The response of thermocline ventilation to variability at the ocean surface from observations and offline tracer modeling

Andrew Edward Shao

A dissertation
submitted in partial fulfillment of the
requirements for the degree of

Doctor of Philosophy

University of Washington

2016

Reading Committee:

Sabine Mecking, Chair

LuAnne Thompson, Co-Chair

Rolf Sonnerup

Program Authorized to Offer Degree:
School of Oceanography

University of Washington

Abstract

The response of thermocline ventilation to variability at the ocean surface from observations and offline tracer modeling

Andrew Edward Shao

Chair of the Supervisory Committee:
Dr. Sabine Mecking
Affiliate Assistant Professor, Oceanography

Variability in oceanic ventilation can arise from either changes at the surface of the ocean or the ocean interior. Four studies are presented which advance our understanding on how these changes can be diagnosed in both observational and modeling contexts.

Chlorofluorocarbons (CFCs) and sulfur hexafluoride (SF_6) have been used extensively to infer transit time distributions (TTDs) and ventilation ages in the ocean. An offline tracer model (*Offtrac*) is combined with a simple model of gas exchange to simulate the mixed layer saturations of CFC-11, CFC-12, and SF_6. The large wintertime undersaturations of these tracers arise from the increase in solubility due to the cooling of the mixed layer and also from the entrainment of relatively tracer-poor waters as the mixed layer deepens. In the mode waters of the North Pacific, this can cause a bias TTD mean ages of up to 24%.

The Antarctic Circumpolar Current (ACC) is a strong dynamical feature in the Southern Ocean which transports water around the entirety of the Antarctic continent. Monte-Carlo simulations of a meandering Gaussian jet model in conjunction with distributions of sea level anomaly from 1992 to 2014 are used to determine the mean position and width of the fronts that form the boundaries of the ACC. The mean position of these fronts largely follow the underlying topography. Significant internannual variability in the location of the fronts was

uncorrelated to changes in the Southern Annular Mode (SAM).

Offtrac is used to simulate CFCs, SF_6, oxygen, ideal age, and transit time distributions using a boundary impulse response technique (TTD-BIR). The output from these simulations are used to evaluate how well tracers can constrain the timescales of oceanic ventilation. The inverse Gaussian solution to the 1d transport equation is shown to be a reasonable approximation to the TTD-BIR within the ventilated thermocline of the subtropical gyres, but a poor approximation in regions with strong gradients in age. 1d TTDs constrained by modeled CFC-12 and SF_6 have a strong bias towards diffusively dominated transport. By comparing variability in oxygen and tracer-inferred TTD mean ages to changes in ideal age, guidelines are developed as to where observations of these tracers may robustly diagnose changes in ventilation.

The effect of how variability of a tracer at the surface maps to changes in the oceanic interior is examined using an analytic Fourier transform of the 1d TTD. The magnitude and phase of the Fourier coefficients of the 1d TTD demonstrate that interior variability is a result of ventilation behaving like a low-pass filter with nonlinear phase response applied to a time-varying surface boundary condition. Typical values of the parameters of the filter for the thermocline suggest that primarily the low-frequency (> 5 years) part of the time-varying boundary condition are likely to observed within the interior.

Both climatological and hindcast adjoint TTDs are calculated in Offtrac to understand variability of the formation of North Pacific Mode Water (NPMW) and South Indian Ocean Subantarctic Mode Water (ISAMW). Using volume fraction (V_f) and mean ages calculated from these adjoint TTDs, NPMW is found to be formed within one region of the North Pacific, whereas ISAMW likely has at least two formation regions, one within the Indian Ocean and another southwest of Australia. Empirical orthogonal function analysis shows that about 54% of ISAMW V_f variability is captured by a mode, uncorrelated to SAM

($p < 0.1$), with a 30-year oscillation between the two climatological formation regions. For NPMW, 69% of the variability is explained by a meridional mode centered around 35°N in the central North Pacific that is significantly correlated ($p < 0.05$) with the Pacific Decadal Oscillation.

TABLE OF CONTENTS

LIST OF FIGURES

LIST OF TABLES

ACKNOWLEDGMENTS

The work accomplished here and personal growth as an oceanographer are a result of the excellent guidance and mentorship provided by my advisor Sabine Mecking and co-advisor LuAnne Thompson throughout my time at the University of Washington. My gratitude goes to them for their patience as I have honed my writing and technical skills over the years. Sincere and special thanks to Sabine for taking me on as the first Ph.D. student she has advised from beginning to end, for supporting me through all the challenges of graduate school, and for all the time she has spent over the years as my guide.

I also recognize my fellow graduate students that I have had the fortune to meet during graduate school, in particular Hayley Dosser, Jacob Wenegrat, John Guthrie, Melinda Webster, and Leah Johnson for all their friendship over the years. A standing ovation to all those I have met through Stage Notes, especially Jillian Johnson, who have welcomed me to the larger University of Washington community. Also my profound thanks to my family, Pop, Mom, Jongni, and Na for helping me become the person I am now.

Lastly, I recognize all the mathematicians, scientists, and technicians on whose work this thesis relies. May I always deserve to be counted in their ranks.

DEDICATION

This thesis is dedicated to my forever person Hayley and my best friend Jessica.

Chapter 1

INTRODUCTION

The work presented in this thesis addresses the subject of oceanic ventilation, the process by which gas-rich water parcels are delivered from the oceanic surface to the interiors. The problem of determining the mean state and variability of ventilation is approached from observational, theoretical, and numerical modeling perspectives. This introduction is a qualitative overview of the advances made by both historical and recent oceanographers that have contributed to our understanding of oceanic ventilation.

1.1 The 3d-circulation of the ocean

The two dimensional, horizontal movement of water at the ocean's surface is a phenomenon that has been documented since the earliest seafaring civilizations. For much of human history, the concept of an ocean-river surrounding a disk of land prevailed until challenged by Aristotle who asserted that the Earth was spherical. Exploration during the Age of Sail saw the first observations of the major currents (in chronological order) in the Indian, Atlantic, and Pacific Oceans (Idyll, 1970). However only after the invention of the marine chronometer by John Harrison in the late 1700s could longitude be determined at sea (Gould, 1923) and thus also could the first accurate chartings of ocean currents be made.

The current understanding of the large-scale circulation began with the era of modern oceanography. In the late 1800s, Zöppritz (1878) argued that the piling up of water in the western tropics by the wind drove northward currents (though crucially ignored the effects

of the Earth's rotation). Conversely, Sandström (1908) posited that the movement of water owed to differences in density which led to the northward flow of warm water. The theory of wind-driven circulation put forth by Zöppritz (1878), was advanced by Sverdrup (1947), who in turn built on the work of Ekman (1906) to develop a theoretical model of the wind-driven gyre circulation that could be used to predict the transport of water in the upper 1000m of the ocean. Further developing the ideas presented by Sverdrup and incorporating the effects of friction at the continental boundaries and bottom of the ocean, Stommel (1948) and Munk (1950) provided an analytic model of the ocean circulation which forms our current view of horizontal oceanic transport being organized into the large-scale gyres with intensified western boundary currents.

Vertical velocity of water parcels in the ocean is often orders of magnitude smaller than in the horizontal, but is crucial to setting the vertical structure of the ocean. Vertical transport in the ocean can either be downwards into the ocean interior (downwelling) or upwards (upwelling). Some of the most dramatic examples of this vertical motion are found during deep and bottom water formation where strong convection leads to water parcels mixing from the surface down to 1000-3000m in depth (Marshall and Schott, 1999). These areas of strong convection occur in relatively localized geographic areas in the North Atlantic (Dickson et al., 1990) and around the Antarctic continent (Seabrooke et al., 1971).

In the upper 1000m of the thermocline (where density changes rapidly with depth) the delivery of water parcels from the surface ocean into the interior is characterized by subduction (Cushman-Roisin, 1987). The subject of thermocline ventilation (so named because of the delivery of gas-rich surface waters into the ocean interior) was first explored by Iselin (1939). In that study, he noted that surfaces of constant density (isopycnals) within the thermocline could connect with the surface at some latitude (that is the isopycnal 'outcrops'). Exposure to converging winds (i.e. negative wind-stress curl) leads to the pumping of water onto these isopycnals and drive motion throughout the entirety of the isopycnal. Later in-

vestigations (for example Woods (1985)) showed that subduction can also occur from mixed layer detrainment during springtime shoaling of the mixed layer and lateral induction of water parcels by large-scale circulation acting against strong gradients in mixed layers.

1.2 Numerical modeling of the worlds oceans

Both the gyre circulation and ventilation of the thermocline are emergent properties of the so-called 'primitive equations' which describe a particular set of differential equations derived from thermodynamics and the hydrostatic Navier-Stokes equations introduced first by Bjerknes et al. (1904). Due to the highly non-linear nature of these equations in addition to the complex boundary conditions associated with the geometry of the Earth, these equations can usually only be solved using numerical techniques.

Numerical models of the ocean provide a means to test theoretical predictions and perform experiments which are either impossible or impractical to do in an observational context. One of the earliest demonstrations of the power of models can be attributed to Cox (1975). In this study, the ocean was discretized into a 3d grid with roughly 200km resolution in the horizontal and 100m resolution in the vertical. Their control run incorporated realistic representation of topography and coastlines and was forced at the surface by winds, heat fluxes, and freshwater input. This control run provided estimates of water transport within the major western boundary currents and the Antarctic Circumpolar Current (ACC) which runs eastward around the Antarctic continent. By running a variety of experiments, they found that wind forcing contributed to the transport within these currents, confirming the theoretical work of Sverdrup (1947), Stommel (1948), and Munk (1950). They also noted that in order to capture the details of oceanic circulation, the model had to be run with realistic temperature and salinity distributions, validating the hypothesis of a buoyancy driven component of the circulation put forth by Sandström (1908).

Since this early implementation of an oceanic general circulation model (GCM), com-

putational and theoretical advances have lead to increasingly better representations of the world's oceans. While current state-of-the art, ocean-only global configured models can now be run at increasingly higher horizontal resolutions (e.g. Maltrud and McClean (2005)), lower resolution models have also benefited from the development of parameterizations of processes that occur on smaller spatial scales. Perhaps the most notable of the various parameterizations are those that attempt to capture the effect of eddies, the size of which are on the order of 10 to 100km (e.g. Gent and Mcwilliams (1990)).

1.3 Modeling tracers in forward, inverse, and adjoint contexts

Many physical, biological, and chemical oceanographic questions require knowledge about the state of some quantity that is transported along with a water parcel. Such quantities are referred to as 'tracers' which are further characterized chemical/physical, active/passive, or conserved/non-conserved. Chemical tracers are actual compounds which are transported along with the parcel (e.g. chloroflurocarbons (CFCs) and arguably salinity) (England and Maier-Reimer, 2001). Physical tracers describe a property of the water parcel (e.g. temperature) and also tend to be active tracers because they directly associated with one of the terms in the equations of motion (Iselin, 1939). Chemical tracers also tend to be classified as passive tracers because they do not appreciably interact with with the flow. The concentration of a conserved tracer can only be modified by the flow whereas non-conserved tracers have sources or sinks.

The transport of tracers in the ocean can be described by a mathematical model- broadly defined as any equation or system of equations that generate an output based on relationships between the model parameters (Bender, 2000). The tracer transport equation (which has different names depending on discipline) describes how the concentration of a conserved, passive tracer of a water parcel changes in the presence of advection and diffusion. In an

Eulerian framework it can be written as

$$\frac{\partial C}{\partial t} + \vec{u} \cdot \nabla C = \nabla \cdot (\kappa \nabla C) + R \tag{1.1}$$

where C is the concentration of the tracer, t is time, $\vec{u}$ is a 3d velocity vector, κ is a 3d diffusion coefficient, and R is a potential source or sink of the tracer. Depending on scale, κ can represent molecular diffusion or mixing due to the effects of unresolved eddies (Gill, 1982). Much of the research presented in this thesis relies on either forward, inverse, or adjoint solutions to this equation. A qualitative overview of these three formulations are briefly discussed here but are presented in further technical detail in Chapters 2, 4, and 5.

Using a forward model would mean prescribing $\vec{u}$ and κ and then stepping the 1.1 forward in time to solve for C. GCMs almost always simulate tracers as a forward model as $\vec{u}$ and κ are calculated diagnostically from the core primitive equations which are then used to numerically integrate (1.1) to determine C at the next timestep. The offline tracer transport model (*Offtrac*) used in this study is another example of a 'forward model.' First, the fields necessary to integrate (1.1) are calculated using a GCM, but then saved offline. Tracer sources and sinks are then prescribed and the model stepped forward in time. The advantage of an 'offline' transport model is primarily computational because 1) only the tracer transport equation and not all the primitive equations must be solved and 2) the length of the timestep can be on the order of days which is much longer than that taken in a GCM, where the timestep must be on the order of hours to resolve faster dynamic timescales.

The use of an inverse model, by contrast, uses observations of C to estimate $\vec{u}$ and κ. This is often an underdetermined problem- that is too few observations of C exist to uniquely constrain estimates of $\vec{u}$ and κ. However if simplifying assumptions are made, the number of free parameters can be reduced. For the problem of tracer transport, a common technique (used in this thesis and other studies) assumes that transport is one dimensional with a constant velocity u and κ which are the only two free parameters. This simple model 1d

advective-diffusive pipe model can represent oceanic transport relatively well because most oceanic transport occurs along surfaces of constant density (Montgomery, 1937).

An analytic form of the Green's function solution to this problem was derived by Holzer and Hall (2000) who showed that any given water parcel has a distribution of transit times which can be described by a mean age and a shape parameter. This so called 1d transit time distribution framework, combined with measurements of CFCs, sulfur hexafluoride (SF_6), and helium/tritium have allowed for better representations of the transport timescales from the surface to the interior of the ocean (e.g. Waugh (2003), Sonnerup et al. (2008)).

1.4 Overview of thesis

The work presented in this thesis uses numerical and analytic models to understand the response of thermocline tracer properties to surface variability using tracers that are commonly measured. Chapter 2 uses *Offtrac* to estimate the mixed layer saturations of CFC-11, CFC-12, and SF_6. Chapter 3 uses a simple, Gaussian meandering jet model combined with satellite altimetry to estimate the magnitude and causes variability in the path of the ACC (which affects the ventilation of the Southern Ocean). Chapter 4 evaluates how well and where CFCs, SF_6, and oxygen can be used either individually or in tandem to constrain oceanic ventilation and diagnose changes in ventilation. Chapter 5 shows how variability at the surface is modified by oceanic ventilation and uses an adjoint form of Offtrac to determine potential surface sources of variability for mode waters in the North Pacific and South Indian Ocean. Chapter 6 provides a brief summary of the results in Chapters 2-5 and suggests further work and additional avenues of investigation that arises from the advancements presented in this dissertation.

Chapter 2

MIXED LAYER SATURATIONS OF CFC-11, CFC-12, AND SF_6 IN A GLOBAL ISOPYCNAL MODEL

Published citation: Andrew E. Shao, Sabine Mecking, LuAnne Thompson, and Rolf E. Sonnerup, 2013: Mixed layer saturations of CFC-11, CFC-12, and SF_6 in a global isopycnal model. Journal of Geophysical Research - Oceans, 118(10), 4978-4988. doi: 10.1002/jgrc.20370

Abstract

The use of CFC-11, CFC-12, and SF_6 to quantify oceanic ventilation rates, interior water age, and formation rates requires knowledge of the saturation levels at the sea surface. While their atmospheric histories are relatively well known, physical processes in the mixed layer in conjunction with limited air-sea gas exchange can cause surface concentrations to be in disequilibrium with the atmosphere. We use an offline tracer advection-diffusion code that evolves tracers using along-isopycnal and cross-isopycnal mass fluxes from a global, climatological run of the Hallberg Isopycnal Model to reconstruct the saturation level of all three tracers over the entirety of their atmospheric histories. Disequilibria on a global scale occur in regions associated with deep winter mixed layers and are found throughout the time period of the release of these chemicals into the atmosphere. Sensitivity studies using targeted

model simulations, focusing on the North Pacific, show that seasonal cycles in temperature and salinity that affect gas solubility as well as entrainment of water containing low concentration of tracers during mixed layer deepening are the dominant causes of undersaturation. When using the transit time distribution method, our results show that these undersaturations introduce a significant bias towards older ages for North Pacific Central Mode Water but do not significantly affect estimates of anthropogenic carbon inventory.

2.1 Introduction

Transient, anthropogenic gases such as the chlorofluorocarbons CFC-11 and CFC-12 have been used extensively as tracers of oceanic ventilation. These compounds have been released in detectable amounts since the 1940s and have atmospheric mixing ratios whose time history can be estimated well from observations or inferred from anthropogenic activity (Walker et al., 2000) (2.1a). Due to measures undertaken as a result of the Montreal Protocol in 1987, atmospheric CFC concentrations have begun to decrease. The complications that arise from this nonmonotonic history and from the similarity between the CFC-11 and CFC-12 source functions (Sonnerup, 2001) has spurred the extension of tracer techniques to include sulfur hexafluoride (SF_6), another anthropogenic gas which has been released in a exponentially increasing manner since the mid-1950s (Bullister et al., 2006; Sonnerup et al., 2008).

One application of transient tracers, the transit time distribution (TTD) method, described by Haine and Hall (2002) has provided a framework to estimate the mean age and width of the distribution that describes the spectrum of the ages in a water parcel by inferring the advective-diffusive Green's function from in-situ tracer observations. This problem is highly underconstrained, but the use of CFCs and SF_6 in tandem can give better estimates of the TTD (Hall et al., 2002; Waugh, 2002a). As noted by Hall et al. (2007) a significant source of error in these calculations is the disequilibrium in tracer concentration between the atmosphere and oceanic mixed layer. The most important aspect of this disequilibrium is gas

undersaturation with respect to the atmosphere (i.e. negative disequilibrium) observed at the end of winter when permanent subduction into the thermocline occurs (Cushman-Roisin, 1987) or during water mass formation through deep convection (Marshall and Schott, 1999). Undersaturations during water mass subduction/formation can significantly skew estimates of ventilation ages and pathways from tracers as well as oceanic anthropogenic carbon concentration using the tracer-based TTD (Waugh et al., 2004; Tanhua et al., 2009) or ΔC^* methods (Gruber et al., 1996).

Studies utilizing CFC and SF_6 concentrations to infer ages or TTDs have employed a variety of methods to address the biases introduced by undersaturation. Most researchers assume a constant fixed value of saturation over time (e.g., Waugh et al., 2004; Tanhua et al., 2009). For example in a global study, Khatiwala et al. (2009) used mixed layer undersaturations observed during the World Ocean Circulation Experiment (WOCE) era to scale the CFC mixed layer boundary condition derived from atmospheric concentrations. Using a one dimensional slab mixed layer model, Haine and Richards (1995) showed a seasonal variability of 70-100% saturation for CFC-11 and CFC-12. Mecking (2004), based on constraining a 2D advection-diffusion model to reproduce observed interior concentrations, estimated the CFC saturations at isopycnal outcrops in the North Pacific to be as low as 80%. Local one-dimensional mixed layer models tuned to the region of North Pacific Central Mode Water Formation in the 1990s gave similar low saturation values for the North Pacific (Tokieda et al., 2004; Mecking et al., 2006) while CFC saturation in regions of seasonal ice coverage, such as the Antarctic margins, may be even lower (Rodehacke et al., 2010).

In this paper, we use an offline tracer transport code described in Section 2.2 to estimate the temporal and spatial variability in the surface saturation of CFC-11, CFC-12, and SF_6. We define undersaturation (λ) by

$$\lambda = 100 \times (1 - C_{obs}/C_{sat}) \tag{2.1}$$

which describes the percent deviation from equilibrium when the observed or modeled tracer concentration (C_{obs}) is smaller than the saturation value (C_{sat}). By this definition, negative values of λ represent oversaturation, and $100 - \lambda$ is equivalent to percent saturation.

Model results are presented in Section 2.3. We show global maps of undersaturation to identify spatial patterns (Section 2.3.1) as well as time series of undersaturation at a fixed location (Section 2.3.2). We then evaluate the role of physical processes controlling undersaturation in the North Pacific by performing a series of model experiments to isolate the effects of the seasonal cycle in saturation concentration, gas transfer velocities, and wintertime entrainment of subsurface waters (Section 2.3.3). The runs performed for this paper are summarized in Table 2.1. The discussion of these results and conclusions are presented in Sections 2.4 and 2.5, respectively.

2.2 Model descriptions

The research conducted herein relies on a two-tiered modeling approach. First, monthly averages of physical fields are derived from the Hallberg Isopycnal Model (HIM), a general circulation model solving the oceanic primitive equations of motion with realistic forcing. These fields are then used to drive an offline tracer advection-diffusion code with along-isopycnal mixing, dubbed Offtrac.

2.2.1 Hallberg Isopycnal Model

Our run of HIM is similar to the default publicly available code distributed by NOAA's Geophysical Fluid Dynamics Laboratory (http://www.gfdl.noaa.gov/ocean-model) (Hallberg, 1995). The horizontal grid is 210 cells in the meridional coordinate (nominally 1/3 degree resolution near the equator and 1 degree elsewhere) and 360 cells (1 degree resolution) in the zonal. The vertical resolution is determined by a distribution of 50 density interfaces (49 layers) referenced to 2000db ranging from $\sigma_2 = 21.85 - 37.90$ kg m^{-3}. The surface ocean is a

Kraus-Turner bulk mixed layer with Richardson-based turbulence (Kraus and Turner, 1967) and two buffer layers allowing smooth detrainment/entrainment to outcropping isopycnal surfaces. Transport due to unresolved eddies are parameterized as along-isopycnal diffusion, an isopycnal thickness diffusion equivalent to a Gent-McWilliams scheme (Gent and Mcwilliams, 1990) (each with a diffusivity of 600 $m^2\ s^{-1}$), and cross-isopycnal diffusion with a diffusivity of $10^{-5}\ m^2\ s^{-1}$.

The model is initialized as a quiescent ocean with isopycnal depths, temperature, and salinity from the Steele et al. (2001) climatology. Surface salinity is restored to climatology with a transfer velocity of 50 cm day^{-1} by adding an implied freshwater flux. The model is spunup for 650 years using the normal year climatological Common Ocean Reference Experiment version 2 (CORE-2) forcing (Large and Yeager, 2008). Previous applications of HIM include participation in the Coordinated Ocean-ice Reference Experiments Model Intercomparison (Griffies et al., 2009), North Pacific mode water studies (Ladd and Thompson, 2000, 2002) as well as investigation of oxygen variability in the North Pacific (using the Offtrac code) (Deutsch, 2005; Deutsch et al., 2006).

Because CFCs and SF_6 invade the ocean through air-sea gas exchange at the surface (except for a few SF_6 tracer release experiments, with SF_6 now being replaced by SF_5CF_3; e.g. Ho et al. (2008)), mixed layer processes play a crucial role in controlling the saturation states of CFCs and SF_6. As a metric of how well these dynamics are represented in HIM, we compare the maximum mixed layer depths from the model (Figure 2.2a) to a mixed layer product based on Argo profiles by Holte and Talley (2009) (Figure 2.2b). The root-mean-square difference between the model and the observations amounts to 45m globally and 30m for the North Pacific.

Visual comparison between Figures 2.2a and 2.2b shows that with the exception of the Brazil Current extension, the large-scale structure of maximum mixed layer depth in the model agrees well with observations, specifically in the South Indian, South Pacific, North

Atlantic, and North Pacific Basins. In the western boundary current extensions, the regions of maximum mixed-layer depth are larger in extent in the model than observed. This bias is typical of non-eddy resolving models because horizontal resolution is insufficient to fully resolve western boundary current dynamics (Smith et al., 2000; Penduff et al., 2010) or to adequately represent the eddy-controlled Antarctic Circumpolar Current (Hallberg and Gnanadesikan, 2006). The modeled mixed layers also tend to be somewhat too deep because not all the processes controlling restratification are captured. For example, the western boundary current extensions are weaker than observed and do not advect warm water sufficiently quickly into the interior ocean, and also the restratification owing to the effect of mixed layer eddies is not adequately represented (Hallberg, 2003). This tendency towards deeper mixed layers slows the time required for air-sea gas equilibration and accordingly may bias modeled undersaturations high. The Kuroshio and Kuroshio Extension (K/KE region) region off Japan, the subject of our more detailed analyses (see Sections 2.3.2 and 2.3.3), is relatively well represented with maximum mixed layer depths being only about 10% deeper in the model and covering roughly the same geographic area as in the observations.

2.2.2 Offtrac

To study the processes controlling surface disequilibria, particularly undersaturations of CFC-11, CFC-12, and SF_6, we use the three-dimensional monthly averaged mass transports, surface wind speeds, temperature (T), and salinity (S) as well as monthly instantaneous isopycnal thickness fields from HIM to drive the offline model, Offtrac. These input fields to Offtrac, more specifically, are based on a normal year 12-month climatology created by averaging the monthly physical fields over the last 20 years of the 650-year HIM run. Tracer uptake was modeled using the one-dimensional air-sea gas exchange equation at each grid point:

$$\frac{\partial C}{\partial t} = \frac{k_w}{H}(C - C_{sat}) \tag{2.2}$$

where C is the concentration of the tracer, k_w is the gas transfer velocity scaled by the Schmidt number of the gas (Wanninkhof, 1992; Zheng et al., 1998), H is mixed layer depth, and C_{sat} is the saturation concentration which for CFCs and SF_6 is based on the tracers' empirically determined solubility functions (Warner and Weiss, 1985; Bullister et al., 2002) and atmospheric pressure. In Offtrac, gas exchange fluxes are calculated after advecting and diffusing tracers by integrating (2.2) using an Euler forward method with a roughly one day time step. Following the Ocean Carbon Modeling Intercomparison Project Phase 2 (OCMIP-2) guidelines (Najjar and Orr, 1998), the monthly averaged gas transfer velocities values were calculated by assuming a quadratic dependence on wind speed (U) (Wanninkhof, 1992): $k_w = \alpha U^2$. For consistency with the physical model, the U used for Offtrac are based on the CORE-2 forcing instead of the 1987-1992 SSM/I winds used in OCMIP (Najjar and Orr, 1998). Following the assumptions of Sweeney et al. (2007), we determined α by scaling k_w to an average CO_2 gas transfer velocity of 15.6 cm hr^{-1} [C. Sweeney, unpublished data, 2012]. Through this scaling, bubble processes that can enhance gas exchange (Keeling, 1993; Schudlich and Emerson, 1996) but that are not explicitly parameterized in the model are accounted for to first order. The model configuration described here will be referred to as the control run (Experiment 1, Table 2.1) in the sections that follow.

2.3 Results

We primarily discuss the results from CFC-11 as being representative of the spatial patterns of mixed layer saturation levels for all three gases, but also examine differences between CFC-11, CFC-12 and SF_6 when looking at the temporal evolution of undersaturation (Section 2.3.2). For the latter and for the sensitivity experiments in Section 2.3.3, we focus the analysis on the North Pacific because its ventilation dynamics, lacking deep-water formation, are simple relative to other basins and because mode water formation and corresponding mixed layer depth patterns in the North Pacific have been well studied

with HIM (Ladd and Thompson, 2000, 2001, 2002). Additional figures, including global maps of CFC-12 and SF_6 mixed layer saturations, are available in the supplemental material online (http://www.apl.washington.edu/project/project.php?id=cfc_mixed_layer). The model's sea surface temperature (SST), sea surface salinity (SSS), and mixed layer depth, along with the tracers' time-evolving surface concentrations and saturation levels are also made available online as netCDF files.

2.3.1 Regional descriptions of undersaturation

The spatial structure of the saturation is relatively independent of time when climatological circulation fields are used to evolve the tracer structure. Hence, we first focus on the spatial pattern of maximum undersaturation of CFC-11 in 1980 (Figure 2.3) in combination with mixed layer depth (Figure 2.2), to show the boundary condition for relatively young (10-20 years), near surface waters measured during the 1990s WOCE era.

In the open North Pacific, the largest undersaturations occur in the K/KE region off Japan (Figures 2.3a and 2.3b). This region is associated with deep mixed layers (yellow colors in Figure 2.2a) and the formation of North Pacific Subtropical and Central Mode Waters (the latter abbreviated as NPCMW) (Nakamura, 1996). Additionally, large undersaturations can be seen in the Sea of Okhotsk, the source area for the waters that eventually form North Pacific Intermediate Water, and other marginal seas although the model resolves the dynamics in these areas less well. At the equator, strong upwelling in the east Pacific basin exposes older, low tracer concentration water to the surface which causes maximum undersaturations on the order of 5% there (Figure 2.3a). Similarly, coastal upwelling produces tracer undersaturations along the eastern margins of the Pacific and Atlantic Oceans.

In the southern hemisphere, mode water formation sites of the Indian, Pacific, and Atlantic basins correspond to some of the deepest mixed layer depths of the world's oceans (yellow and red colors in Figure 2.2) and are associated with some of the largest under-

saturations (as large as to 20%; Figure 2.3a). The patch of undersaturation east of the Antarctic Peninsula and north of the Weddell Sea is due to large amounts of winter ice coverage (thick, black contour line in Figure 2.3a) which isolates the surface ocean from the atmosphere preventing gas exchange.

The North Atlantic basin shows a large coherent patch of undersaturation that stretches northeastward from the U.S. east coast and whose overall shape is consistent with the formation site of Eighteen Degree Water (Talley and McCartney, 1982), northeastward advection in the North Atlantic Current, and the formation of Labrador Sea Water (Talley and McCartney, 1982) which occurs eastward in the model off the tip of Greenland and not in the Labrador Sea.

The sites of large maximum CFC-11 undersaturations (Figure 2.3a) which mostly occur in mid to late winter, correlate spatially with large maximal mixed layer depth (Figure 2.2a; R = 0.65 between maximum mixed layer and maximum CFC-11 undersaturation maps), also usually present at the end of winter and a prerequisite for mode water formation (McCartney, 1982). Because of the frequent collocation of sites where large wintertime undersaturations occur with mode water formation sites (see above), we focus further analysis (Sections 2.3.2 and 2.3.3) on the physical processes associated with those sites. Wintertime cooling results in buoyancy loss and weaker stratification which combined with momentum input from strong winds causes mixed layer deepening. The solubilities of CFCs and SF_6 are temperature dependent so this cooling also increases their saturation concentrations driving a larger deviation of C from C_{sat} (2.2). Deeper mixed layers also have two-fold effect leading to larger undersaturations: the tracer equilibration time scale is inversely-proportional to H (2.2) and mixed layer deepening entrains older waters from below with relatively low tracer concentration. However, k_w increases with wind speed so the higher winds may partially balance these disequilibria-causing effects (see Section 2.3.3 for further analysis of these effects).

2.3.2 Temporal evolution of undersaturation

To demonstrate how the degree of undersaturation varies over time, we examined the maximum undersaturation of CFC-11, CFC-12, and SF_6 (Figure 2.4a) over a patch in the K/KE region where maximum CFC-11 undersaturation in 1980 was greater than a threshold value chosen at 8% here (black contour line in Figure 2.3b) and where North Pacific mode waters are formed (see previous section).

The degree of maximum undersaturation declines over time as the ocean tracer concentrations become closer to equilibrium with the atmosphere (Figure 2.4a). Deviations from a smooth decrease are caused by changes in the growth rate of the atmospheric concentration of the tracers (Figure 2.1b). Generally, maximum undersaturations decrease faster during times of small atmospheric growth than during times of large atmospheric growth. For example, the CFC-11 atmospheric concentration increased relatively slowly from 1950-1960 (blue line in Figure 2.1b) such that the maximum CFC-11 undersaturation decreased from 19% to 13% (blue line in Figure 2.4a). From 1960-1975, the atmospheric growth accelerated while CFC-11 maximum undersaturation decreased very slowly from 12% to 11%. From 1975-1990, a fairly constant atmospheric CFC-11 growth rate caused a decrease in the undersaturation from 11% to 8%. The deceleration in the CFC-11 growth rate from 1990 to present day, including a decrease in atmospheric CFC-11 concentrations since 1994, allowed for a decrease in wintertime undersaturations to as low as ∼4% in recent years. The time series of CFC-12 undersaturations (red line in Figure 2.4a) is similar to that of CFC-11 with a less steep decline in maximum undersaturation (from 14% to 12%) in the initial part of the record (1950-1960). In contrast to CFCs, SF_6 atmospheric concentrations (black lines in Figure 2.1) have grown monotonically at a roughly exponential rate over the course of its record. Accordingly, SF_6's maximum undersaturation declines slowly overall, after the initial part of its record, from ∼10% in 1960 to its 2010 value of ∼7% (black line in Figure 2.4a). CFC undersaturations of 4-5% persist until present day (Figure 2.4a) likely due to the sea-

sonal cycle of solubility (see Section 2.3.3) and despite the slowing of the CFC atmospheric growth rates/reduction of atmospheric concentrations since the 1990s.

As illustrated for CFC-11 in Figure 2.4b, tracer undersaturations exhibit a strong seasonal cycle imposed on the interannual behavior described above with the largest undersaturations occurring in late winter. Conversely in the summertime, the surface ocean is in near equilibrium due to the lower solubility of gases in higher temperature waters and a shallow mixed layer. Supersaturations may occur then if gas exchange cannot keep pace with the warming despite the shallower mixed layers. In the model, CFC-11 in the western part of the North Pacific does not become supersaturated beyond 1% (Figure 2.4b) whereas the eastern part does exhibit supersaturations as high as 5% in 1980 and beyond (not shown). This is, however, significantly less than what has been observed on some summer cruises (Warner, 1988). The lesser supersaturations in the model may be attributed to the monthly advection-diffusion time step, masking the quick restratification and rapid heating of the mixed layer that can occur in the summer. Additionally, interannual variability in wind speed, particularly anomalously quiescent periods (not captured by the model because it is based on climatological forcing) may play a large role in allowing larger supersaturations in the observations.

Focusing on the seasonal cycle for one model grid point (39.5^{o}N, 163.5^{o}E; see Figure 2.3b for location of grid point) illustrates that the month of the largest undersaturation at any point in the model does not necessarily correspond to the month of deepest mixed layers (dashed lines in Figure 2.5). Instead, it usually corresponds to the month which has the largest increase in mixed layer depth (Figure 2.5a) and/or largest decrease in temperature and hence increase in solubility (Figure 2.5b) which often occurs 1-2 months before mixed layer depths reach their maximum. SF_6 solubility is less sensitive to temperature than the CFC solubilities. Accordingly, the maximum SF_6 undersaturation is smaller in the early part of the SF_6 record (1955-1975) compared to CFCs (Figure 2.4a). In 1980, at the model

grid point shown in Figure 2.5, CFC-11, CFC-12, and SF_6 all have comparable seasonal amplitudes in saturation state (Figure 2.5c) whereas in more recent years (using 2005 as an example, Figure 2.5d) SF_6 is more undersaturated than CFCs by about 1-2% because of the slowing of the atmospheric CFC growth curves.

2.3.3 Sensitivity Experiments

We perform a set of model experiments (Experiments 2-6; Table 2.1) to try to determine the contribution of gas exchange rates, seasonality of solubility based on T and S, mixed layer entrainment of older, lower concentration water in the winter, and the combined effect of the seasonal cycle and entrainment on the modeled tracer saturations (Figures 2.6 and 2.7). For reasons mentioned previously, we focus on the North Pacific region in the model and compare the resulting CFC-11 undersaturations in the sensitivity runs to the control run (Figure 2.3b; Experiment 1 in Table 2.1).

Dependence on gas transfer velocities

We performed two experiments to examine the sensitivity of the saturation level to gas transfer velocities. In Experiment 2, we replace the monthly-varying k_w with each grid point's annual average to evaluate the importance of seasonally varying wind speeds (Figure 2.6a). In response, the magnitude of maximum CFC-11 undersaturation in 1980 increases across the basin particularly in the K/KE region where undersaturations in the control run (Figure 2.3b) were already large. This suggests that high winter wind speeds (as present in the control run) do indeed act to reduce the wintertime disequilibrium in the mixed layer due to higher gas exchange rates (see Section 2.3.1). In Experiment 3, instead of scaling the globally averaged k_w (2.2) to the revised radiocarbon-based CO_2 exchange rate of 15.6 cm hr^{-1} [C. Sweeney, unpublished data, 2012], we scaled it to the higher, earlier estimate of 21.7 cm hr^{-1} (Broecker et al., 1986). The level of undersaturation across the North Pacific basin

is dramatically reduced in this case (Figure 2.6b) compared to the control run (Figure 2.3b) with maximum CFC-11 undersaturation values in the K/KE region reaching only 8% in 1980. This suggests that the saturations reported in this paper are sensitive to the magnitude of k_w and that model studies like OCMIP-2, that use the larger, globally averaged Broecker et al. (1986) k_w to scale to, might be underestimating the degree of disequilibria that CFCs and other gases experience in the mixed layer.

Sensitivity to seasonality of solubility

In Experiment 4, to determine the effect of the seasonal cycle in SST and SSS (and accordingly solubility), we calculated C_{sat} (2.2) in the mixed layer using each grid point's annually averaged temperature and salinity (Figure 2.7a) instead of using the monthly varying fields as in the control run (Figure 2.3b). In the southern and eastern parts of the North Pacific basin, the surface ocean remains essentially in equilibrium with the atmosphere in this case with maximum undersaturations somewhat closer to 0% than in the control run (Figure 2.3b). Tracer concentrations in the K/KE region and the Sea of Okhotsk are also much closer to equilibrium with the percent undersaturation being reduced to about half of its value from the control run. The basin-wide decrease in undersaturation suggests that the seasonal cycle in solubility and accordingly C_{sat} (which are highest in winter when SST's are the lowest) is a significant contributor to the degree of undersaturation observed in the control run.

Sensitivity to entrainment of subsurface water

In Experiment 5 to remove the effect of the entrainment of older waters containing mostly lower (until recently) tracer concentrations, we do not allow tracer concentration to change when the mixed layer deepens and entrains water from below, although the tracer is still allowed to be transported horizontally. Thus, the mixed layer is entraining water with the

same concentration as the mixed layer. In contrast to Experiment 4 (Figure 2.7a), the southern and eastern parts of the basin remain undersaturated to approximately the same (small) level (Figure 2.7b) as found in the control run (Figure 2.3b). The most dramatic difference in undersaturation between this experiment (Figure 2.7b) and the control simulation (Figure 2.3b) occurs in the K/KE region and the eastern edge of the Sea of Okhotsk. These waters are even closer to equilibrium ($\lambda \approx 5\%$) than in Experiment 4 (Figure 2.7a) indicating that entrainment of subsurface, tracer-poor water also plays an important role in the K/KE region.

Sensitivity to both seasonal solubility cycles and entrainment

In Experiment 6, we remove both the seasonal cycle in solubility (Experiment 4) as well as the effects of entrainment of subsurface water (Experiment 5). The removal of these effects in tandem yields surface waters that are essentially at equilibrium ($\lambda < 2\%$ everywhere in 1960 and beyond) for CFC-11 (Figure 2.7c) as well as for CFC-12 and SF_6 (not shown). From this we conclude that the seasonal cycle in solubility and entrainment of lower tracer waters are the main reasons for CFC and SF_6 undersaturation in the mixed layer during those times. CFC-11 undersaturations larger than 2% existed before 1960, likely attributable to the relatively rapid growth of CFC-11 atmospheric concentrations then.

Having identified two major processes that cause undersaturation (seasonal solubility cycles and entrainment), we examine differences in the temporal evolution of maximum undersaturation, averaged over the K/KE region (Figure 2.3b), between the control simulation and the experiments that isolate these effects (Experiments 4 and 5; Figure 2.8). Since 2000, CFC-11 is near saturation in Experiment 4 (blue line in Figure 2.8), while Experiment 5 (red line in Figure 2.8) shows undersaturations similar to those in the control run (black line in Figure 2.8). This suggests that in recent years entrainment has played only a minimal role in causing CFC-11 disequilibria because waters in the seasonal pycnocline are no

longer tracer-poor relative to an atmosphere where CFC concentrations have stalled and declined. However until 2000 (especially before ∼1980), the maximum CFC-11 undersaturation found in Experiment 5 is significantly less than in the control run, suggesting that entrainment was the dominant cause of disequilibria in the earlier part of the record. The effects of the seasonal solubility cycle have been relatively constant over time causing a 3-4% decrease in maximum CFC-11 undersaturation in the K/KE region compared to the control run throughout the record (see offset between blue and black lines in Figure 2.8).

2.4 Discussion

The model simulations shown here demonstrate that the saturation levels of trace gases vary greatly both in space and in time. To quantify the impact of undersaturation on tracer-inferred quantities, we discuss here an additional model run (Experiment 7) where the mixed layer concentrations were always set to C_{sat} and hence are in equilibrium with the atmosphere. We find that the global CFC-11 inventory in this experiment yields an inventory that is 11% greater in 1970 than in the control run (Experiment 1) where dynamic gas exchange is included (Table 2.1). In 2000, this difference in inventory is only 7% due to the surface ocean being closer to equilibrium in recent years. Similarly, global inventories of CFC-12 and SF_6 are 9.5% and 12.6% higher in 1970 and 6.4% and 7.4% higher in 2000, respectively, compared to the control run. Estimates of water mass formation rates that are based on CFC inventories (Smethie and Fine, 2001) or SF_6 inventories will be affected accordingly since the formation rate is assumed to be proportional to the inventory.

Mixed layer disequilibria can also cause biases in inferred ages of water parcels. Here we examine the ages of water parcels using the 1-d TTD method (Haine and Hall, 2002; Waugh, 2003) which assumes that the TTD can be represented as an 1-d Inverse Gaussian determined by two parameters, a mean age Γ and a width parameter Δ. The ratio Γ^2/Δ^2 is equivalent here to the Peclet number (Pe) of the flow (Waugh, 2003). In the following analysis, we

convert tracer concentrations to an equivalent partial pressure assuming equilibrium with the atmosphere when interior waters left the surface ocean. We then infer Γ by assuming $\Gamma = \Delta$ (Waugh et al., 2004) and finding the TTD that yields the modeled partial pressure when convolved with the atmospheric history of the tracer. Note that Experiment 7 enforces saturated tracer values for CFC-11 at the surface, consistent with the assumptions of surface equilibrium used with the TTD method here, which is not the case for the control run. The difference in the inferred mean ages between the two runs thus represents a measure of the biases in mean age due to undersaturation that one might obtain when calculating Γ from observed tracer concentrations assuming 100% saturation at the surface.

To evaluate the size of the age biases, we applied the TTD method described above to infer the average Γ of the North Pacific thermocline ($\sigma_2 = 30.15 - 35.35$ kg m^{-3}, i.e. all isopycnals that outcrop in the open North Pacific in the model) using the modeled CFC-11, CFC-12, and SF_6 concentrations in January of model years 1980-2010 independently of each other. Each tracer shows a consistent bias towards older ages when comparing the control run to Experiment 7 (not shown). However, the percent differences in the average Γ are small (¡5% for all years 1980-2010) because not all of the thermocline ventilates in areas associated with high undersaturations.

Larger differences between the control run and Experiment 7 may be expected when inferring the ages of mode waters because mode water formation sites, including those in the North Pacific, correspond to areas of high undersaturation in late winter (see Section 2.3.1). We estimated the differences in average Γ in the North Pacific thermocline using only model grid points where NPCMW is present ($\sigma_2 = 33.29 - 34.58$ kg m^{-3} in the model with the requirement that potential vorticity $\leq 2.5 \times 10^{-10}$ m^{-1}s^{-1}, similar to Nakamura (1996) and Ladd and Thompson (2001)). We infer the mean age at model year 1980 (corresponding to the early part of the WOCE era) and 2000 (just after the atmospheric downturn in CFC-11 concentration and prior to the reduction of CFC-12; Figure 2.1). To reiterate, both TTD

calculations assume a saturated boundary condition meaning that surface undersaturations in the control run would cause TTD mean ages to be biased. The resulting bias towards older ages of the average Γ inferred from the control run compared to Experiment 7 is significantly more pronounced for NPCMW (Table 2.2) than the rest of the thermocline for all three tracers. For SF_6, the difference between the two runs amounts to 0.8 years (10.4%) in 1980 and 1.0 years (12.7%) in 2000. For CFCs, the differences in age are somewhat larger, amounting to 1.0 years (13.8%) in 1980 and 1.8 years (23.9%) in 2000 for CFC-11 and 1.0 years (13.7%) in 1980 and 1.6 years (19.2%) in 2000 for CFC-12. The larger differences for CFCs particularly in 2000 that occur despite a decrease in mixed layer undersaturation over time (Figure 2.4a) may be explained by the reduction of atmospheric CFC growth rates since $\sim$1990 which makes the ocean interior age calculations much more sensitive to small variations in tracer concentrations and assumptions about surface saturation. Also, atmospheric CFC concentrations in the past two decades or so are still greater than in the earlier part of the record, yielding a greater absolute difference in mixed layer concentrations between Experiment 7 and the control run despite lower percent undersaturation.

A drift in ages from 1980-2000 exists even when using a saturated boundary condition in the model (Experiment 7) which is consistent with the assumption of 100% saturation used when we inferred the TTDs. However, this drift is smaller than the differences between Experiment 7 and the control run for CFCs (0.2 years for CFC-11, 0.4 years for CFC-12; Table 2.2), but of similar magnitude for SF_6 (-0.9 years; Table 2.2). The drift results from the 1-d Inverse Gaussian with $\Delta/\Gamma = 1$ being a good, but not perfect approximation of TTDs in the North Pacific thermocline (Waugh, 2003; Sonnerup et al., 2013). The results of our first order TTD age comparison for NPCMW, nevertheless illustrate the biases toward older ages that occur when neglecting surface undersaturations and that, particularly for CFCs, increase over time. Tracer-inferred estimates of age for other mode waters and water masses with high tracer undersaturations at their formation sites are expected to be similarly

affected.

Lastly, following Hall et al. (2002) and Waugh et al. (2006), we convolved the TTDs inferred above with the anthropogenic carbon perturbation in the atmosphere to estimate anthropogenic carbon concentrations (C_{ant}) in NPCMW. The differences in C_{ant} inventory between Experiment 7 and the control run are small ($< 3\%$) both in 1980 and 2000 (Table 2.2) indicating that despite uncertainties associated with saturation levels, CFCs and SF_6 are a valuable proxy for anthropogenic CO_2 in the oceans. This relative insensitivity of C_{ant} inventories to tracer saturation levels likely arises because the absolute difference in age is small resulting in similar TTDs. C_{ant} inventories of older mode waters with a similar percent difference (accordingly, higher absolute difference) in age due to the undersaturated mixed layer boundary are likely to be more affected. Further work allowing Pe to vary by constraining TTDs using CFCs and SF_6 combined (Sonnerup et al., 2008, 2013) or utilizing the maximum entropy method (Holzer and Primeau, 2010) will help to investigate the effects of undersaturations on tracer-inferred TTDs and C_{ant} inventories in more detail.

2.5 Conclusions

We have demonstrated that the mixed layer boundary conditions of CFC-11, CFC-12, and SF_6, gases used to diagnose oceanic ventilation, have both spatial and temporal variability in their gas saturation states because gas exchange can fail to keep pace with equilibrium conditions. Significant levels of undersaturation of CFCs and SF_6 can occur particularly as the mixed layers deepen and cool during winter. Using the North Pacific as an example, our results suggest that these undersaturations can be explained primarily by the entrainment of low tracer concentration waters from below the mixed layer and by the seasonal cycle in the temperature-dependent gas solubilities, with the latter being the dominant cause for CFCs since $\sim$1985. The magnitude of the gas transfer velocity also plays an important role, suggesting that model studies (such as OCMIP-2) that scale k_w to a larger global mean

value than recently proposed by Sweeney et al. (2007) might be underestimating the degree of disequilibria that CFCs, SF_6, and other gases experience in the mixed layer.

The undersaturated mixed layer boundary affects tracer-inferred quantities introducing differences of around 6-13% in global inventories of CFCs and SF_6 (1970-2000) compared to a saturated boundary. For NPCMW in the model, mixed layer undersaturations introduce biases as large as $\sim$20% in average CFC-derived mean TTD ages ($\Delta/\Gamma = 1$) in 2000, but small differences in C_{ant} inventory due to the relatively young age of the water.

2.6 Acknowledgments

This work was supported by NSF OCE-0825095. We thank David Darr who provided computing and programming support for the Offtrac model, David Trossman for further modeling help, and Mark Warner for insightful discussions about North Pacific CFC observations.

2.7 Figures and tables

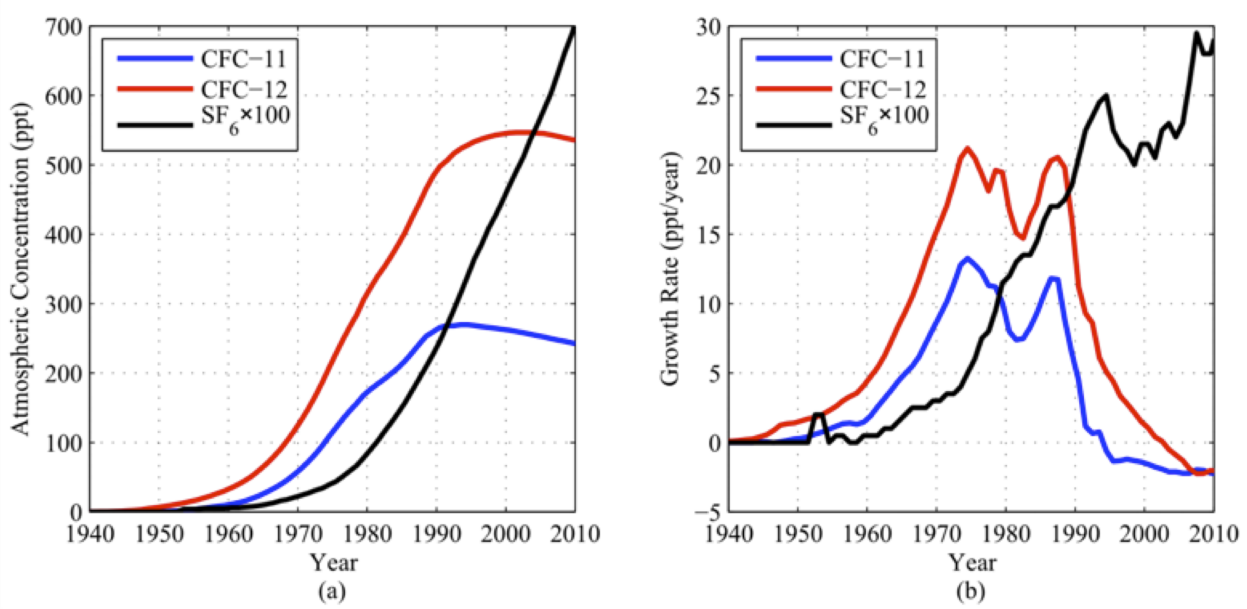

Figure 2.1: (a) Time history of atmospheric CFC-11, CFC-12, and SF_6 concentrations. (b) Time history of the atmospheric growth rate of each of these gases.

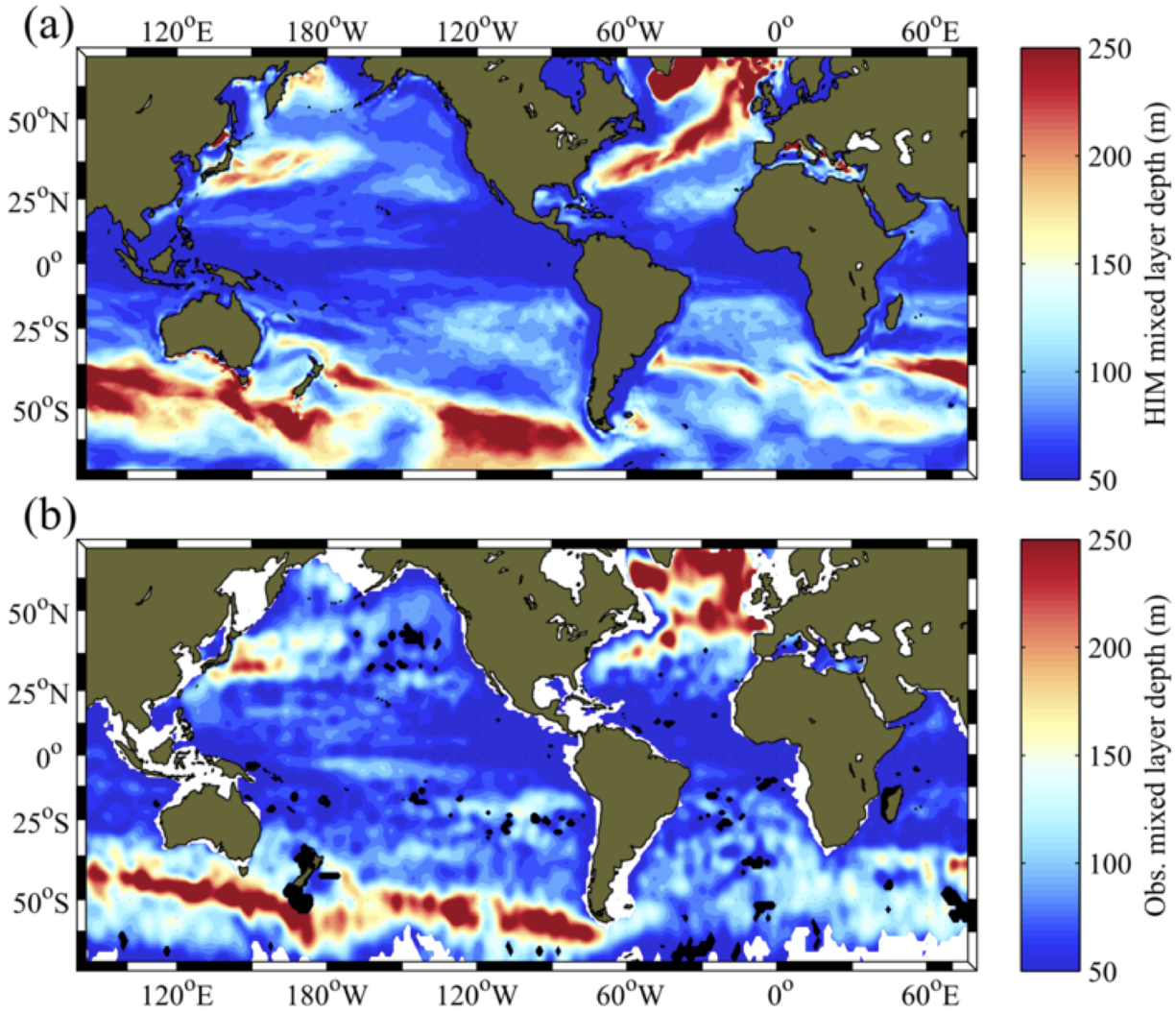

Figure 2.2: Maximum mixed layer depth: (a) in the climatological, normal-year Hallberg Isopycnal Model (HIM) run, and (b) as observed from Argo (Holte and Talley, 2009).

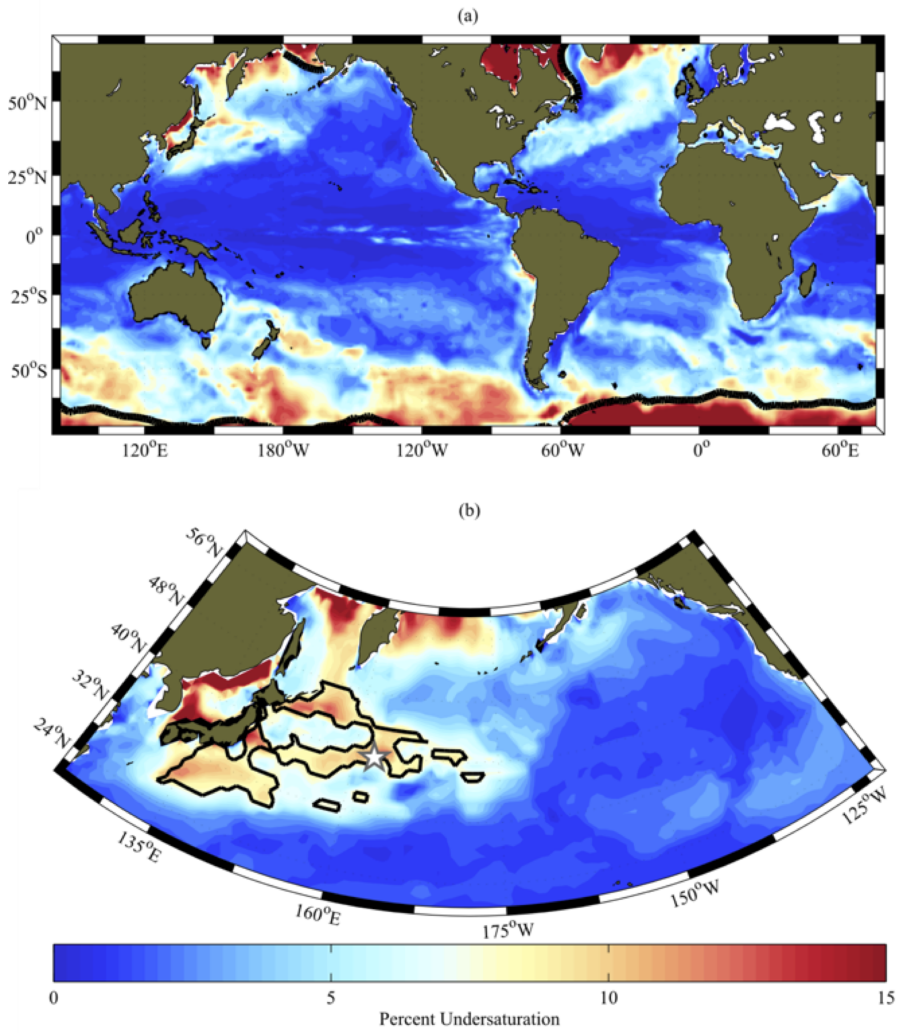

Figure 2.3: Maximum percent undersaturation of CFC-11 in 1980 in the control run (Experiment 1, Table 2.1) with offline code (Offtrac) of HIM: (a) globally and (b) in the North Pacific. Bold black contour in (a) represents ice fraction greater than 50%. Black contour in (b) represents the region where undersaturation was greater than 8% in 1980 and over which undersaturations were averaged for time series in Figures 2.4a and 2.4b and Figure 2.8. Gray star in (b) is the location of the grid point used to display seasonal cycle in Figure 2.5.

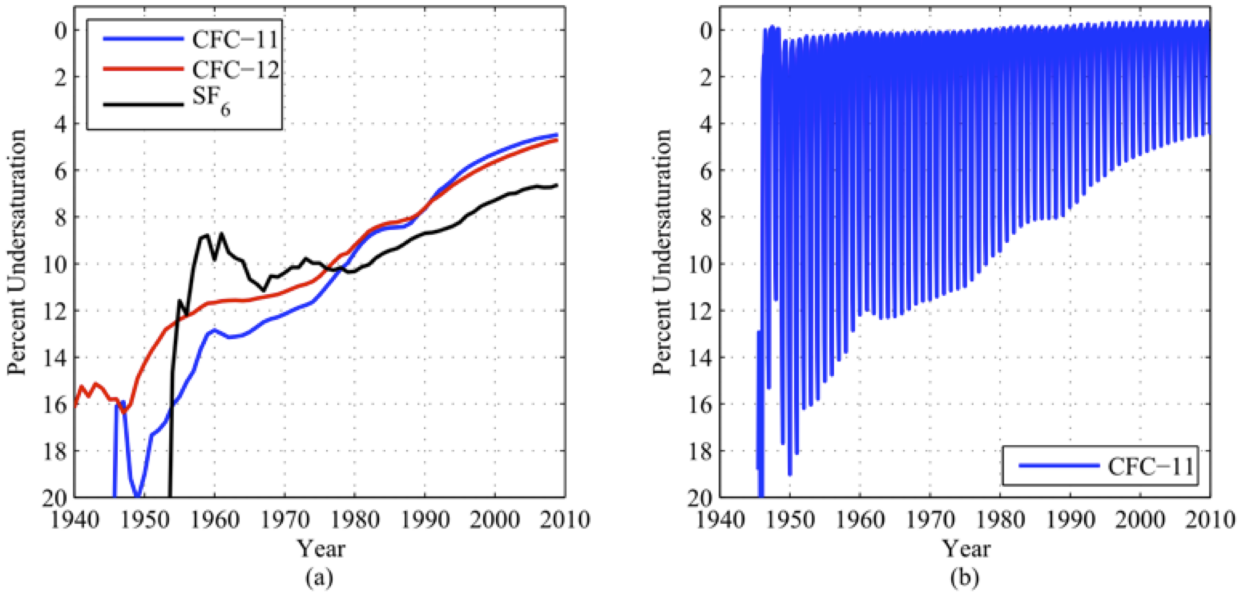

Figure 2.4: (a) Maximum annual undersaturation of each tracer in the control run (Experiment 1; Table 2.1) averaged over the northwest North Pacific region outlined in Figure 2.3b. (b) CFC-11 undersaturation for the same experiment now averaged monthly over the same region.

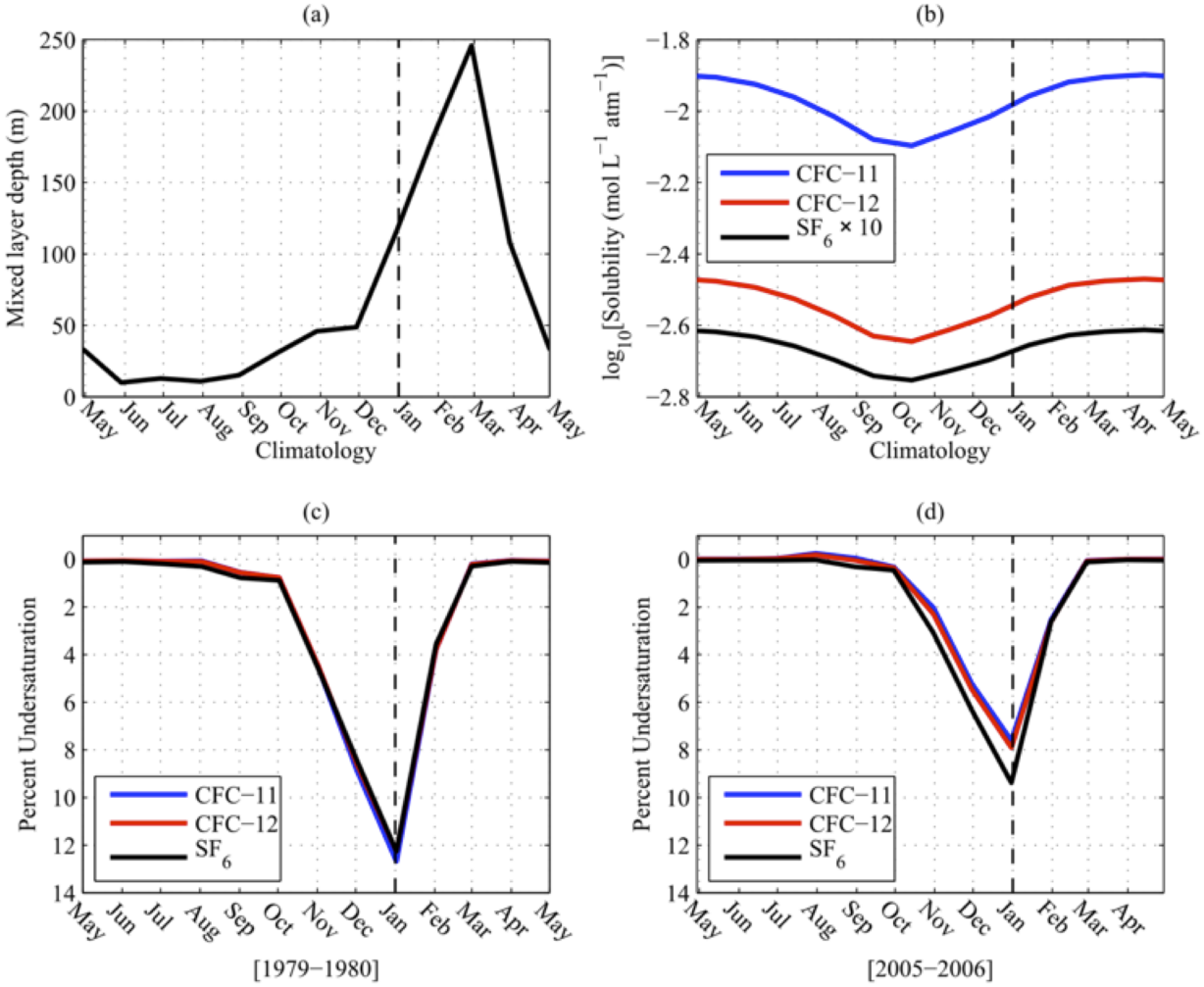

Figure 2.5: At model point 39.5^{o}N, 163.5^{o}E (gray star in Figure 2.3b), the seasonal cycle in (a) mixed layer depth, (b) solubility for CFC-11, CFC-12, and SF_6, (c) beginning of month percent undersaturation between May 1979 and May 1980, and (d) beginning of month percent undersaturation between May 2005 and May 2006. Vertical dashed line represents month of largest undersaturation.

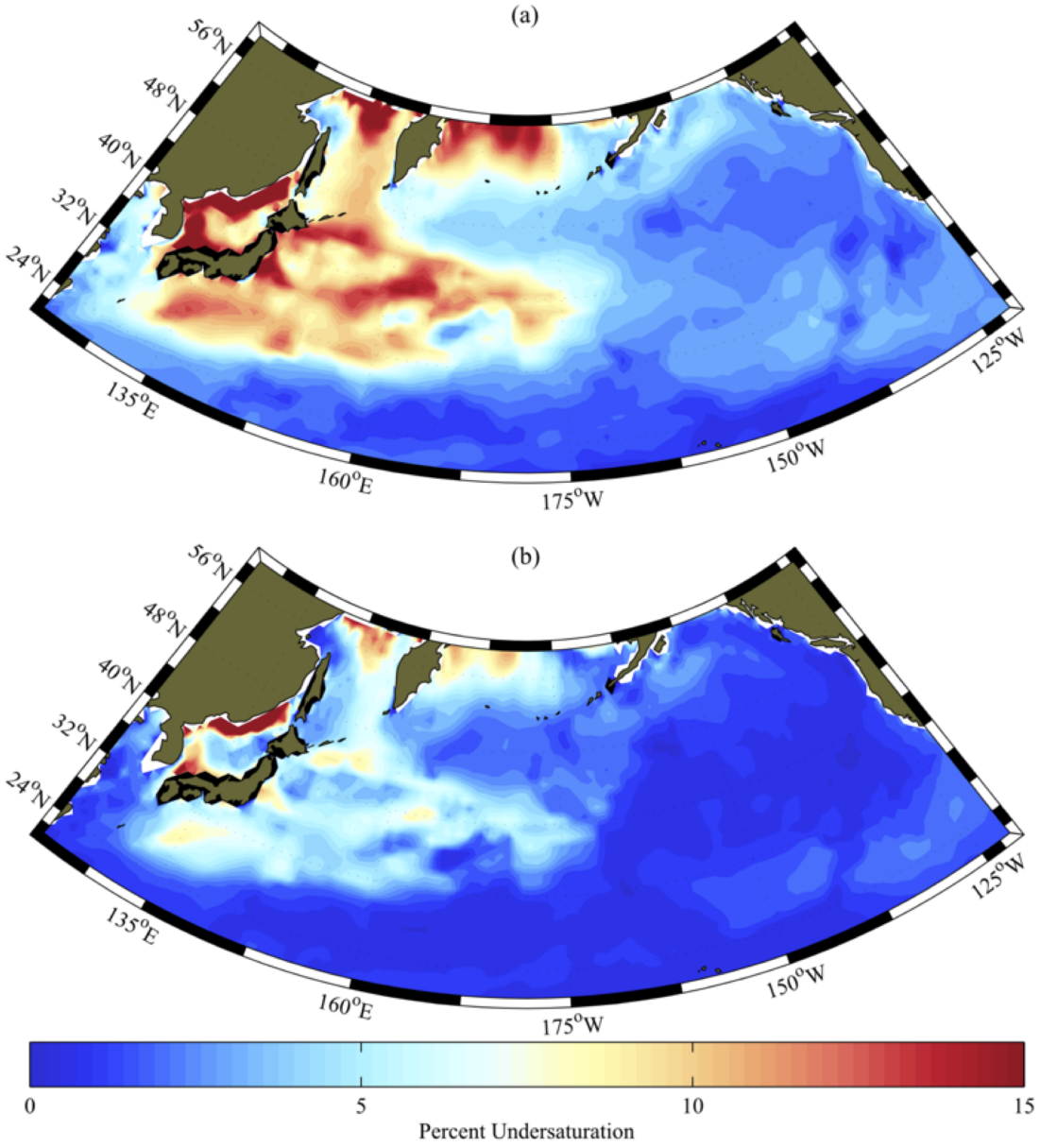

Figure 2.6: Results of gas-exchange related sensitivity experiments showing maximum undersaturation of CFC-11 in 1980: (a) Monthly varying k_w replaced with annual average (Experiment 2), and (b) globally averaged k_w scaled to value of 21.9 cm hr^{-1} (Broecker et al. (1986); Experiment 3).

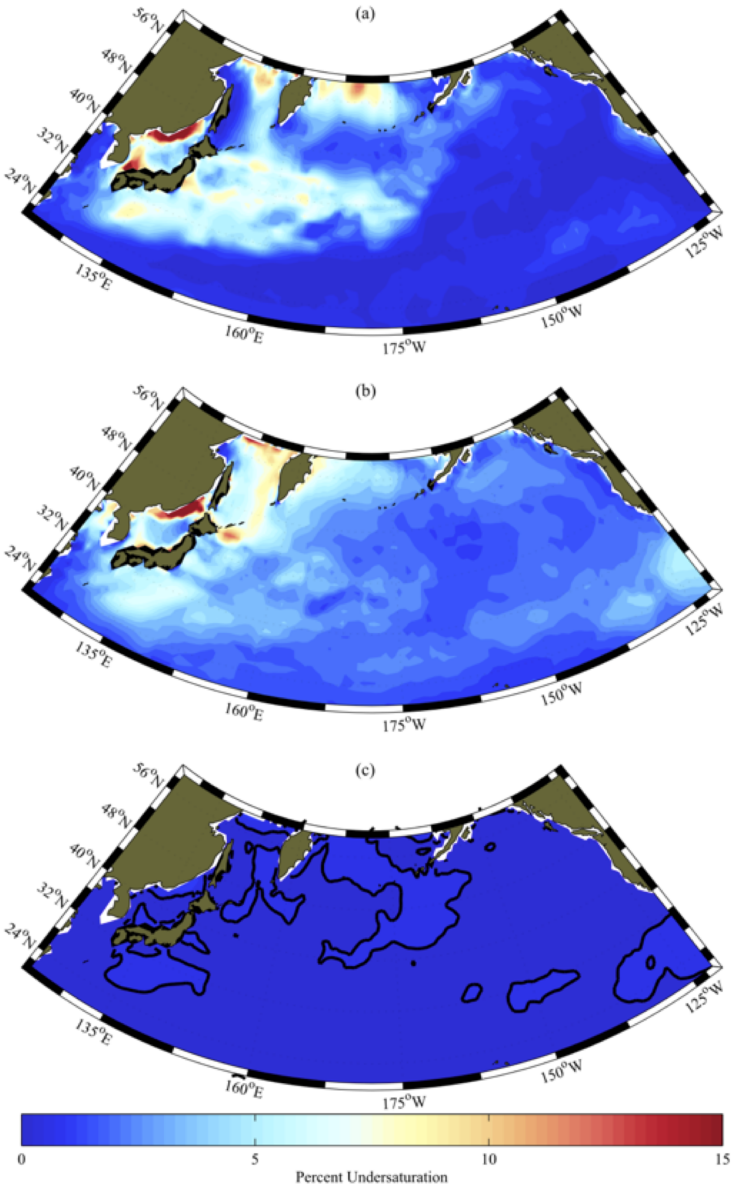

Figure 2.7: Maximum undersaturation of CFC-11 in 1980 for (a) monthly varying solubility replaced by annual average (Experiment 4), (b) assuming entrainment of underlying waters does not change mixed layer concentrations (Experiment 5), and (c) the combination of (a) and (b) (Experiment 6) where the black contour represents 0.5% undersaturation.

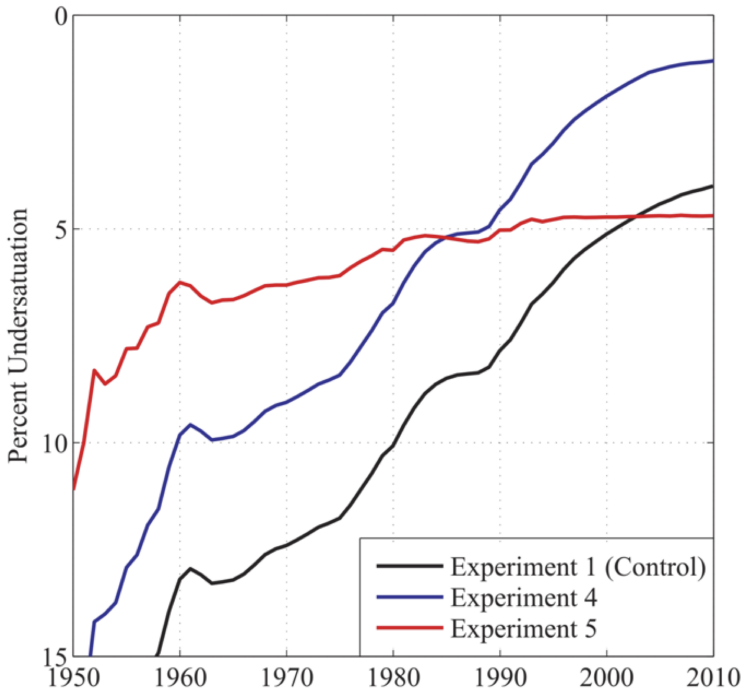

Figure 2.8: Time series of annual maximum undersaturation for CFC-11 in the control run (Experiment 1), Experiment 4, and Experiment 5 averaged over the same region shown in Figure 2.3b. See the corresponding maps of maximum CFC-11 undersaturation in 1980 in Figures 2.3b, 2.7a, and 2.7b respectively.

Experiment	Description
1 CONTROL	Monthly varying temperature, salinity, mass transport, gas transfer velocity (scaled to global average of 15.6 cm hr^{-1})[b]
2	Annually averaged gas transfer velocity for gas exchange
3	Gas transfer velocity scaled to global average of 21.9 cm hr^{-1} [c]
4	Annually averaged SST/SSS used to calculate solubility
5	Mixed layer entrainment does not change tracer concentration
6	Both modifications from Experiments 4 and 5 applied
7	Surface tracer concentrations set to saturation

Table 2.1: **Summary of Model Runs**[a]

[a] The difference to the control run (Experiment 1) is described for all other model runs.

[b] Following Sweeney et al. (2007), based on C. Sweeney [unpublished data, 2012].

[c] Based on Broecker et al. (1986).

	Age (years)[a]				Age (% Diff)[b]	
	1980		2000		1980	2000
	Exp. 7	Control	Exp. 7	Control		
CFC-11	7.3	8.3	7.5	9.3	13.8	23.9
CFC-12	7.6	8.6	8.0	9.6	13.7	19.2
SF_6	8.1	8.9	7.2	8.2	10.4	12.7
	C_{ant} Inventory (10^{13} mol)[c]				C_{ant} Inv. (% Diff)[d]	
	1980		2000		1980	2000
	Exp. 7	Control	Exp. 7	Control		
CFC-11	1.58	1.56	2.38	2.33	-1.4	-2.4
CFC-12	1.57	1.55	2.36	2.31	-1.4	-2.1
SF_6	1.56	1.55	2.39	2.36	-1.1	-1.3

Table 2.2: **Average NPCMW TTD ages and C_{ant}**

[a] TTD-inferred mean ventilation age (Γ assuming $\Delta/\Gamma = 1$ where Δ = width and 100% surface saturation) averaged over North Pacific Central Mode Water (NPCMW).

[b] Percent difference in age between Experiment 7 and control run (Experiment 1; Table 2.1).

[c] Anthropogenic carbon inventories (C_{ant}) for NPCMW based on same TTDs as used for average ages in [a].

[d] Percent difference in C_{ant} inventories between Experiment 7 and control run.

Chapter 3

PROPERTIES OF THE SUBANTARCTIC FRONT AND POLAR FRONT FROM THE SKEWNESS OF SEA LEVEL ANOMALY

Published citation: Shao, A. E., S. T. Gille, S. Mecking, and L. Thompson (2015), Properties of the Subantarctic Front and Polar Front from the skewness of sea level anomaly, J. Geophys. Res. Oceans, 120, 51795193, doi:10.1002/2015JC010723.

Abstract

The region of the Southern Ocean that encompasses the Subantarctic Front (SAF) to the north and the Polar Front (PF) to the south contains most of the transport of the Antarctic Circumpolar Current. Here, skewness of sea level anomaly (SLA) from 1992-2013 is coupled with a meandering Gaussian jet model to estimate the mean position, meridional width, and the percent variance that each front contributes to total SLA variability. The SAF and PF have comparable widths (85km) in the circumpolar average, but their widths differ significantly in the East Pacific Basin (85km and 60km respectively). Interannual variability in the positions of the SAF and PF are also estimated using annual subsets of the SLA data from 1993 to 2012. The PF position has enhanced variability near strong topographic features such as the Kerguelen Plateau, the Campbell Plateau east of New Zealand, and

downstream of Drake Passage. Neither the SAF nor the PF showed a robust meridional trend over the 20-year period. The Southern Annular Mode was significantly correlated with basin-averaged SAF and PF positions in the East Pacific and with the PF south of Australia. A correlation between the PF and the basin-scale wind stress curl anomaly was also found in the Western extratropical Pacific but not in other basins.

3.1 Introduction

The Antarctic Circumpolar Current (ACC) is the one of the most dominant, dynamical features in the Southern Ocean. It connects the Southern Hemisphere Pacific, Atlantic, and Indian Ocean basins. Much of the large-scale, eastward flow organizes into jets in three distinct regions (from north to south) the Subantarctic Front (SAF), the Polar Front (PF), and the Southern ACC Front (SACCF) Each of these fronts characterize regions where near-surface hydrographic properties change rapidly. The fronts tend to be aligned zonally with notable exceptions south of New Zealand around the Campbell Plateau, Scotia Sea and in the Brazil Basin, where large topographic features steer their paths. To first order, these fronts are in geostrophic balance resulting in jets whose zonal velocities are described by

$$u_g = -\frac{g}{f}\frac{\partial \eta}{\partial y}, \tag{3.1}$$

where u_g is the zonal geostrophic velocity, g is gravitational acceleration, f is the Coriolis frequency, and η is the geopotential height and is equivalent to the sum of the mean dynamic topography (MDT) and sea level anomaly (SLA) at any given time. The circumpolar path of these fronts was estimated using hydrographic data to define criteria describing each of these fronts (Orsi et al., 1995) yielding the traditional view of three coherent, circumpolar structures. Subsequent studies found evidence that the SAF and PF split into multiple branches in some regions, suggesting a more complicated frontal structure (Belkin and Gordon, 1996; Sokolov and Rintoul, 2002).

Since the advent of satellite observations of sea level anomaly (SLA) and sea surface temperature (SST), a number of methods have been developed to detect these fronts on smaller spatial and temporal timescales. One class of methods exploits the fact that surface properties change rapidly in the location of a front. Fronts are identified as either local maxima in gradients of sea surface height (SSH; e.g Sokolov and Rintoul (2007, 2009)) or SST (e.g. Moore et al. (1997)) or detected as a step in properties (Chapman, 2014). Gradient-based methods suffer from the problem that differentiation amplifies noise and makes it more difficult to ensure that any given maximum is related to a jet. Additionally, these methods also require an a priori choice of a threshold value.

The contour method, based on satellite observations of SLA and estimates of mean dynamic topography, is based on the intepretation of SSH contours as geostrophic streamlines. One of the earliest applications of the contour method matched density fronts from hydrographic and expendable bathythermographs to sea surface height contours from satellite altimetry south of Tasmania (Sokolov and Rintoul, 2002). They showed that these multiple branches sometimes merge to form a single strong jet or diverge to yield two weaker, but distinct, cores. Marrying the concepts of hydrographic fronts with dynamic jets, they further noted that the characteristic SSH contours of these fronts were coincident with large SSH gradients and enhanced geostrophic velocities via Equation 3.1. Under the assumption that these SSH contours represent the same front over time, this method can be used track the path of these fronts over time (Sallée et al., 2008; Sokolov and Rintoul, 2009). Recent studies have evaluated this assumption, questioning whether the SSH contours associated with the SAF and PF are actually continuously circumpolar fronts (Graham et al., 2012; Chapman, 2014) and also asking whether these contours could shift in response to steric changes in the large-scale sea level field (Gille, 2014).

The method detailed in this study is based on the findings of Thompson and Demirov (2006) (hereafter TD06) and Hughes et al. (2010) that meandering jet-like features are asso-

ciated with non-Gaussian probability density functions (PDFs) of SLA whose shape can be quantified by skewness and kurtosis. They are defined as the 3rd and 4th moments about the mean, normalized by the standard deviation:

$$\gamma_n = \mathrm{E}\left[\frac{(X-\mu)^n}{\sigma^n}\right], \tag{3.2}$$

where $n = 3$ for skewness and $n = 4$ for kurtosis, E is the expectation operator for a distribution of quantities χ with N elements χ_i defined as $\sum_{i=0}^{N} \chi_i/N$, X is measured SLA at an individual location, μ is the mean of these SLA, and σ is the standard deviation. TD06 show in a quasi-geostrophic model that skewness is positive poleward of a jet and negative equatorward. Hughes et al. (2010) find that, when used together, skewness and kurtosis describe most of the spatial variability in PDFs of SLA in the ocean. They further demonstrate that jet cores are associated with PDFs with zero skewness and low kurtosis.

In Section 3.2, we extend TD06's findings using a meandering Gaussian jet model to better understand how different properties of a jet can modify the magnitude of skewness. In Section 3.3, we apply this method to the Southern Ocean to identify the mean position, width and local effect on SLA variability of the SAF and PF. In Section 3.4, we subset the data annually to determine whether a trend exists in the meridional position of fronts from this method and also whether the interannual variability in the frontal position can be ascribed to local variability in forcing or to two large patterns of climate variability: the El-Niño Southern Oscillation (ENSO) and the Southern Annular Mode (SAM). Section 3.5 discusses our findings in the context of studies of SAF and PF variability and compares the benefits of our front detection method relative to others. Lastly, Section 3.6 summarizes the main findings of this study.

3.2 Methods and data

3.2.1 Skewness of SLA

The skewness statistic is a measure of the symmetry of a distribution whose values are largely determined by the tails of the distribution. For example, a perfectly symmetric distribution (e.g. a Gaussian) has zero skewness, a distribution whose right tail is thicker than its left tail (e.g. an Inverse Gaussian) has positive skewness, and a distribution whose left tail is thicker than its right tail has negative skewness. TD06 showed that the presences of eddies as well as strong geostrophic currents can cause strong non-zero regions of skewness. An eddy field dominated by either cyclonic or anti-cyclonic rotation can result in an SLA distribution with negative or positive skewness respectively. Using an idealized quasi-geostrophic model and skewness calculated from satellite altimetry, TD06 further demonstrated that oceanic jets have a distinct signature: skewness will be negative equatorward of a jet, where the average SSH is higher, but contains some lower values when the jet meanders towards the equator. As a result, the distribution tails off to the left with some negative values of SLA (Figure 1d). An analogous argument explains why skewness is positive poleward of a jet (Figure 1b).

3.2.2 The Gaussian meandering jet model

Description of the idealized jet model

To be able to investigate the location and size of the skewness transition, we consider an idealized model for a meandering jet (Figure 3.1) which has a purely zonal Gaussian velocity profile and meanders in time according to

$$u_g(y,t) = u_0 \exp\left(-\frac{[y-\bar{y}+\delta(t)]^2}{\sqrt{2}L}\right), \tag{3.3}$$

where y is the distance from the jet center, t is a time variable, u_0 is the maximal zonal velocity (assumed to be constant in time), $\bar{y}$ is the mean position of the jet, $\delta(t)$ is a normal distribution with zero mean and a standard deviation σ which represents the distance over which the jet meanders, and L is the width of the jet (Gille, 1994). Using the geostrophic relationship (Equation 3.1), the corresponding SSH will be

$$\eta_g(y,t) = \eta_0 \text{ erf}\left(\frac{y - \bar{y} + \delta(t)}{\sqrt{2}L}\right), \tag{3.4}$$

where η_0 is equal to $(\pi/2)^{1/2}\ fLu_0/g$ and can be interpreted as the size of the SSH jump associated with the jet. Averaging in time yields the equivalent of mean dynamic topography, $\bar{\eta}_g(y) = \eta_0 \text{ erf}\left((y-\bar{y})/\sqrt{2}L\right)$. Here $\eta_g(y,t)$ represents an ocean in which all variability is associated with meandering currents, whereas the Southern Ocean also contains a large number of coherent eddies (e.g. Keffer and Holloway (1988); Fu (2009)). The total SLA (e.g. as observed by a satellite) from both the meandering jet and the eddy field is then

$$\eta_{obs}(y,t) = \eta_g(y,t) + A_\phi \phi(y,t), \tag{3.5}$$

where A_ϕ is the amplitude of the sea level anomaly from the eddy field and $\phi(y,t)$ is a structure function representing the SLA of the eddy field, which we assume to be approximated by white noise (discussed in further detail in the next section).

Despite ϕ having a mean of zero, the ratio between η_0 and A_ϕ does affect the skewness, because if A_ϕ is larger than η_g the SLA distribution is dominated by noise rather than the SLA of the jet. This can be interpreted as a signal to noise ratio (SNR $= \eta_g/A_\phi$) where the SLA of the the jet (η_g) is analogous to the signal, and eddy variability (A_ϕ) represents noise. Rewriting Equation 3.5 using the SNR term yields

$$\eta_N(y,t) = \text{SNR erf}\left(\frac{y - \bar{y} + \delta(t)^2}{\sqrt{2}L}\right) + (1 - \text{SNR})\phi(y,t) \tag{3.6}$$

where η_N refers to the SLA profile that is composed as a sum of the jet and the eddy field. Using results from Gille (1994), the meander distance σ is set to 1.7 times the width of the jet. Each of the model parameters have been summarized in Table 3.1 for reference.

A skewness curve can be generated using a Monte-Carlo simulation by choosing values for the three free parameters $\bar{y}$, L, and SNR and drawing 1000 samples from $\delta(t)$. This large number of samples helps ensure that the random numbers used as an analog for the meandering of the jet and for eddy variability have zero skewness. An example for a purely zonal, meandering, Gaussian jet in the Southern Ocean with $\bar{y} = 60°S$, $L = 80$km, $\sigma = 136$km, and SNR $= 0.8$ is shown in Figure 3.1, with meridional profiles of SLA in panel (a). By construction SSH is negative south of the jet and positive north of the jet (Figure 3.1a), as discussed previously. Resulting SLA distributions at 62°S (Figure 3.1b) and 58°S (3.1d) are skewed while the PDF at the center of the jet, 60°S has close to zero skewness (Figure 3.1c).

Relationship between skewness and model parameters

Plots of SLA skewness in TD06 were normalized such that the maximum or minimum of the skewness transition was equal to 1. In the example (Figure 1), skewness reaches a maximum of around 1.5. Here, we vary the shape parameters in Equation 3.6 individually to gain insight into how the properties of the jet can affect the skewness of the resulting SLA distribution. The mean position parameter $\bar{y}$ has no effect on the magnitude of the skewness, but does shift the zero crossing of the skewness curve (not shown). The effects of the other two shape parameters, L and SNR, on the skewness transition were determined empirically. To investigate L, the same parameters as those shown in Figure 3.1 were used but L was allowed to vary from 20 to 120km. Similarly to investigate SNR, L was set fixed to 80km, but SNR was allowed to vary from 0.01 to 1. This empirical sensitivity test shows that the maximum skewness is inversely proportional to the jet width L (Figure 3.2a) and

that SNR has the largest impact on the maximum skewness. An SNR of approximately 0.6 is required for the signal of the jet to be distinguishable from eddy variability (Figure 3.2b). Additionally, this dependence on SNR suggests that regions where a meandering jet dominates SLA variability will likely have large skewness transitions allowing for an objective identification of the strength of the jet.

In the examples above and for the remainder of this study, we assume that the eddy SLA signature (ϕ in Equation 3.6) can be modeled as white noise. This is potentially problematic as eddy variability has been estimated to be spatially correlated on length scales up to about 85km (Gille and Kelly, 1996). To test the effect of this assumption, we performed the same sensitivity analysis using red noise with spectral slopes from -2 to -5 (which covers the range reported in the literature e.g. Xu and Fu (2011) and McCaffrey (2014)) and a wavelength rolloff beginning at 85km. Both the magnitude of skewness (Figure 3.2) and the shape of the skewness curve (not shown) were affected minimally by the spectral content of the noise. In the case where L varied with a fixed SNR, the maximum skewness with white noise was 5% lower than with red noise. Sampling multiple realizations of the red noise in time yielded Gaussian PDFs, implying that the spatially-distributed red noise when sampled in time behaves like white noise.

Jets may be in close enough proximity to each other such that their velocity envelopes overlap (Gille, 1994). To investigate the impact on skewness of two jets in close proximity, we simulate this case under the assumption that the jet-jet interactions are linear (not shown). Skewness is a nonlinear statistic and so the individual skewness profile of each jet cannot be linearly summed (see Appendix A in Hughes et al. (2010)). Here we find that for two jets a and b, if the distance between their centers $|\bar{y}_0^a - \bar{y}_0^b|$ is less than the sum of their widths $L_a + L_b$, only one skewness transition will be observed, asymmetrically centered around the peak of the summed velocity. The zero crossing of this skewness transition still corresponds roughly to the average of the two jet centers. When applied to observed skewness, this implies

that given an asymmetric skewness transition the zero crossing is still a robust estimate of jet locations. However in regions where multiple jets overlap, our use of a single Gaussian may yield overly broad estimates of the jet width.

3.2.3 Application to the Southern Ocean

To determine ACC jet positions from observations, we use the delayed-time, reference along-track SLA product provided by AVISO. This product represents a continuous measurement record from the TOPEX/Poseidon, Jason-1, and Jason-2 satellite missions. Each satellite measures along a fixed reference orbit with 254 ground tracks (127 descending and 127 ascending). SLA measurements are repeated every 9.9 days from 25 September 1992 to 7 August 2013 with an approximate 10 km along-track resolution. Unfiltered along-track data are used for this study rather than a gridded product, because the gridding process affects higher moment statistics such as skewness (Sura and Gille, 2010). Additionally, in the Southern Ocean the first baroclinic Rossby radius of deformation ranges between 10 km and 30 km (Chelton et al., 2011) and is better resolved by the along-track data than by the gridded product. The added measurement noise associated with the unfiltered data is assumed to be white noise and is incorporated as part of the A_ϕ term.

Following TD06, we calculate skewness of SLA along every track to show regions in the Southern Ocean where skewness transitions from positive to negative. Throughout this study, skewness was calculated using a biased estimator (differences using an unbiased estimator were negligible). The positions of the middle branches of the SAF and PF estimated by Sokolov and Rintoul (2009) (red and blue lines, Figure 3.3) roughly follow regions where skewness transitions between positive (red) and negative (blue) values. The along-track skewness of SLA from the entire altimeter record on ground track 6 shows these distinct skewness transitions more clearly (the two largest indicated by the blue and red colored portions of the skewness curve in Figure 3.4). The skewness is fairly noisy on this track

(and on all others) which leads to false positives when trying to identify skewness transitions by eye. In Section 3.4, the skewness of SLA was calculated based on annual subsets of the data between 1993 and 2012, when measurements of SLA were collected over the entire year. To evaluate the sensitivity of our results to using calendar year subsets of the data, we perform the same analyses over a year beginning in April and ending in March (which is more representative of ENSO (Stein et al., 2010)).

The following algorithm is applied to each track in order to consistently identify skewness transitions associated with either the SAF and the PF. First, the latitude bounds in which we look for skewness transitions are chosen to restrict the analysis to the ACC. Here we use the Sokolov and Rintoul (2009) estimates of the middle branches of the SAF and PF as the basis for the envelope. Their estimates of front location are also based on satellite altimetry and more precise than the hydrographic estimates of (Orsi et al., 1995), though our results should not be sensitive to this choice, as the estimates from Sokolov and Rintoul (2009) broadly agree with those of Orsi et al. (1995). The northern bound of our search envelope is 5°equatorward of the SAF-M, and the southern bound is 5° poleward of the PF-M. Second, either the maximum or the minimum of a skewness transition must be statistically significant. In this study statistical significance is determined using a bootstrap method (Efron and Tibshirani, 1994) at the 95% confidence level. Alternatively, a significance level can be calculated directly using the standard error of skewness: $\sqrt{[6n(n-1)]\,[(n-2)(n+1)(n+3)]^{-}1}$ where n is the number of samples (Fisher, 1930). Lastly, because the largest skewness transitions should be associated with strong jets (i.e. higher SNR), the two largest skewness transitions along each track are chosen. In this study, the northern transition is referred to as the SAF and the southern one is referred to as the PF. Note here that these labels are used because these transitions tend to roughly align with the SAF and PF locations from Sokolov and Rintoul (2009). However in the absence of any other information (e.g. SSH or SST gradients) these frontal locations may actually correspond to other strong fronts such as the SACCF, the

Subtropical Front (Graham and De Boer, 2013), or a different branch of the same front.

For each of these skewness transitions, the shape parameters $\bar{y}$, L, and SNR are determined by a nonlinear least squares fitting routine minimizing the normalized sum of squared residuals (NSSR) $\sqrt{(\gamma_{obs} - \gamma_s)^2/(N-3)}$ where γ_{obs} is the observed skewness, γ_s is the skewness derived from the Monte-Carlo simulation in Section 3.2, N is the number of data points used to fit, and the 3 arises from the number of free model parameters. Based on examining a number of fitted curves, we define a good fit where NSSR is < 0.2. This fitting method relies on randomly drawn samples and so is susceptible to uncertainty in the shape parameters. To estimate the inherent error in this method, we generated 100 independent skewness curves using the Monte-Carlo method described in Section 3.2 with $L = 100$ km, $\bar{y} = -50°$, and SNR=0.8 and evaluated if the fitting routine can reproduce the parameters. When the number of simulated measurements is large (here 700, a number similar to the full data record), the difference between the actual and estimated values for L was 20 ± 1 km, $\bar{y}$ was $0.1 \pm 0.01°$, and SNR was 0.08 ± 0.01. However, when applied to smaller subsets (i.e 36 measurements, similar to the size of the annual distributions of SLA), the mean position of the front, $\bar{y}$, is still well-constrained, but L and SNR are not. This behavior arises from the sensitivity of skewness to outliers. For a large number of samples, this effect is suppressed, but for smaller realizations, the Monte-Carlo method used here does not consistently generate the same width or magnitude of the skewness transition. Lastly, The width estimates of the jet may be biased because the satellite tracks are not necessarily perpendicular to the axis of the jet. In this case the width that a satellite 'sees' may be artificially broadened and give the along-track width.

3.3 Long-term mean position and width

As an initial investigation of the accuracy of the method, we compare the estimated mean jet positions from our method with those determined by the frontal positions from Sokolov

and Rintoul (2009). In general, consistent with previous studies (Orsi et al., 1995; Graham and De Boer, 2013), we find that frontal locations align along zonal ridges and are steered around areas of significant topographic features (Figure 3.5a). Dynamically, this topographic control is due to near conservation of potential vorticity (PV) along the path of a fluid parcel which in the barotropic framework is f/H, where f is the Coriolis frequency, and H is the height of the fluid (Marshall, 1995). If the fluid encounters a ridge, H decreases, so f must also decrease to conserve PV, implying an equatorward deflection.

South of Africa between 0 and 30°E, the SAF (red line in Figure 3.5a) flows across a small abyssal plain before reaching the Southwestern Indian Ridge (30° to 50°E) where the front is primarily constrained along the southern boundary of the ridge. The path then diverts around the northern edge of the Kerguelen Plateau (60° to 80°E) and flows gradually southward along the northern part of the Southeast Indian Ridge (80° to 140°E). It is then steered sharply southward around the Campbell Plateau (170°E) before steering northward again along the northern outskirt of the Pacific Antarctic Ridge (170° to 230°E) until the ridge turns sharply northward at 240°E. The SAF then flows across the Bellingshausen Basin (240° to 300°E) before entering Drake Passage at 300°E. The front turns sharply northward along the South American continental shelf before crossing the Argentine Abyssal Plain (300° to 350°E) and traversing the southern tip of the Mid-Atlantic Ridge.

The PF (blue line in Figure 3.5a) follows topographic features similar to those followed by the SAF. At the Southwest Indian Ridge, the PF and SAF are located within a few degrees of each other. The PF then sharply diverges from the SAF at Kerguelen Plateau southward through a small dip in the Plateau south of the Kerguelen Islands. It then tracks the crest of the Southeast Indian Ridge closely before traversing it at around 220°E and flows south along the southern part of the Bellingshausen Basin. The PF and SAF begin to converge through Drake Passage (but remain distinct from each other) until they traverse the Mid-Atlantic Ridge (around 340°E).

The width of both the SAF (87 ± 10km) and PF (80 ± 8km) are similar when averaged over their circumpolar paths. As a caveat when comparing these to other estimates of jet widths in the ACC, these quantities refer to the along track, Gaussian width of each jet's velocity profile. Our estimates are almost twice as wide those in Gille (1994) potentially because of our assumption that each front represents a single Gaussian jet. As discussed in Section 3.2, two jets whose velocity envelopes overlap appear as a single, broad skewness transition.

The largest differences in width between the SAF and PF occur when their paths are the furthest apart (180°E and 240 to 300°E) where the PF narrows to around 60 km. The narrowing of the PF may be a result of changes in the baroclinic Rossby radius (Chelton et al., 2011) which decreases poleward. In addition, topography appears to influence the width of the SAF and PF (Figure 3.5). In the region of the Kerguelen Plateau (60° to 80°E), the PF width decreases from 90 km to about 75 km and the SAF narrows downstream (80°E) from around 100 km to 80 km. The SAF also narrows after passing the Southeast Indian Ridge. When both fronts reach the Campbell Plateau (170°E), the flow constricts significantly with the PF narrowing from 90 km to nearly 50 km and the SAF narrowing from 100 km to 70 km. The SAF broadens over the Bellingshausen Basin after the Pacific Antarctic Ridge, whereas the PF reaches its narrowest width (other than the Campbell Plateau). The larger spatial variability of the PF's width and position compared to the SAF may be related to the PF's proximity to strong topographic features. For example in regions near strong topography, the branches of the PF are restricted to a smaller meridional region which may sharpen the jets themselves or reduce the distance between jet cores, both of which would result in narrower widths.

The SNR of the PF anticorrelates with its width, suggesting that when the jet narrows because of topographic meridional constraints, the PF tends to have a stronger signature in SLA. In these regions, topography tends to constrain the flow to organize into a smaller

number of jets. If the overall transport does not change in this region, then the velocities of these jets must increase, which would yield a higher signature in SLA (Graham et al., 2012). Similarly, the SNR of the SAF decreases over abyssal plains (e.g. 180° to 200° and 240° to 300°) where the lack of topography permits the SAF to become a more diffuse feature or to split into multiple jets (Thompson and Sallée, 2012). Curiously in the Indian Ocean (30°to 120°E), both the SAF and the PF tend to have relatively low SNRs despite the strong topography in that basin.

3.4 Temporal variability in frontal locations

The long-term features of the SAF and PF (i.e. the mean path, width, and SNR) seem to be heavily controlled by bathymetry. However on shorter timescales, the ACC may have significant variability caused by changes in the Southern Ocean westerly winds (Allison et al., 2010) or that may be internally generated variability in the ocean. To determine how much the SAF and PF vary interannually, the mean latitude of each front is calculated by averaging the centers determined from the annual subsets of SLA over 5° longitudinal sectors (centered at 2.5°E, 7.5°E, etc.).

As a simple measure of the variability in the locations of these two fronts, the standard deviation (σ_y) of the annual frontal position in each longitudinal sector between 1993 and 2012 was calculated. The SAF's σ_y (red line in figure 3.6a) remains fairly constant geographically with an average of 110 ± 40km. In contrast, the PF (blue line in Figure 3.6a) generally has much higher variability (170 ± 57km) and shows four distinct regions where σ_y is large: (i) the Brazil Basin (300°E), (ii) in the Bellingshausen Basin (260°E), (iii) along the Southeast Indian Ridge (190°E), (iv) upstream of Kerguelen Plateau at Elan Bank (60°E). The elevated peak in region (i) is relatively narrow and may be an artifact of our methodology, which may be picking a more southern branch of the SAF or the PF in some years. In region (ii), the PF flows over an abyssal plain which leaves the jet free to wander over a

wide meridional range without modifying its PV.

In regions (iii) and (iv), the PF either flows very near to or over topographic obstruction, suggesting a relationship between variability in jet positions and topography, an interaction discussed by Thompson and Richards (2011). Strong topography causes large changes in PV, and interactions with the mean-flow can cause a jet to drift toward low PV gradient regions (see Thompson and Richards (2011) Section 3.2 for more details) before the jet eventually dissipates. The peak in PF variability at 190°E might be explained by this mechanism, with the PF being close to the ridge in some years and further northward in other years as it migrates away from the sharp topographic gradient. At (iv), Elan Bank represents a bathymetric feature around which the flow may bifurcate. The enhanced variability here may then be related to the 'jet jumping' mechanism described by Chapman and McC. Hogg (2013) and Chapman and Morrow (2014) in which transport can transition from one jet to another on yearly or slower timescales. As our method would preferentially choose the stronger jet, this would result in higher variability in the mean position of the PF.

In addition to the frontal meridional variability, two other potential features of interannual variability in the ACC are considered: long-term meridional trends and changes in meridional position in response to climate modes of variability. We evaluate the significance of trends and correlations at a 90% significance level of ($p < 0.1$).

The poleward trend in wind stress related to the contraction of the polar vortex (Marshall, 1995) has led to the hypothesis that the ACC might respond with a similar poleward shift. Evidence for this exists in some observational studies (Sallée et al., 2008; Sokolov and Rintoul, 2009) and some low-resolution modeling studies (Saenko et al., 2005; Fyfe and Saenko, 2006). However, here we find that neither the SAF nor the PF has a statistically significant trend averaged over their entire circumpolar paths. On smaller spatial scales, the PF has no statistically significant trends (blue dots in Figure 3.6b) whereas the SAF displays some sectors with statistically significant trends (red stems in Figure 3.6b). Just 8 of the 72 5°-

wide sectors have statistically significant trends. These are likely spurious false positives considering that sectors neighboring the significant regions are often of the opposite sign, and the trends lack any coherent, zonal structure. Additionally, none of these same sectors show statistically significant trends in the ENSO-year analysis. These results suggest that a robust signature of a trend cannot be found in any basin.

SAM is the dominant mode of atmospheric variability in the Southern Hemisphere and can modify surface wind stress particularly in the eastern Indian Ocean, southwest Pacific Ocean, and (to a lesser extent) Atlantic Ocean (Gong and Wang, 1999). ENSO is one of the leading modes of global climate variability with atmospheric teleconnections to the Southern Hemisphere that project strongly onto SAM (Cai et al., 2011; Ciasto and Thompson, 2008). Indices of the strength of SAM and ENSO are taken from those made available by the Ocean Observations Panel for Climate (http://ioc-goos-oopc.org/). These indices were annually averaged to match the same annual timescales for which skewness was calculated.

Correlations of SAM with mean SAF and PF latitude in the 5° longitudinal sectors yield only a handful of statistically significant locations (Figure 3.7a). As with the long-term trends, the significant correlations between SAM and the SAF position tend not to be spatially coherent except potentially in the southeast Indian Ocean (120° to 180°). This may be due to the combination of SAM being particularly strong in this region and a relative lack of topography to the north of the jet allowing the SAF to shift in response to large SAM events. However, once again these correlations might be false positives as no two neighboring sectors show significant correlations to SAM. For example, the sectors at 142.5°E and at 152.5°E are of opposite sign. No coherent signal can be seen between SAM and the PF. Likewise, the statistically significant correlations between ENSO and these fronts are too random to indicate a strong relationship (Figure 3.7b). Similar to the trend analysis, these sectors are also not significant in the ENSO-year analysis.

To examine basin-scale variability in SAF and PF location, we divide the ocean into

Atlantic (300° to 25°E), West Indian (25° to 100 °E), south of Australia (100° to 180°E), West Pacific (180° E to 230 °E), and East Pacific (230° to 300°E) sectors. An index of variability for position of the SAF and PF in each ocean basin is calculated as the mean latitude of the frontal positions within each of those defined sectors. To examine whether local variability in forcing can cause variabilty in each basin, the first empirical orthogonal function (EOF) of monthly wind-stress curl (WSC) anomaly from the ERA-interim reanalysis (Dee et al., 2011) is calculated in each basin within 10 degrees of the ACC. The 1st mode of this EOF is used as an index of variability. Every basin's EOF has a SAM-like response with a shift of the WSC southward for positive phases of the local index of variability.

These basin-scale averages of the position of the SAF and PF lead to higher correlations (Figure 3.8) compared to the track-by-track investigation. In the East Pacific, both the SAF and PF mean latitude correlate strongly ($p < 0.05$) with SAM, suggesting that both fronts shift slightly northward (the SAF by 39km and the PF by 20km during 1σ positive SAM year). This is also the region where topographic features may have little influence because of a relatively large abyssal plain. SAM is also anticorrelated with the PF south of Australia, where the loading pattern is particularly strong, representing a shift southward of the PF of about 41km for a 1σ SAM event. ENSO does not correlate significantly with either the PF or SAF in any basin, though the strongest correlation occurs with the SAF in the East Pacific where ENSO originates. In the West Pacific, wind-stress curl is the only significantly correlated forcing of the PF. Despite the strong influence of SAM here, the 1st mode EOF of WSC is not significantly correlated to the SAM index. The lack of correlations in most basins suggests that the relationship between the SAF and PF latitudinal position may not be directly related to large-scale wind-forcing.

3.5 Discussion

The lack of long-term trends and the weak correlations with SAM and ENSO reported above

is counter to the other studies (Sokolov and Rintoul, 2009; Sallée et al., 2008; Kim and Orsi, 2014) that use the SSH contour method to infer frontal position variability. Part of the disparity may arise from the fact that the results discussed here rely on annual estimates of frontal positions and ignore the possibility that the relationships to SAM occur on shorter or seasonal timescales. However recent studies have noted a significant downside in using the contour method to infer temporal variability, notably that SSH contours may not be co-located with strong gradients in SSH along the entirety of their circumpolar path (Chapman, 2014; Graham et al., 2012). In particular Graham et al. (2012) argue that in these regions with weak gradients, SSH contours can migrate in time without necessarily corresponding to a change in transport which may lead to erroneous estimates of temporal variability.

Our finding that the path of the ACC is insensitive to changes in the large-scale wind field aligns with a number of other studies using independent methodologies. Gille (2014) diagnosed the meridional variability of the ACC by calculating the zonally-averaged geostrophic transport-weighted latitude and found no long-term trend and only a weak correlation with SAM. In an analysis of historical model runs submitted to the fifth Coupled Model Intercomparison Project, the ACC was found to not shift significantly in response to a poleward migration of Southern Ocean westerlies (Meijers et al., 2012). In a high-resolution coupled climate model configured for 21st century warming scenario, Graham et al. (2012), showed that the position of the ACC remained virtually unchanged despite an overall shift in the westerlies of 1.3° poleward. Domingues et al. (2014) using a combination of in-situ and satellite observations south of Africa found that the positions of the SAF and PF fronts were uncorrelated with SAM.

The methodology introduced in this paper is an alternative method to detecting fronts in the Southern Ocean (and perhaps elsewhere). It is relatively simple to implement, as skewness can be calculated directly from SLA without incorporating estimates of MDT. Additionally, unlike many other jet finding schemes that require an a priori estimate of

the number of fronts to find or thresholding criteria (Chapman, 2014), this method can be modified to be entirely objective. Using the standard error of skewness, a significance threshold can be calculated and compared to the along track skewness (see Figure 4) to find statistically significant transitions. If only the mean position is needed, we found that extrapolating the zero skewness crossing using a linear fit to the skewness transition is a good approximation to the more complicated nonlinear fitting routine employed in this study (not shown, but note the roughly linear transition from positive to negative skewness in Figure 1a between -62°and -58°). Also, because higher SNR corresponds with higher maximum skewness, jets can be ordered in terms of relative strength based on the magnitude of the transition.

This method has a number of limitations that could be improved upon in future studies. Other detection methods provide a picture of the ACC as being comprised of closely spaced jets (Chapman, 2014; Sokolov and Rintoul, 2009). This suggests that perhaps the SAF or PF could better approximated by a double Gaussian jet model (Gille, 1994; Hughes et al., 2010); further investigation however must be done to determine whether this increases the number of free parameters beyond a tractable limit. Lastly, particularly for studies that attempt to find every possible jet along a track, a kurtosis criterion could also be enforced when choosing skewness transitions, following the finding of (Hughes et al., 2010) that low kurtosis represents a barrier to mixing.

3.6 Conclusions

In this study, we used a Monte-Carlo simulation based on a meandering Gaussian jet model to demonstrate that a jet's width and SNR modulate the skewness signature first explored by TD06. Coupling this with a fitting routine allows for the robust identification of jets from the along track SLA dataset. Unlike many other frontal detection schemes, no estimates of MDT are required, ensuring that any temporal variability in frontal location is unaffected

by large-scale SSH changes. Also, this method requires no threshold criterion to be defined and any skewness transition that exceeds a statistical threshold potentially corresponds to a jet-like feature.

This method was then applied to the SLA in the Southern Ocean where the two largest skewness transitions along each satellite track were identified. The northern one was assumed to be the dominant branch of the SAF and the southern one was assumed to correspond to the PF. In accordance with previous studies, we find that the path of the SAF and PF closely track the underlying bathymetry. These jets narrow downstream of strong topographic features such as the Kerguelen Plateau, the Campbell Plateau, and the Pacific Antarctic Ridge, and they widen over the Bellingshausen Basin suggesting that topography may play a role in controlling the width of jets in these regions. Additionally, downstream of topographic obstructions, the SNRs of both the SAF and PF decrease, suggesting that lee effects cause enhanced eddy activity in these regions and/or that the jets become less stable.

Lastly, we find that between 1993 and 2012, the ACC as a whole and on regional spatial scales has not exhibited significant meridional trends in contrast with other studies. The ACC was also shown to be relatively insensitive to climate mode-induced variability except in the East Pacific where SAM is correlated with changes in the basin-averaged SAF and PF position (a northward shift for positive SAM) and anticorrelated with the PF south of Australia (southward shift for positive SAM).

3.7 Acknowledgments

This work was supported under grants from NSF (OCE-1059886) and NASA (NNX13AE44G). We thank two anonynous reviewers whose comments and suggestions greatly improved this study. The along track sea level anomaly data used for this study were produced by Ssalto/Duacs and distributed by Aviso, with support from CNES (http://www.aviso.altimetry.fr/). Zonal and meridional wind speed obtained from the ECMWF ERA-Interim atmospheric re-

analysis was also used in this study (http://apps.ecmwf.int/datasets/data/). SAF and PF frontal positions presented in this paper are made available by request from the corresponding author.

Table 3.1: Description of the parameters in the meandering Gaussian jet model described in Section 3.2

Symbol	Parameter Description
L	The width of the Gaussian velocity profile
$\bar{y}$	The time mean position of the jet
σ	The distance over which the jet meanders. Set to $1.7L$ per Gille (1994)
SNR	The ratio of SLA variability due to the jet compared to the eddy field

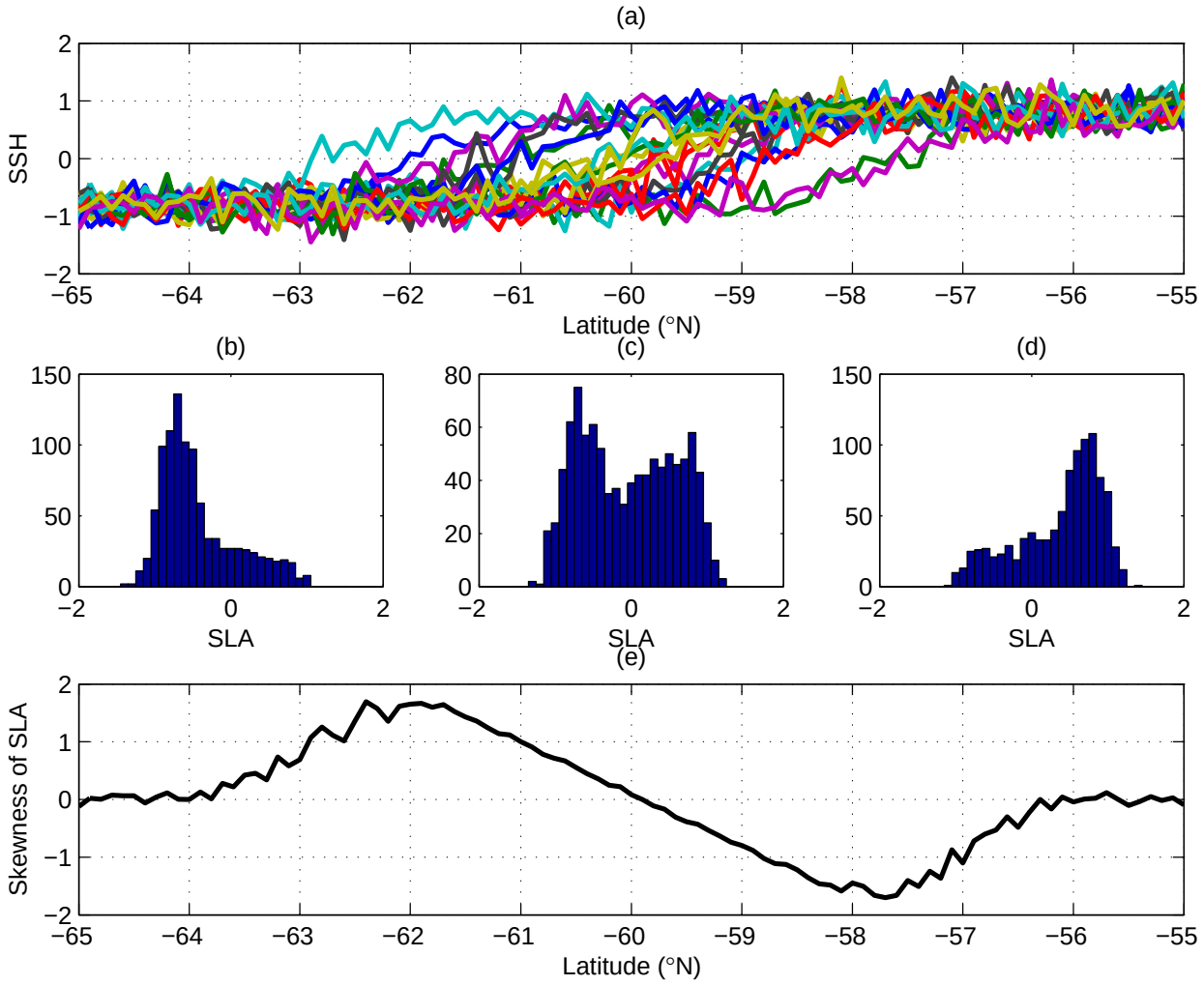

Figure 3.1: Synthetic skewness curves generated using a meandering jet centered at 60°S. Panel (a) shows 10 realizations of SSH using the Monte Carlo method described in Section 3.2, (b), (c), and (d) show the probability density function of sea surface height south of the jet (61°S), at the center of the jet (60°S), and north of the jet (59°S), (e) is the skewness of SLA at each latitude demonstrating the transition from positive to negative skewness as the jet is traversed from south to north.

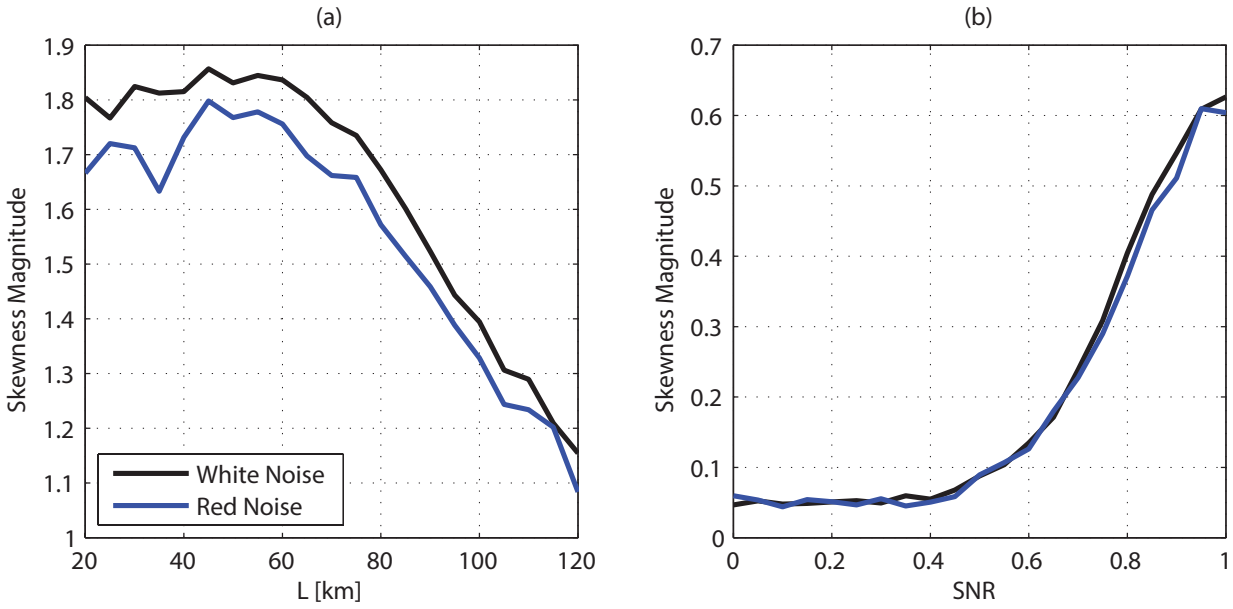

Figure 3.2: The effect of changing the shape parameters of the meandering Gaussian jet model on the magnitude of the resulting skewness using red noise (blue) and white noise (black): (a) L ranges from 20 to 120km (SNR=0.8,$\bar{y}$=0) and (b) SNR ranges from 0 to 1 ($L = 80$km, $\bar{y} = 0$). See Table 1 and text for explanation of parameters

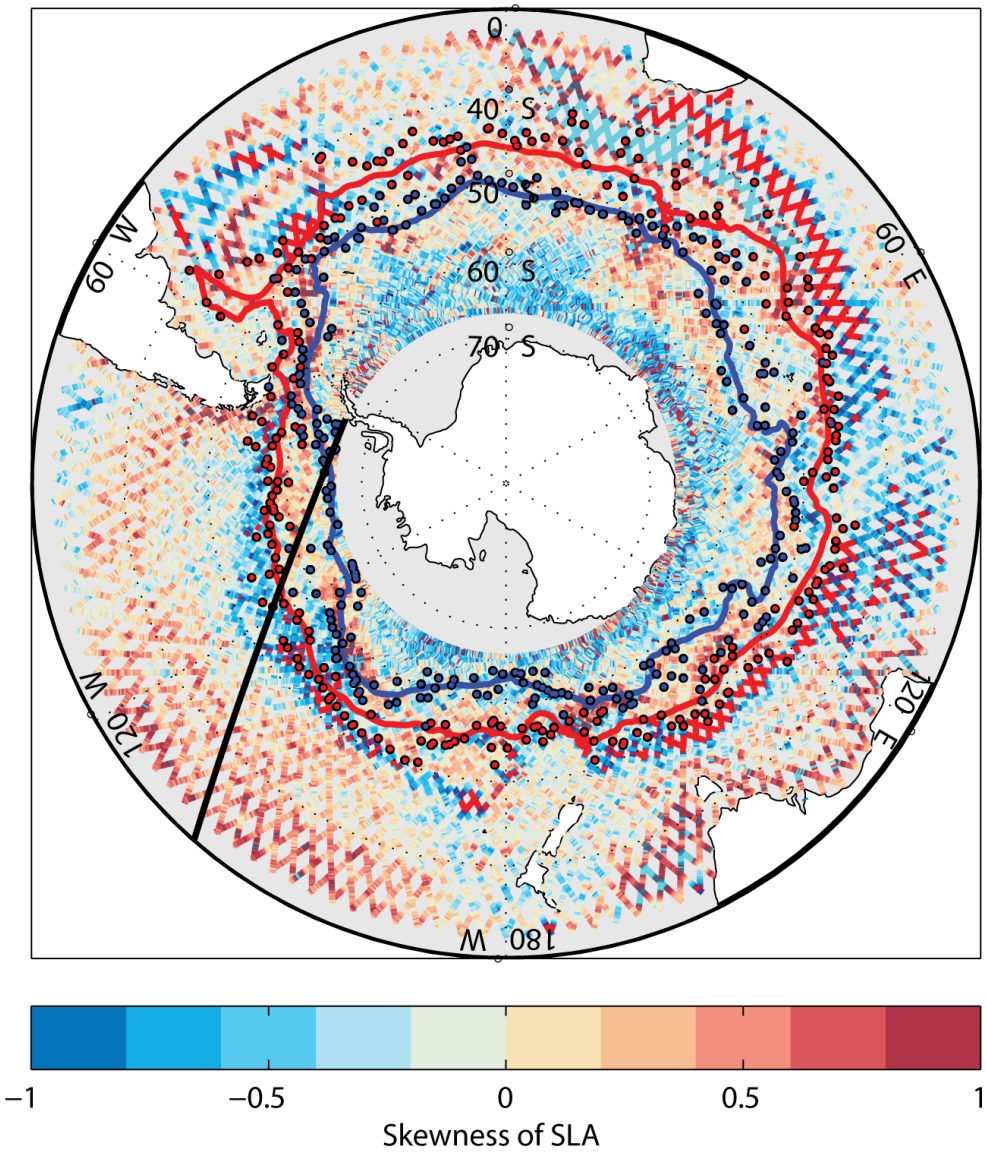

Figure 3.3: Skewness of sea level anomaly (SLA) calculated from along-track satellite altimetry in the Southern Ocean. Red and blue circles represent the mean positions of the Subantarctic Front (SAF) and Polar Front (PF) estimated in this study compared to the middle branches of the SAF and PF from Sokolov and Rintoul (2009). Solid black line denotes the path of ground track 6 shown in Figure 3.4.

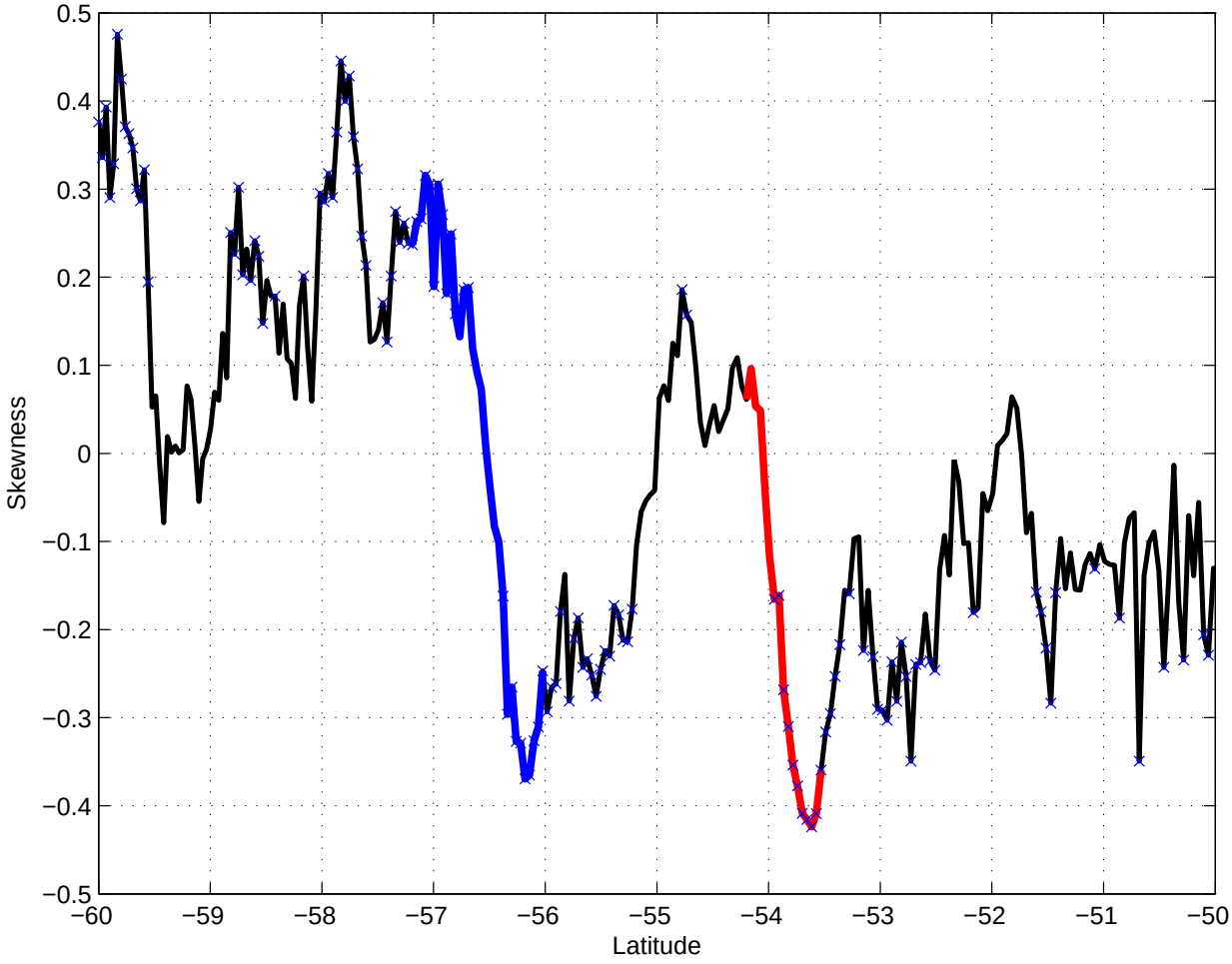

Figure 3.4: Skewness of SLA along ground track 6 showing distinct transitions from positive skewness south of a front to negative skewness north of a front. Blue line represents the transition likely related to the PF, red line represents the SAF, and 'x' represents observations of statistically significant skewness determined from a bootstrap method.

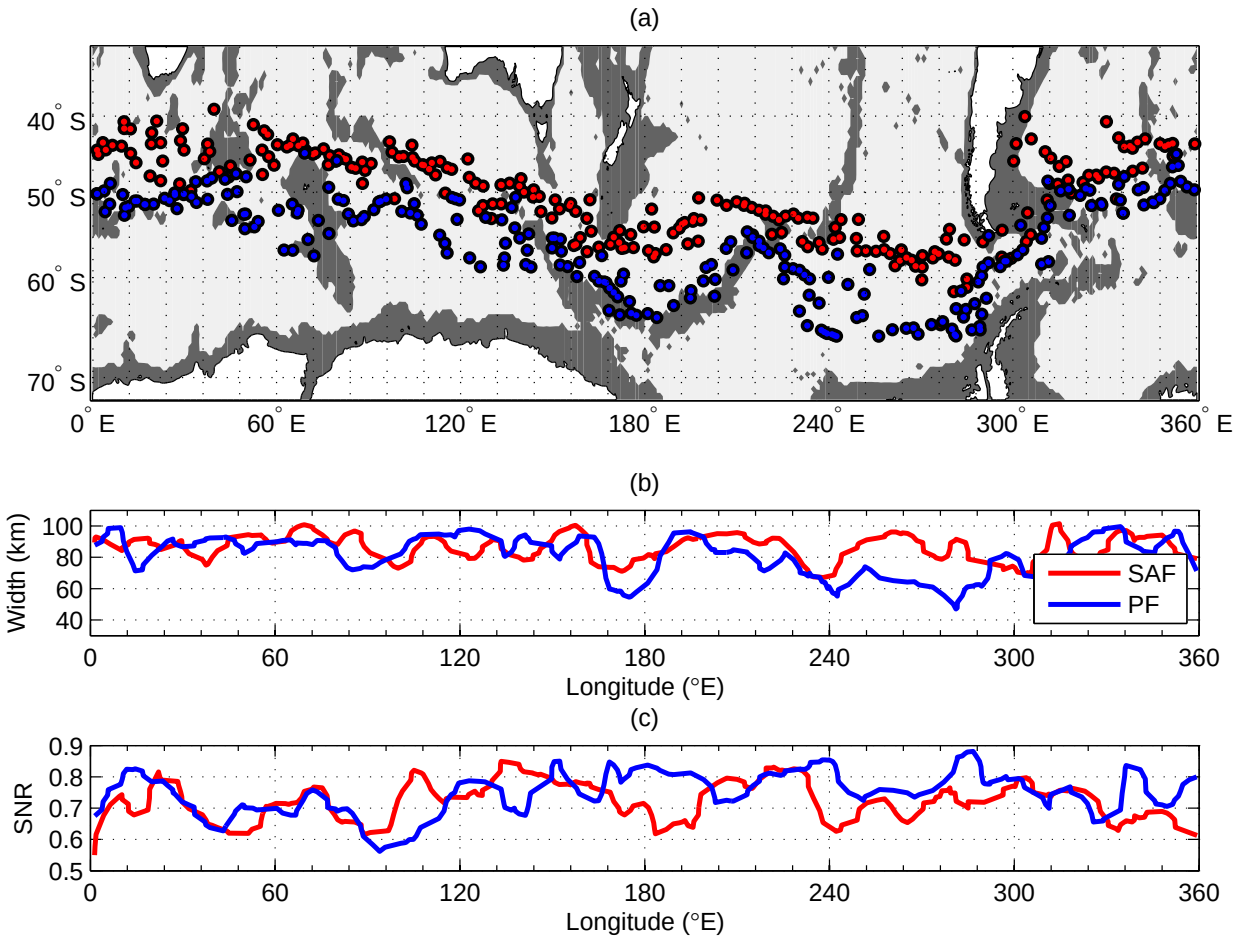

Figure 3.5: (a) Mean position, (b) width, (c) and SNR of the SAF (red line) and PF (blue line) from the entire altimetry record. Colored dots in panel (a) are the same shown in Figure 3.3. Topography shallower than 2000m (Smith, 1997) is denoted by the gray shaded region.

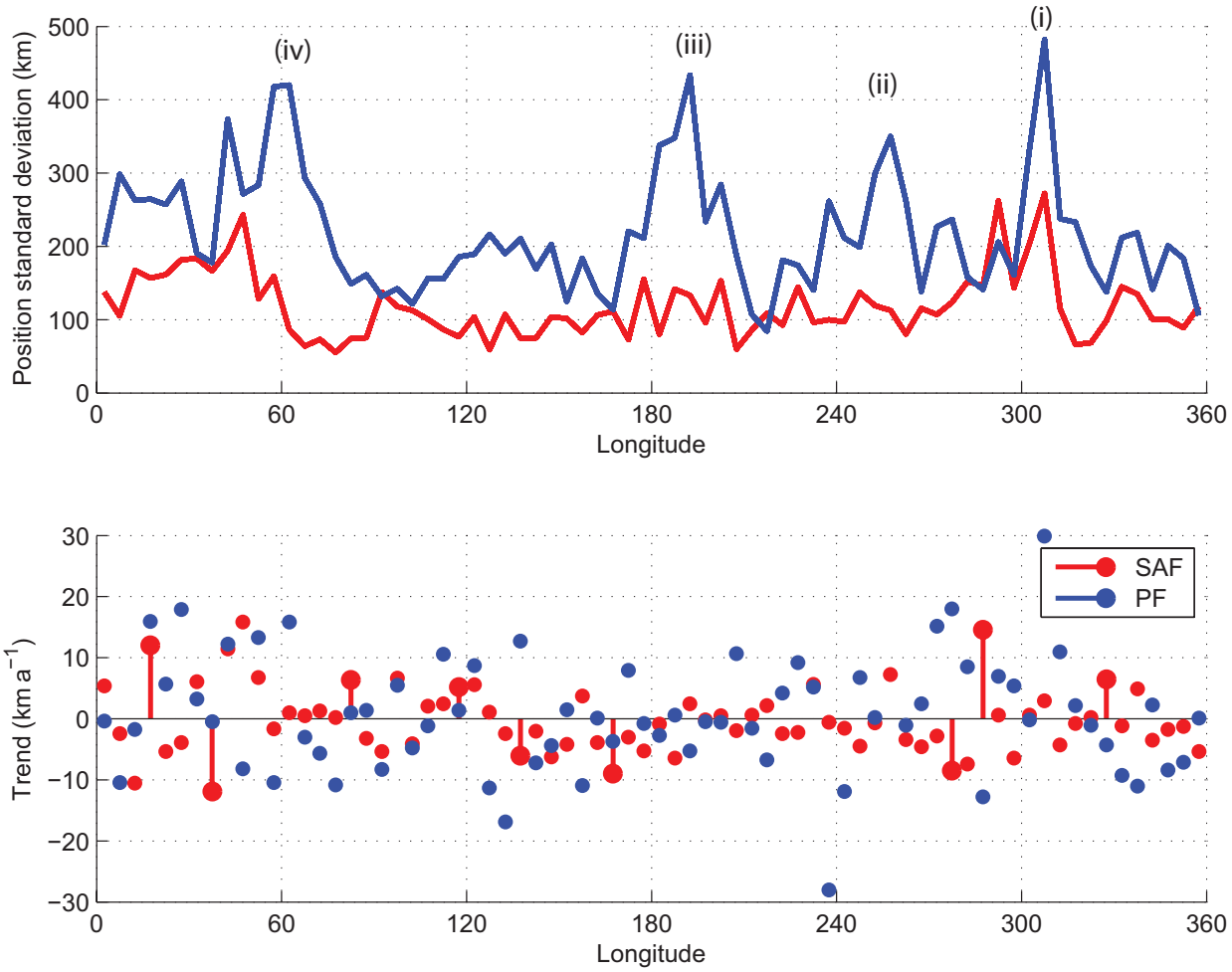

Figure 3.6: Long-term variability in the annual mean latitudinal position over 20 years within 5 degree longitudinal sectors of the SAF (red line) and PF (blue line) from the (a) standard deviation of position and (b) meridional trends (km a^{-1}). Statistically significant trends in (b) are denoted by stems. Roman numerals in (a) represent peaks in PF variability discussed in Section 3.4.

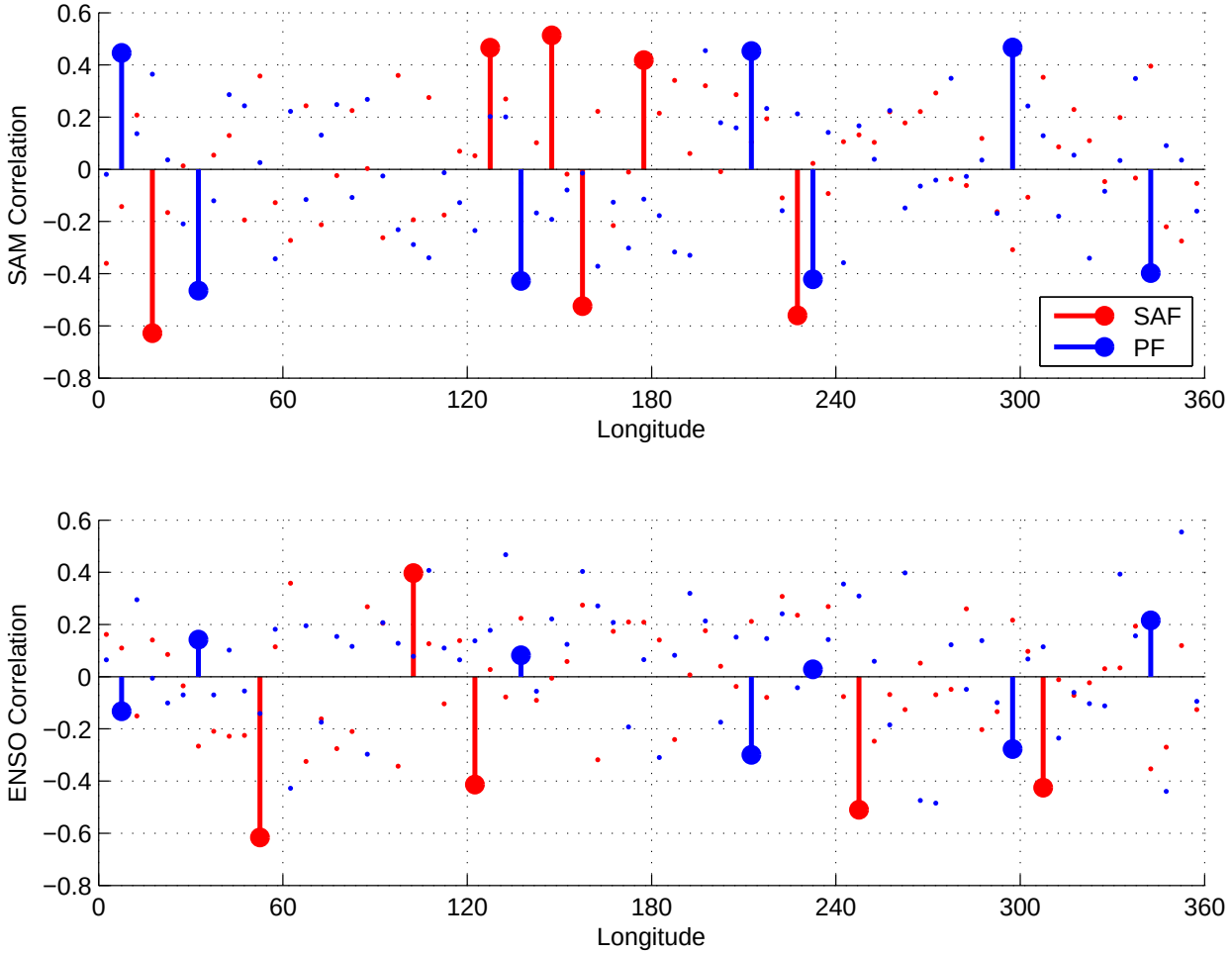

Figure 3.7: Correlations of the SAF (red line) and PF (blue line) with climate modes of variability represented by indices of the Southern Annular Mode (SAM) (a) and the El-niño Southern Oscillation (ENSO) (b). Statistically significant correlations ($p < 0.1$) are denoted by stems.

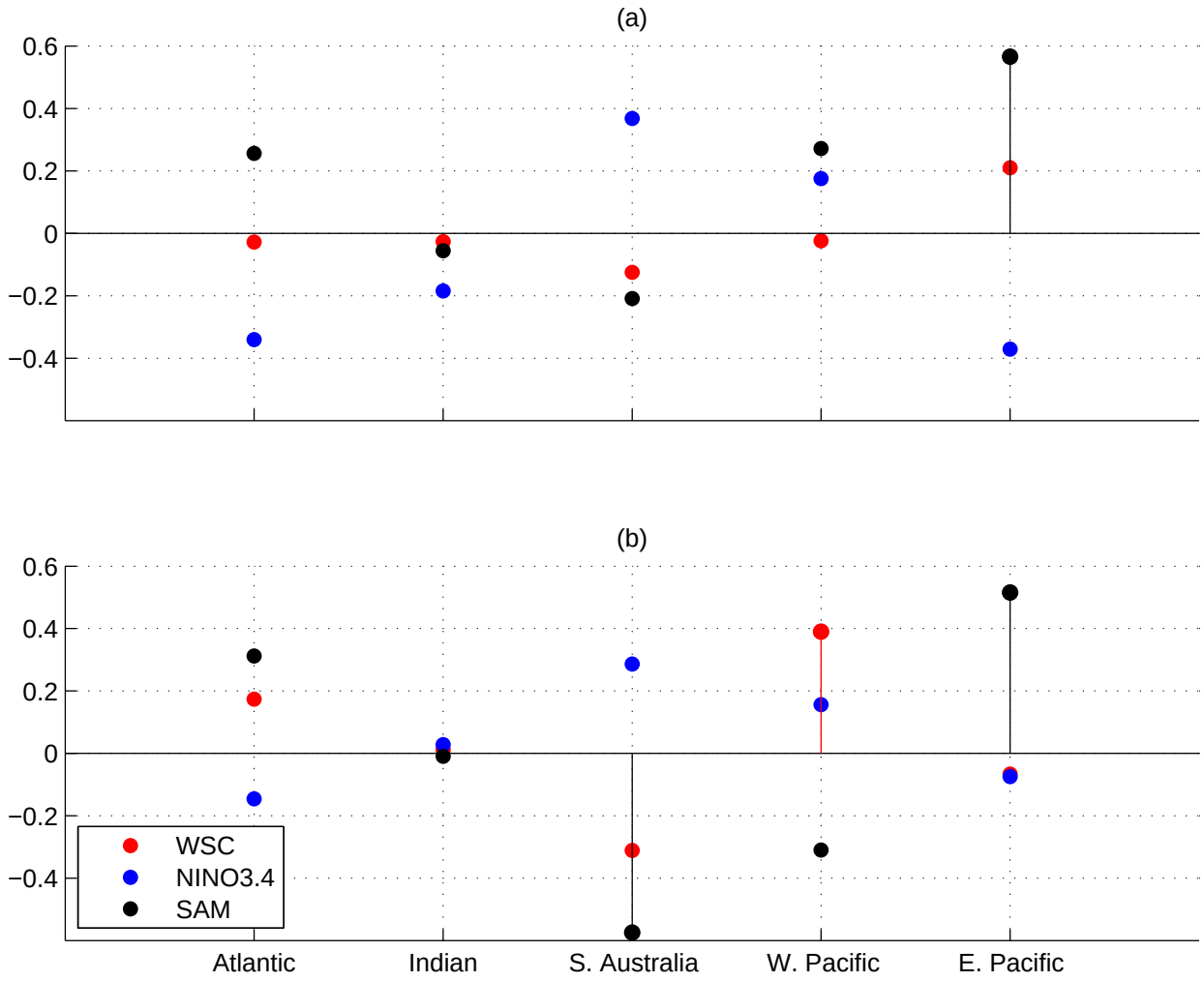

Figure 3.8: Correlations of the latitude of the SAF (a) and PF (b) from the annual subsets averaged over each basin to the SAM and the ENSO (b). Statistically significant correlations of the wind stress curl ($p < 0.1$) and SAM ($p < 0.05$) are denoted by stems.

Chapter 4

EXAMINING THE USE OF TRACER-BASED METHODS IN DETERMINING THE MEAN STATE AND VARIABILITY OF OCEANIC VENTILATION

Abstract

An offline tracer transport model transport is used to simulate chlorofluorocarbon (CFCs), sulfur hexafluoride (SF_6), oxygen, ideal age, and model transit time distributions (TTDs) to evaluate how well tracers can be used to constrain both the mean state and variability of oceanic ventilation. Using climatological transports, the two-parameter 1d inverse Gaussian approximation of the model TTD is found to be an adequate representation of ventilation pathways within the subtropical gyres, but a poor approximation for regions with large gradients in ideal age (i.e. near the base of the thermocline and the continental boundaries). TTDs inferred from CFC-12 and SF_6 using a Peclet number based lookup table approach yield poor representations of the model TTD with a consistent bias towards ventilation being strongly dominated by along-isopycnal diffusion. In a run with variable circulation, ideal age is used to track changes in thermocline ventilation. Variability in both apparent oxygen utilization (AOU) and tracer-inferred TTD mean ages inferred using CFC-12 (assuming fixed Peclet number) and dual tracers (SF_6 and CFC-12) are well-correlated to ideal age variability in most of the thermocline. Changes in AOU are correlated with ideal age variability in even more regions compared to the TTD ages both horizontally and vertically down to intermediate depths. Generally when changes in TTD mean age and AOU agreed in sign, correlations of both with ideal age changes were positive indicating the usefulness of tracers in diagnosing ventilation changes.

4.1 Introduction

The concept of age can be used to describe a variety of metrics relating to the exchange of waters between dynamical regions (Bolin and Rodhe, 1973). In the case of oceanic ventilation, age refers to the time elapsed since a water parcel was last in contact with the atmosphere (Thiele and Sarmiento, 1990). Early studies have taken advantage of the input of tritium into the atmosphere and oceanic mixed layer from nuclear testing and the radioactive decay of tritium into its daughter compounds to estimate ventilation timescales (e.g. Rooth and Östlund (1972); Sarmiento (1983) and Jenkins (1987)). In the 1930s, industrial and military development led to extensive production of chlorofluorocarbons (CFCs), particularly CFC-12 and CFC-11, and their release into the atmosphere. As these compounds have no significant sources or sinks in the oceanic interior and their atmospheric histories are well known (Weiss et al., 1985; Walker et al., 2000), they provide another useful tracer of oceanic ventilation and age. The first robust oceanic measurements of CFC-11 and CFC-12 were reported at roughly the same time as the bomb-tritium studies (Gammon et al., 1982; Bullister and Weiss, 1983). While Weiss et al. (1985) used the ratio of CFC-11 to CFC-12 to estimate a ventilation age, Warner et al. (1996) calculated an age directly by comparing the partial pressure of CFC-11 (pCFC-11) to its atmospheric history. This so-called 'apparent age' method has also been applied to other anthropogenic gases such as CFC-12 and sulfur hexafluoride (SF_6).

Both the tritium and the apparent age methods as used in the above studies neglect the effect of mixing, essentially assuming that transport is advective, and thus give estimates of ventilation age which are biased young (Warner et al., 1996; Mecking, 2004; Mecking et al., 2006; Sonnerup et al., 2007; Waugh, 2003). Later studies introduced the concept of a water parcel's transit time distribution recognizing that a myriad of transport pathways exists from the surface to the interior each with its own transport timescale (Hall and Plumb, 1994; Holzer and Hall, 2000; Haine and Hall, 2002). These studies introduced transit time distribtuions (TTD) as the Green's function solution to the scalar tracer transport equation.

In a 3d sense, TTDs reflect the combination of subduction of water from the surface mixed layer to the interior and the transport of water horizontally due to the large-scale circulation.

While analytic solutions to oceanic transport remain untenable due to the presence of complex geometries and oceanic dynamics (Holzer and Hall, 2000), the solution to the 1d advective-diffusive transport equation takes the form of an inverse Gaussian (IG), a family of distributions defined by two parameters: Γ representing the mean age of the distribution and Δ related to the variance of the distribution (Hall and Plumb, 1994; Holzer and Hall, 2000; Waugh, 2002a). Progress has been made using dual tracers (CFCs and SF_6) to determine these two parameters by assuming that the ventilation of the thermocline via subduction and horizontal transport can be reasonably approximated as an along-isopycnal process (e.g. Bullister et al. (2006); Sonnerup et al. (2008, 2013); Tanhua et al. (2008); Waugh (2002a)).

However, a number of studies have also identified deficiencies that exist when using transient tracers and the 1d TTD method to represent transport pathways in the ocean. Part of this is due to the reduction in atmospheric growth rates of CFCs which have decreased since 1990, yielding a bias towards older apparent ages ventilated since then (Mecking et al., 2006) and has implications for the efficacy of the TTD method as well (e.g. Shao et al. (2013)). Additionally, only oceanic waters which have one formation pathway are likely to match the 1d transport assumption. By comparing IG approximations of 3d TTDs calculated in general circulation models, Peacock and Maltrud (2006) and Trossman (2011) found that TTDs for water masses with multiple formation regions often had multimodal distributions and could not be sufficiently described by a single IG. Peacock and Maltrud (2006) also found unimodal model TTDs elsewhere in the ocean that had wider tails (i.e. slowly decaying tails which are evidence for the influence of older water on the TTD) than could be modeled by an IG. Other studies, recognizing this deficiency, have attempted to use mixture distributions comprised of two IGs to represent the TTD (Waugh, 2002a; Trossman, 2011; Stöven and Tanhua, 2014). However, combining IGs increases the number of free parameters which

would require additional tracers to constrain.

The main goal of this study is to evaluate how well changes in mean age (Γ) of TTDs inferred from CFCs and SF_6 can be used to diagnose changes in oceanic ventilation. To evaluate the skill of applying tracer methods to diagnose variability, we use a global configuration of the Hallberg Isopycnal Model (HIM) as a proxy for the real ocean and simulate the model TTD, CFCs, SF_6, ideal age, and oxygen offline. The focus of the model analysis is in the subtropical Indian-Pacific Oceans where a variety of observational studies using CFCs and SF_6 have been conducted (Tanhua et al., 2013; Sonnerup et al., 2013, 2015).

In Section 4.2, we describe our configuration of HIM and its offline transport model Offtrac, compare the modeled CFC-12 distribution to observations, and introduce the methods by which we calculate the best 1d approximation to the 3d model TTDs. The main results of this study are presented in Section 4.3 which is split into three parts: Section 4.3.1 discusses regions where climatological oceanic transport can be approximated as 1d advection/diffusion, Section 4.3.2 examines how well 1d TTDs constrained by CFC-12 and SF_6 represent the TTD, and Section 4.3.3 compares ideal age variability from a run with variable circulation to the variability in apparent oxygen utilization (AOU), single-tracer, and dual-tracer constrained mean ages to evaluate the skill of these tracer-based approaches in diagnosing changes in ventilation. Section 4.4 discusses the implications of these results and makes recommendations for observational studies that use tracers to diagnose changes in oceanic ventilation. Section 4.5 summarizes the major findings of this study.

4.2 Methods

4.2.1 Model description

Here we describe a two-tiered modeling approach used to simulate both the climatological and interannually varying fields of CFC-11, CFC-12, SF_6, oxygen, and ideal age, and the model TTD. The offline modeling of these tracers allows us to perform long integrations (up

to 4000 years) to achieve a pseudo-steady state for the age tracers. All tracer fields are saved every 5 days except the TTD tracer which is saved monthly from 100 to 4000 years.

We first integrate the physical model HIM (Hallberg, 1995; Hallberg and Gnanadesikan, 2006), an isopycnal coordinate general circulation model, in a coupled ocean sea-ice configuration to obtain temperature, salinity, 3d mass transports, and isopycnal thicknesses. The horizontal resolution is nominally 1° and finer near the equator. The surface boundary layer is represented by a Kraus-Turner bulk mixed layer (Kraus and Turner, 1967) consisting of two layers, homogeneous in tracer, but not in velocity. Two variable density buffer layers are used to simulate entrainment and detrainment from the mixed layer into the oceanic interior which is made up of 45 isopycnal layers referenced to 2000 dbar (σ_2). Along-isopycnal transport by the effect of eddies is parameterized as diffusion of isopycnal thickness (Gent and Mcwilliams, 1990). Minimum background diapycnal diffusivity is set to 10^{-5} m^2 s^{-1} with enhancement due to shear-driven mixing according to Hallberg (2000).

The model is forced by the Common Ocean-ice Reference Experiments version 2 (COREv2) normal year dataset (Large and Yeager, 2008) looped for 430 years which is sufficient for most of the thermocline to come to steady-state. The COREv2 interannually-varying dataset is then used to force the model and looped twice (another 124 years) from 1948-2009, our so-called hindcast fields, storing instantaneous isopycnal thickness and averaged 3d mass transports, temperature, and salinity every five days. Climatological fields are created by averaging over the period 1980-1989 near the middle of the hindcast (comparing ideal age runs with a climatology made in 1960-1969 yielded negligible differences). These physical fields are then used to drive an offline tracer transport model (Offtrac), adapted from the HIM scalar transport code, which has been used previously to examine mixed layer saturations of CFCs (Shao et al., 2013), mercury distribution in the ocean (Zhang et al., 2014), and variability in North Pacific oxygen (Deutsch, 2005).

4.2.2 Implementation of tracers

CFCs and SF_6 are modeled using the same methodology described in Shao et al. (2013) that is based on the protocols laid out by the Ocean Carbon Model Intercomparison Project version 2 (OCMIP-2) (Najjar and Orr, 1998). Atmospheric mixing ratios of CFC-11, CFC-12, and SF_6 (Walker et al., 2000) (`http://cdiac.ornl.gov/oceans/new_atmCFC.html`) are used in conjunction with their solubilities (Warner and Weiss (1985) for CFC-11 and CFC-12 and Bullister et al. (2002) for SF_6 to determine the surface concentrations of each tracer. To maintain consistency in the boundary condition of CFCs and SF_6 between the climatological and hindcast simulations, we assume that the atmospheric concentrations were zero until 1948. The truncation of the atmospheric histories results in a neglible ($< 0.1\%$) change in tracer inventories because between 1936-1948, the atmospheric mixing ratios are so small (< 5 ppt for CFC-12 compared to a maximum value of about 550ppt).

The OCMIP2 protocol is also used to model oxygen (see Deutsch et al. (2006) for the specific implementation in Offtac). Oxygen production and consumption terms are determined by applying Redfield ratios (Redfield, 1934; Anderson and Sarmiento, 1994) to phosphate sources and sinks that are calculated using a simplified phosphate cycling model (Najjar and Orr, 1998). Two different simulations for oxygen and CFCs are performed: 1) where the surface is set to saturation for each of the gases and 2) simulating gas exchange following the OCMIP protocol, to allow for disequilibria between the atmosphere and ocean (Shao et al., 2013).

Ideal age is modeled as a tracer initialized to 0 and stepped forward with a source function equal to the length of the timestep everywhere except in the mixed layer where the tracer is kept at zero (Thiele and Sarmiento, 1990). Both oxygen and ideal age are brought to pseudo steady state by integrating Offtrac for 2000 years using climatological transports. The abyssal ocean is not quite in steady state even after 2000 years though this does not have a significant effect on the thermocline. After the spinup period, all the fields are then looped twice over

the hindcast period (1948-2009) to eliminate the initial transient response of transitioning from climatological to interannually varying circulation. The tracer concentrations from the second loop are used to evaluate the ability of tracers to quantify interannual variability.

The model TTD is computed using the boundary impulse response (BIR) method (Peacock and Maltrud, 2006; Haine et al., 2008; Maltrud et al., 2009) where a passive tracer is set to 1 in the surface mixed layer for the first year of integration and to 0 from then on with no interior sink of tracer. Offtrac is stepped forward using the 5-day climatological circulation for 4000 years. The BIR tracer is saved at each model grid point every 25 days for the first 100 years to enhance the resolution of the TTDs in waters that are rapidly ventilated. From 101 to 4000 years, the annual average of the tracer at every grid point is saved. From model year 101 to 4000, annual averages are saved. The true 3d model TTDs calculated using the BIR method are referred to hereinafter as TTD-BIR.

4.2.3 Model-data comparison

The skill of Offtrac and HIM in representing thermocline ventilation and tracers is evaluated by comparing salinity and pCFC-12 (calculated by dividing the modeled CFC-12 concentrations by temperature and salinity dependent solubility (Warner and Weiss, 1985)) along zonal transects in the South Indian, North Pacific, and South Pacific Oceans. Model output is projected onto depth by calculating the depth of the center of each isopycnal. To emulate the effective 'smoothing' of the model output due to discrete differences in isopycnal density, the observational data along each section are objectively mapped from bottle data onto σ_2 coordinates with a correlation length scale of 0.1 kg m^{-3} vertically and 2° horizontally and then projected onto depth.

Intermediate waters are characterized in the thermocline as subsurface minima in salinity as a result of their formation in the relatively fresh, but cold subpolar portions of the basins. North Pacific Intermediate Water (NPIW) is formed in the Sea of Okhotsk before being

modified in the region between the Oyashio and Kuroshio Extension (Talley, 1993; Yasuda, 1997). In the Southern Ocean, Antarctic Intermediate Water (AAIW) is formed both by outcropping Subantarctic Mode Waters that are modified by air-sea fluxes and also by the transformation of Antarctic Surface Water as it crosses the Polar Front and subducts at the Subantarctic Front (Sloyan and Rintoul, 2001).

In the model, the depth of NPIW matches the observations well (labeled white contour in Figures 4.1 a, b), but AAIW is shallower than observed by about 200m (Figures 4.1 c, d, e, and f). AAIW is also fresher than observed by roughly 0.2‰ in the Pacific and 0.3‰ in the Indian Ocean. This is likely attributable to the surface salinity restoration in the model which may preferentially add freshwater in regions of intermediate water formation. NPIW has the correct salinity but is also slightly too thick likely because the Oyashio and Kuroshio Extension are not fully separated in the model. These deficiencies in intermediate water representation are common in low-resolution ocean models because parameterizations of eddy processes fail to capture the localized mixing in the formation regions (Ladd and Thompson, 2001).

CFC-12 partial pressures (pCFC-12) can also be used as a metric for evaluating the model's skill (e.g. England et al. (1994) and Valsala et al. (2008)) at representing oceanic ventilation as they can only be measured in waters which have been actively ventilated. In the North Pacific and South Indian Oceans, pCFC-12 is higher than observed indicating a bias towards a younger thermocline (Figures 4.1 a and b). In contrast, concentrations in the western portion of the South Pacific basin are too low indicating a bias towards slower ventilation (Figure 4.1c and d). Despite these deficiencies, the broad agreement between the model and observations within the subtropical gyres suggests the model represents oceanic ventilation reasonably well.

4.2.4 1d approximations of the model TTD

To estimate how well transient tracers constrain the 3d model TTD (TTD-BIR), we discuss the functional form of the 1d IG TTD, how we choose to estimate the parameters of the 1d TTD from the true TTD-BIR, and how 1d TTDs can be inferred from CFC-12 and SF_6.

The inverse Gaussian distribution and estimation from the model

Holzer and Hall (2000) showed that the Green's function solution to the 1d transport equation

$$\partial_t \phi(x,t) + u\partial_x \phi(x,t) = \kappa \partial_x^2 \phi(x,t) \tag{4.1}$$

where u is the advective velocity and κ is along-isopycnal tracer diffusivity, is

$$\phi(t,\Gamma,\Delta) = \left[\Gamma^3/\left(4\pi\Delta^2 t^3\right)\right]^{1/2} \exp\left[-\Gamma(t-\Gamma)^2/4\Delta^2 t\right] \tag{4.2}$$

with $\Gamma = x/u$ and $\Delta = 2\kappa x/u^3$. The Peclet (Pe) number for the flow, which characterizes the flow as being dominated by either advective ($Pe > 1$) or diffusive ($Pe < 1$) processes, can be represented as Γ^2/Δ^2 (Holzer and Hall, 2000; Waugh, 2003). In the oceanographic literature, Δ/Γ (i.e. $1/\sqrt{Pe}$) is often used instead of Pe.

This solution has a similar functional form to the probability density function (PDF) of IG distributions with shape parameters Γ and λ

$$IG(t,\Gamma,\lambda) = \left(\lambda/2\pi t^3\right)^{1/2} exp\left[-\lambda(t-\Gamma)^2/(2t\Gamma^2)\right]. \tag{4.3}$$

With a change of variables $\Delta = \sqrt{\Gamma^3/2\lambda}$, (4.2) and (4.3) are identical. The IG distribution is entirely defined by the two shape parameters Γ and λ (and thus also by Γ and Δ).

Determining the parameters of a distribution from a set of data is a widely studied statistical problem. Two commonly used methods to estimate parameters are the 'method

of moments' and maximum likelihood estimators (MLE) (Seshadri, 1999). The method of moments relies on analytically derived relationships between model parameters and the moments of a distribution defined as

$$\gamma_n = \int_0^\infty \mathcal{G}(t) t^n \, dt \tag{4.4}$$

where γ_n is the nth moment of the distribution $\mathcal{G}$. For an IG of the form described in (4.2), $\Gamma = \gamma_1$ and $\Delta = 1/2\gamma_2$ (Waugh, 2003). Peacock and Maltrud (2006) used the method of moments calculated from the TTD-BIR to calculate Γ and Δ. However in this study, we find that the second moment is slow to converge in the case of the model TTDs whose tails drop off more slowly than t^{-2} and may lead to biased estimates of the shape parameters (Seshadri, 1999).

To overcome this potential bias, we calculate IG parameters using the MLEs which maximizes the agreement between an empirical PDF (here the TTD-BIR) and an assumed form of the PDF (here an IG). For an IG of the form in (4.3), the MLE estimates of the shape parameters (which can be found in Seshadri (1999)) are given by

$$\Gamma = \int_0^{t_f} \mathcal{G}(t) t \, dt \tag{4.5}$$

and

$$1/\lambda = \int_0^{t_f} \mathcal{G}(t)(1/t - 1/\Gamma) dt \tag{4.6}$$

where t_f is length of the integration (here 4000 years). Note that by this definition Γ is the same for both the TTD-BIR and IG-MLE. When calculating these parameters using the TTD-BIR for $\mathcal{G}$, we first normalize the TTD to ensure that $\int_0^{t_f} \mathcal{G} dt = 1$. TTDs which have the functional form of an IG whose parameters are based on these MLEs are referred to in this paper as IG-MLE.

4.2.5 Evaluating the goodness of fit

Modeling studies which have calculated the model TTD using the BIR method have shown that in many regions of the ocean, TTDs have relatively simple shapes that are qualitatively similar to an inverse Gaussian (Peacock and Maltrud, 2006; Maltrud et al., 2009). To test how well oceanic transport could be approximated by a 1d model, Peacock and Maltrud (2006) convolved IGs whose parameters were estimated from the model TTD using the method of moments (Seshadri, 1999) with the boundary conditions for CFC-like and radiocarbon-like tracers. The largest differences between the directly modeled tracer fields and those from the convolutions with the IG were in the Southern Ocean where recently ventilated waters mixed with older waters leading to well-defined peaks around the mode of the distribution along with a slowly decaying tail. Large biases were also found in the Southern Ocean where model TTDs are multimodal due to multiple ventilation pathways. They found that the differences were sensitive to the tracer used; a radiocarbon-like tracer was more sensitive for old waters and when $\Delta/\Gamma > 1$, whereas a CFC-like tracer had larger differences for young waters. Here, we introduce a metric based on the interpretation of TTDs as a statistical distribution which can be used consistently without dependence on the age or nature of the flow.

If the ages in a TTD were normally distributed, a standard z-test could be used to determine whether the 1d TTD matched the true TTD-BIR. However, neither the TTD-BIR nor the 1d IG are normal but may be highly skewed distributions. In this study we compare individual TTDs visually, but also use the Cramer von Mises (CvM) as a goodness-of-fit statistic to objectively quantify the similarity between TTDs. The CvM metric is applicable to skewed distributions generally (and IGs specifically) and is defined as

$$\mathrm{CvM}^2 = \int_0^\infty \left(F_1(t) - F_2(t)\right)^2 \; dF_1(t) \tag{4.7}$$

where $F_1(t)$ and $F_2(t)$ are the cumulative probability distribution functions (CDF) of two TTDs, G_1 and G_2, defined as $F_n(t) = \int_0^t \mathcal{G}_n(t')dt'$ (Anderson, 1962). Because the cumulative probability distribution is an integrated quantity of all previous ages up to t, this metric captures differences between two distributions whether they occur systematically throughout the distribution or in the beginning or tail of the distribution.

As a demonstration of how this CvM metric can be used to compare two TTDs, we use it to quantify whether IGs are more sensitive to changes in Γ or Δ. We first define F_1 to be the CDF of an IG with $\Delta = \Gamma = 50$ years. Next, we change only one of the parameters at a time to vary Pe between 0.1 to 5. F_Δ refers to the CDF of an IG where $\Gamma = 50$ yrs and Δ varies. F_Γ sets $\Delta = 50$ yrs and allows Γ to vary. We note that the choice of 50 years is arbitrary as the CvM would be the same if we chose any value for $\Gamma = \Delta$ in F_1 and varied Pe.

Applying the CvM metric (4.7) to F_Δ and F_Γ relative to F_1 shows than changes in the Δ parameter lead to IGs which are more dissimilar that changes in Γ suggesting the overall shape of the distribution is controlled by Δ. The CvM also varies more rapidly for both parameters when the Pe of F_Δ or F_Γ is less than that of F_1. Because of this sensitivity, for applications where Δ/Γ (i.e. $Pe^{-1/2}$) is assumed to be fixed, biases in Γ are likely to be higher if the ventilation pathways are diffusive rather than advective

4.2.6 Inferring the 1d TTD from tracers

We use a lookup table approach (Stanley et al., 2012) modified slightly from Sonnerup et al. (2015) to infer 1d TTDs constrained by modeled pCFC-12 and pSF_6. We omit CFC-11 for computational simplicity as we found that it provided a similar constraint on the TTD as CFC-12, consistent with Sonnerup et al. (2008). IGs with a given Γ and Δ are convolved with the atmospheric history of CFC-12 and SF_6 to calculate a predicted partial pressure for each gas. IGs are calculated for a range of ages from 0.25 years to 1000 years in 0.25

year increments. To calculate Δ, each Γ is multiplied by $1/\sqrt{(Pe)}$ where Pe (Γ^2/Δ^2) ranges from 0.05 to 5 in 0.05 increments. These values for Γ and Pe covers parameter space for Δ/Γ discussed in the literature (0.1 to 7) (Waugh, 2003; Sonnerup et al., 2015). Γ and Δ for a pCFC-12 and pSF_6 pair is then calculated as the average of all the IGs which match the two modeled tracer partial pressures within 2%. Separate tables are made for each hemisphere to account for the slightly higher atmospheric concentrations in the northern hemisphere.

Basing our table on linearly spaced values for Pe instead of Δ/Γ, differs from the approach used by Sonnerup et al. (2013) and Sonnerup et al. (2015), but yields better estimates of Δ and Γ using the CFC-12 and SF_6 tracer pair particularly for $\Delta/\Gamma > 1$. As an example of this, a water parcel whose TTD can be described by an IG with $\Gamma = 15$ and $\Delta = 25$ would have pCFC-12 and pSF_6 values of 317.4ppt and 1.2ppt. Applying the table lookup method described above, the Pe based table gives an estimate of $\Gamma = 16.2$ and $\Delta = 23.9$yrs whereas the Δ/Γ based table yields $\Gamma = 19.8$ yrs and $\Delta = 35.0$ yrs. This bias results from IGs predicting similar values of pCFC-12 and pSF_6 when $\Delta/\Gamma > 1$ (Waugh, 2003). When performing the table lookup, the more diffusive TTDs are then oversampled compared to advective TTDs.

TTDs inferred using CFC-12 and SF_6 partial pressures are referred to in the text as IG-Dual. In Section 4.3.3, TTDs where we assume that $\Delta/\Gamma = 1$ (e.g. Waugh (2003)) are inferred using only pCFC-12 (referred to as IG-CFC12).

4.3 Results

In section 4.3.1, the IG-MLE is compared to the TTD-BIR in the North Pacific and the Southern Indo-Pacific basins to investigate where in the thermocline transport can be approximated as 1d. In Section 4.3.2, 1d TTDs are then inferred using modeled CFC-12 and SF_6 (referred to as IG-Dual) and compared to the IG-MLE to determine where transient tracers can provide information about the transport pathways. In Section 4.3.3, the skill of

Γ from IG-Dual and AOU in diagnosing changes in oceanic ventilation is evaluated against ideal age from the hindcast simulation over the time period from 1970-2010.

4.3.1 1d approximations of the climatological TTD

In this section, the IG-MLE is used to show both the horizontal, along-isopycnal and the vertical structures of Γ, Δ/Γ, and CvM in the North Pacific and South Indian Oceans.

North Pacific

We compare the TTD-BIR to the IG-MLE and IG-Dual to investigate how well the ventilation of the thermocline can be represented by one-dimensional transport. The analysis first focuses on how closely the IG-MLE matches the TTD-BIR on the $\sigma_2 = 34.1$ kg m^{-3} isopycnal (model layer 15) in the North Pacific, corresponding to the mode water density, along a zonal transect at 30°N, and on the $\sigma_2 = 35.6$ kg m^{-3} isopycnal (model layer 26) in the southern hemisphere on zonal transects along 32°S which represents the denser variety of Antarctic Intermediate Water (AAIW).

Mode waters in the North Pacific are primarily formed via the permanent subduction of water from the deep wintertime mixed layer into the thermocline (Bingham, 1992). These waters have a local minimum in potential vorticity minimum and represent some of the youngest waters in the thermocline. While observations show a distinction between various classes of mode water (Bingham, 1992; Nakamura, 1996; Suga et al., 1997), the model tends to produce one primary type of mode water distributed across model layers 15 and 16 ($\sigma_2 =$ 34.10 to 34.35 kg m^{-3}) referred to hereinafter as North Pacific Mode Water (NPMW).

The spatial structure of age on the $\sigma_2 = 34.1$ kg m^{-3} isopycnal reflects the along-stream distance from the outcrop location (Figure 4.3a). The youngest waters are found near 40°N, 190°E which is the primary formation region of NPMW in the model and is co-located with wintertime mixed layer depths of more than 150m. This water mass ages as it is transported

westward around the outer boundary of the gyre. West of 170°E the pool of water older than 20 years reflects recirculating water near the Kuroshio. South of 20°N the age increases rapidly from about 10 years to over 100 years likely owing to the influence of old water upwelled near the equator.

The dominance of advective versus diffusive transport on the isopycnal is related to the water parcel's proximity to the center of the gyre (Figure 4.3b). Outside the outcrop region, Δ/Γ from the IG-MLE is less than one indicating predominantly advective transport associated with the large-scale gyre circulation. Within the isopycnal outcrop region, the large diapycnal mixing associated with the seasonal entrainment/detrainment of the isopycnal leads to the highest values of Δ/Γ. The coastal waters in the eastern basin and tropical waters also have $\Delta/\Gamma > 1$ owing to wind-driven upwelling associated with strong diapycnal transport.

The IG-MLE is a good approximation to the TTD-BIR throughout must of the subtropical gyre (CvM$<$ 0.1 in Figure 4.3c), though the seasonality of the TTD-BIR that reflects the wintertime ventilation of this isopycnal cannot represented by an IG. Within the seasonal outcrop (location (ii) in Figure , the IG does not capture the obduction of water back into the mixed layer that occurs when the wintertime mixed layer densities within the seasonal outcrop are denser than the mode water leading to a TTD-BIR with a very strong seasonal cycle (Figure 4.4a). The TTD-BIR within the mode water (Figure 4.4b, location (ii) also exhibits a seasonal cycle but much smaller than that of (Figure 4.4a) indicating that the smooth interannual variation described by an IG is a better approximation for TTD-BIRs further from the outcrop location.

In addition to seasonal variations, the TTD-BIRs can be bimodal reflecting the presence of multiple ventilation pathways. At locations (i) and (ii) shown in Figure 4.3, the distributions are weakly bimodal (Figures 4.4a and 4.4b respectively) with TTD-BIR being characterized by one fast and one slower transport pathway. At point (i), the tracer is immediately

transported from the mixed layer onto the outcropping isopycnal, followed by a second pulse of tracer at about 20 years from waters which likely have transited around the subpolar gyre. Location (ii) has a bimodal distribution for similar reasons: the first peak reflects the portion of the mode water which is formed by subduction, and the second, weaker peak from other formation sites within the gyre. These bimodal distributions have been noted before in the Southern Ocean (e.g Peacock and Maltrud (2006) and Trossman et al. (2014)), but not, to our knowledge, in the North Pacific.

The combination of multiple transport pathways can also yield unimodal distributions that cannot be described by an IG. On the southern boundary of the gyre around 20°N (Figure 4.4c at location iii in Figure 4.3), the distribution has a very broad peak which drops off quickly between 15 and 25 years and then transitions to a slower decay rate after about 30 years. As IGs have tails which smoothly decay, the rapid change in the decay rate is an indicator that the TTD-BIR here would have to be represented by the mixture of an IG with low Γ and an IG with larger Γ (as proposed in a different setting by Waugh (2002a)). Unimodal TTDs with thick, slowly attenuating tails are prevalent in regions with large gradients in ideal age, indicating that on the boundary between the rapidly ventilated thermocline and tropical waters, IGs do not well represent the older portions of the TTD-BIR.

We next examine Δ/Γ and CvM on zonal transects across the subtropical gyre along 30°N (Figure 4.5a). Generally, the IG-MLE serves as a good approximation to the TTD-BIR (CvM<0.1) throughout most of the ventilated thermocline with the exception of three regions (marked by a yellow contour in Figure 4.5a): 1) below the base of NPMW (dashed contour in Figure 4.5a) and above the NPIW (solid black contour) in the eastern basin from 200°E to 240°E, 2) around 500m of depth between 130°E and 175°E, and 3) between 100 and 300m of depth from 150°E to 170°E. Direct inspection of TTD-BIRs within these regions shows that in regions 1 and 2, the distributions have sharp, narrow advective peaks

transitioning to very broad shoulders, indicating multiple transport pathways. Region 3 exhibits TTDs similar to those shown in Figure 4.4a, suggesting that the isopycnals in this region are being reentrained into the mixed layer likely by meridional movement of the Kuroshio.

Whereas ventilations pathways may be expected to become diffusively dominated deeper in the water column due to weakening horizontal circulation, the vertical structure of Δ/Γ estimated from the IG-MLE shows a more complicated structure. Above the NPIW (solid black contour Figure 4.5a), transport pathways are dominated by advective transport presumably due to the relatively simple, rapid dynamics of gyre circulation. Just below these waters, in the transition region between the abyssal ocean and ventilated thermocline (below the deeper black contour), the transport pathways become more diffusive. Below 800m, in the abyssal North Pacific, advection dominates. This counterintuitive result arises because the Pe number for this flow assumes that both u and κ are constant along the entirety of water parcel's path from the surface to the interior. Older water parcels violate this assumption as Γ and Δ are affected by variations in u, whereas for young oceanic waters the flow might be reasonably assumed to be approximately local.

South Indo-Pacific

We next examine the properties of the TTD-BIR and IG-MLE on an isopycnal ($\sigma_2 = 35.6$ kg m^{-3}) that lies within the salinity minimum characterizing AAIW. In the Indian Ocean, the isopycnal forms the core of the AAIW and in the South Pacific basin it forms the upper boundary of the AAIW.

The model AAIW isopycnal ages rapidly away from the outcrop region to around 100 years as it moves below the Antarctic Circumpolar Current (ACC) and across the northern boundary of the ACC (roughly 40°S to 45°S) into the ventilated subtropical gyres (around 30°S in Figure 4.6a). In contrast to the NPMW where the age varied by longitude, the

progression from younger to older water is nearly zonally symmetric following the equatorward transport of AAIW. Waters near the eastern boundaries on each continent disrupt this symmetry around 30°S owing to the influence of coastal upwelling.

The TTDs also show that advective transport dominates (i.e. low Δ/Γ) further from the outcrop region (Figure 4.6b). The more diffusive pathways lie within 10° of the seasonal outcrop region presumably due to the modification of AAIW precursors and strong mixing associated with the ACC. Within the subtropical gyres, the TTDs indicate that diffusive and advective transports become comparable (similar to that seen in the North Pacific) though Δ/Γ is generally larger than 1, presumably reflecting the more complicated formation and transformation of AAIW.

The ventilation of waters across most of the isopycnal is well-characterized by the IG-MLE despite the fact that AAIW is known to have multiple formation regions (e.g Taft (1963) and Talley (1996)) which migh suggest that TTDs in these waters should be multimodal. However, we find that most of the TTD-BIRs in this isopycnal are unimodal though with high Δ/Γ ratios. We speculate that this may be due to the strong mixing and rapid transport of the ACC homogenizing the distinct formation pathways of the AAIW.

At locations (iv) and (v) in Figure 4.6 is near the northernmost extent of the salinity minimum that characterizes AAIW. The erosion of AAIW as it mixies with saltier, older waters in this region leads to a TTD-BIR that suggests the presence of two ventilation pathways, one fast because of AAIW formation and a slower one representing older waters. The IG, which presumes only one ventilation pathway, is, thus, a poor approximation to the TTD-BIR in this region.

4.3.2 Tracer-inferred TTDs and TTD-BIR

In this section, we examine how well IGs inferred using CFC-12 and SF_6 (IG-Dual) match the IG-MLE (i.e. the best 1d approximation of the TTD-BIR). The analysis focuses in the

North Pacific on the NPMW isopycnal (σ_2 = 34.1 kg m^{-3}, layer 15) and in the Southern Ocean on the AAIW isopycnal (σ_2 = 35.6 kg m^{-3}, layer 23).

In the North Pacific, the IG-Dual differs significantly from the IG-MLE across most of the isopycnal layer (Figure 4.7a). The discrepancy between IG-Dual and IG-MLE is particularly pronounced in the mode water and close to the outcrop location. Comparing the IG-Dual at location (ii) (Figure 4.7a) to the IG-MLE and TTD-BIR shows that they all have similar mean ages (around 4.5 years) but that the TTD-Dual's shape is very different than the IG-MLE and TTD-BIR (Figure 4.7b). The Δ of IG-Dual is almost twice that of IG-MLE (6.7 versus 3.3 years). This bias towards higher Δ persists across the entirety of this isopycnal and is the main reason for the poor fit of the IG-Dual to the IG-MLE.

The bias towards higher Δ/Γ may suggest that for young waters SF_6 does not provide a strong additional constraint on the TTD. Waugh (2003) showed that the portion of the TTD constrained by a tracer is primarily determined by the atmospheric history and growth rates of the gas. Although inclusion of CFC-11 with CFC-12 did not provide a strong additional constraint on the shape of the TTD, SF_6 was demonstrated to add useful time information (Waugh, 2002b; Sonnerup et al., 2008) for some time ranges. However, for these relatively young water parcels, the timescales constrained by CFC-12 and SF_6 are similar and are not strongly independent constraints on the shape of the distribution.

The conversion of concentrations of CFC-12 and SF_6 to partial pressures by dividing by their solubilities may introduce a bias for waters whose temperature and salinity change significantly after subduction. While the permanent and seasonal parts of the thermocline are often thought of as separate, in actuality no definite boundary exists. The seasonal cycle is strongest near the surface, however even in the mode water seasonal variability can cause changes in partial pressure of about 5-10%. Isopycnals near the surface ocean are supersaturated in spring and summer with partial pressures of CFC-12 and SF_6 that exceed the maximum observed atmospheric values (near-surface of Figure 4.3, masked in

white). This results from solubility decreasing as the surface warms which can lead to supersaturation if the waters are detrained from the shoaling mixed layer before coming into equilibrium with the atmosphere.

In the Southern Ocean on the AAIW isopycnal ($\sigma_2 = 35.6$ kg m^{-3}), the IG-Dual differs significantly from the IG-MLE (Figure 4.8a) despite the IG-MLE being a good approximation of the TTD-BIR. The discrepancy between IG-Dual and IG-MLE is due to differences in both Γ and Δ/Γ (not shown). In both gyres, Δ/Γ of IG-Dual is much higher than the IG-MLE by a factor of 2 or more (Figure 4.8b,c). Within the subtropical gyre of the Indian Ocean, Γ-Dual has a bias towards lower Γ of about 25% (e.g. at location (iv) in Figures 4.6 and 4.8), Γ-Dual is 115 yrs whereas Γ-MLE is 156 yrs). In the South Pacific gyre, Γ-Dual has a bias towards higher Γ of about 15% (at location (v) in Figures 4.6 and 4.8, Γ-Dual is 179 yrs and Γ-MLE is 154 yrs). Based on global distributions of Γ-Dual and Γ-MLE (not shown), Γ-Dual begins to converge to the same values as Γ-MLE for waters less than 60 years and when $\Delta/\Gamma < 2$ for IG-Dual.

The inability of the IG-Dual to estimate the values for Γ and Δ that were found in the IG-MLE as in the North Pacific is likely due to the the atmospheric histories of CFC-12 and SF_6. CFC-12 and SF_6 provide little information for the older portion of the TTD because their atmospheric concentrations are small or nonexistent for water parcels ventilated before the 1960s. The CFC-12 and SF_6 grew at roughly the same exponential rate meaning that their boundary conditions, though lagged in time, are very similar.

4.3.3 Using tracer methods to infer variability

In this section, changes in the apparent oxygen utilization (AOU=$[O_2]_{sat} - [O_2]_{model}$) (Mecking et al., 2006), mean age of IGs with $\Delta/\Gamma = 1$ constrained by CFC-12 (Waugh, 2003) referred to as Γ-CFC12, and the mean age of IG-Dual (Γ-Dual) using CFC-12 and SF_6 (Sonnerup et al., 2008) to infer ventilation variability is compared with changes in ideal age.

Time series from 1980 to 2009 are created by sampling each tracer annually in January for the southern hemisphere and June for the northern hemisphere roughly representing the seasons typically sampled on hydrographic cruises. Agreement between ideal age to Γ-Dual, Γ-CFC12, and AOU is quantified using linear correlation (R).

The ideal age tracer represents the balance between the delivery of young water from the surface and the aging of water parcels in the oceanic interior. A decrease in ventilation (either due to reduced transport or subduction) causes an accordant increase in ideal age, while an increase in ventilation would result in a decrease of ideal age. Changes in oxygen within the interior ocean can also be used to detect changes in ventilation. AOU represents the time-integrated consumption of oxygen in the oceanic interior and increases over time since the water parcel's last contact with the atmosphere. Assuming variability in biology is of lesser importance in driving AOU (Deutsch et al., 2006), AOU changes reflect changes in ventilation (Mecking et al., 2008, 2012; Emerson et al., 2004).

We find that changes in AOU generally follow changes in ideal age better than TTD mean ages (whether assuming fixed or varying Δ/Γ) over large portions of the thermocline in the subtropical Indian and Pacific Oceans (Figure 4.9). AOU also better represents changes in age in South Pacific (Figure 4.9 d, e, and f) and at the base of the thermocline where CFC-12 and SF_6 concentrations are close to the detection limit. Both Γ-Dual and Γ-CFC12 have nearly identical skill which suggests that the uncertainty that comes from assuming $\Delta/\Gamma = 1$ is negligible when inferring changes in circulation.

In the North Pacific along 30°N, AOU is significantly correlated with ideal age ($p < 0.1$) in most of the thermocline beneath the seasonal mixed layer at about 100m (Figure 4.9c). Averaged over the layers in the thermocline (NPIW and shallower), AOU explains about 50% of variance in ideal age. The strong relationship between AOU and ideal age in the mode water may result from the simple formation dynamics of NPMW and a relatively uniform biotic consumption of oxygen along its transport pathway. In the deep thermocline, the

variability in ideal age is small ($< 10\%$ of the mean) as is the variability in AOU. The most notable region where AOU is not significantly correlated with ideal age is in the eastern basin between the NPMW and NPIW from 200-400m depth which seems to be related to the sporadic entrainment of old waters.

On the same transect, Γ-CFC12 (Figure 4.9a) and Γ-Dual (Figure 4.9b) have slightly fewer regions that are well-correlated with ideal age when compared to AOU. Although we previously found large differences in the Δ/Γ ratio and Γ between the IG-Dual and IG-MLE, this does not seem to significantly affect the ability of Γ-Dual to track changes in ventilation and performs slightly better than AOU in the NPIW. Despite the fixed ratio of $\Delta/\Gamma = 1$, Γ-CFC12 also has comparable skill to Γ-Dual which suggests that the availability of both CFCs and SF_6 data is not necessary for studies examining variability of ventilation.

In the South Pacific Ocean, AOU is significantly correlated with ideal age essentially throughout the entire upper 1500m (Figure 4.9f). The main exception is the near-surface (above 250m) eastern portion of the basin (120°W to 80°W). Within the AAIW between 100°W to 140°W at about 600m depth, Γ-Dual (Figure 4.9d) and Γ-CFC12 (Figure 4.9e) are either uncorrelated with ideal age or are in fact negatively correlated. Whereas negative correlations between AOU and ideal age are insignificant, Γ-Dual and Γ-CFC12 do have areas where the anticorrelation are statistically significant. This is particularly problematic as it suggests that using IG-Dual constrained by CFCs and SF_6 could lead to false diagnoses of changing circulation.

In the South Indian Ocean, all three tracer-derived quantities (Figure 4.9g, h, and i) have broad agreement with ideal age over most of the thermocline. Γ-Dual has slightly higher correlations than AOU where in many regions correlations are just above the significance level ($R = 0.3$).

To illustrate how correlations between ideal age, AOU, Γ-Dual, and Γ-CFC12 could be used to quantify ventilation changes of water masses from hydrographic cruises, we present

timeseries in the form of Hovmoeller diagrams of each quantity on the NPMW isopycnal layer (Figure 4.10) along 30°N and on the AAIW isopycnal in the South Pacific (Figure 4.11) along 32°S. The NPMW isopycnal has a mean age of about 15 years (zonally averaged) which is significantly younger than the South Pacific AAIW at around 60 years. To aid the direct comparison the tracers, the mean has been removed from each time series and the resulting anomalies scaled by the standard deviation (red and blue lines respectively in Figures 4.10 and 4.11).

In the North Pacific, ideal age, AOU, Γ-CFC12, and Γ-Dual (Figures 4.10a, 4.10b, 4.10c, and 4.10d respectively) all show evidence for ventilation anomalies which oscillate with a 10-year period and do not propagate spatially. AOU, Γ-Dual, and Γ-CFC12 tend to exaggerate the negative phase of the oscillation and underestimate the positive phase of the ideal age anomalies. The time mean of each tracer shows older waters near the continental boundaries and young waters in the center of the basin. AOU tends to underestimate ideal age variability except in the central portion of the basin (compare red lines Figure 4.10 b and c). Γ-CFC12, however, tends to match the magnitude of the ideal age variability (compare red lines Figure 4.10 a and c) better than AOU and Γ-Dual, although any of these three tracers would suffice to diagnose a slowdown or increase in ventilation.

On the older AAIW isopycnal, the time evolution of ideal age and AOU (Figures 4.11a, 4.11b) agree well in the eastern portion of the South Pacific, whereas both Γ-CFC12 and Γ-Dual (Figures 4.11c, 4.11d) are poorly correlated with ideal age. Between 180°E to 280°E, ideal age variability shows a westward propagating oscillation with a roughly 25-year period. This feature is largely absent in the TTD-derived quantities, which are dominated by a trend towards younger ages over the 1980-2009 period. This trend is centered roughly around 1990 which corresponds to the atmospheric downturn in CFCs. Γ-Dual overestimates the age and age variability across all longitudes on this isopycnal whereas Γ-CFC12 fails to capture the correct age of the water east of 100°W. In contrast, the longitudinal pattern in AOU is

similar to that of the ideal age tracer, consistent with the better ability of AOU in tracking mean ages in the region and depth range discussed above.

In general, AOU can be more broadly used to diagnose changes in circulation than Γ-Dual and Γ-CFC-12. To determine how well this holds globally, we also calculated correlations between AOU and ideal age on three isopycnal layers 15, 19, and 26 (σ_2 =34.1, 35.0, and 36.0 kg m^{-3} respectively). Despite the fact that ventilation dynamics of these layers vary significantly from basin to basin, we find that AOU variability is significantly correlated with the ideal age tracer over most of these layers except within the oxygen minimum zones of the Indian, Pacific, and Atlantic Oceans. Overall the correlations between ideal age and AOU are significant on 82% of the grid points on layer 15, 90% of layer 19, and 93% of layer 26.

4.4 Discussion

Hydrographic measurements collected from the World Ocean Circulation Experiment Hydrographic Programme in the 1980s and 1990s (`http://www.nodc.noaa.gov/woce/wdiu/diu_summaries/whp/index.htm`) and the present day Global Ocean Ship-Based Hydrographic Investigations Program (GO-SHIP), `http://http://www.go-ship.org/`) provide an opportunity to diagnose decadal changes in ventilation. As CFC-11, CFC-12, and SF_6 are now routinely sampled on these cruises, changes in CFCs and TTD mean age have been used to diagnose changes in ventilation (Waugh et al., 2013; Waugh, 2014). However, our model results indicate that the TTD method constrained by CFC-11, CFC-12, and SF_6 have biases which can limit their effectiveness.

Part of these biases arise from the assumed IG form of the TTD that cannot reproduce the complex bimodal or thick-tailed TTDs which are common in the model-calculated TTD-BIR (Section 4.3.1). This also has implications for applications that rely on the dual-tracer inferred TTDs to infer the concentrations of other tracers whose surface boundary conditions are sensitive to the shape of the TTD such as anthropogenic carbon inventories (e.g. Hall

et al. (2002) and Tanhua et al. (2008)). A better form for waters with complex ventilation pathways may be addressed by the assumption of a mixture of IGs as done in the Mediterranean Sea by Stöven and Tanhua (2014). In that study, the assumption was made that the TTD was comprised of a fast, advective pathway represented by an IG with $\Delta/\Gamma = 0.6$ and a slower, diffusive pathway with $\Delta/\Gamma = 1.4$. For water parcels where the TTDs inferred from single-tracers with $\Delta/\Gamma = 1$ differed by more than 10 years, these mixture-IG TTDs provided more consistent estimates of the age. Alternatively, the maximum entropy approach (Kibler and Primeau (2006); Holzer and Primeau (2010)) given enough tracer information, can also be used to infer TTDs with more complex features than can be represented by an IG.

Our findings suggest that is important to identify instances in which TTD mean ages inferred from CFCs and SF_6 (assuming the form of a 1d IG) should and should not be used to diagnose changes in oceanic ventilation. Based on the results presented in this paper, we suggest the following four guidelines to be adopted by future studies seeking to use the TTD method to infer changes:

1. Ventilation is unaffected by the influence of either boundary currents or strong upwelling

2. The isopycnal of the water sample outcrops within the basin

3. Variability in temperature and salinity of the water parcel do not significantly change the solubility of the water parcel

4. The increase or decrease in ventilation can be confirmed by other metrics (e.g. AOU)

These criteria constrain the use of the 1d TTD method both horizontally (1.) and vertically (2. and 3.). The first criterion arises from results in Section 4.3.1 which showed that the IG-MLE was an adequate representation of the TTD-BIR within the main subtropical gyres where TTDs had one dominant ventilation pathway. Criterion (2.) is based on the

finding in Section 4.3.2 that the Γ-Dual has significant biases within the intermediate waters. This effectively bounds the effectiveness of CFC-12 and SF_6 constrained TTDs to isopycnals which lie within the ventilated thermocline. Mode waters in each of the basin satisfy criteria (1.) and (2.) whereas the formation of intermediate waters are often more complex and so violate (2.). The third criterion has been briefly addressed in this paper where we speculated that changes in saturation may cause biases towards higher Δ/Γ in IG-Dual.

Criterion (4.) comes from the fact that if we require that changes in AOU and TTD mean ages have to agree in sign in order to conclude a change in ventilation, on the transects shown in Figure 4.9 we would never diagnose the wrong change in circulation. As an alternative to AOU, changes in ventilation may also be independently confirmed by the multivariate regression, Laplacian transform method introduced by Robbins and Jenkins (1998) in the Atlantic using helium-tritium and applied to the Pacific by Sonnerup et al. (2007) using CFCs. With the routine measurement of both CFCs and SF_6 on current and future GO-SHIP hydrographic cruises, the CFC-12/SF_6 offset method introduced by Tanhua et al. (2013) also provides a viable way to validate a change in ventilation.

Changes in saturation may explain why AOU has a slightly higher skill at tracking changes in ventilation than TTDs constrained by CFCs and/or SF_6. Of the transient tracers, the solubility of CFC-11 has the strongest dependence on temperature, followed by CFC-12 and SF_6. The median global supersaturation in the near surface ocean follows this same ordering 6.3% for CFC-11, 5.6% for CFC-12, and 4.6% for SF_6 (values are from 1988 when the atmospheric growth rate for all three gases is still exponential and from the run with a saturated boundary condition). These supersaturated waters all exhibit changes in solubility of about 4% per month typically after the start of spring (April in the northern hemisphere, October in the southern hemisphere). In contrast, we find that supersaturation in oxygen (which has a comparatively weak dependence on temperature) outside the euphotic zone is often negligible. While the near-surface ocean is an extreme example of where saturation of

a water parcel can change rapidly, we many not be able to conclude that the age of a water mass has changed if it is contemporaneous with large changes in T or S.

A decreasing undersaturation of tracers in the mixed layer over time (Shao et al., 2013), which should produce a trend towards decreasing ages, was not found to influence correlations between TTD mean age and ideal age. CFC-12 and SF_6 concentrations from the run where the surface was determined by 1d gas exchange were used to infer TTDs with both fixed and varying Δ/Γ. However even assuming 100% saturation, correlations from these undersaturated TTD ages were not significantly different to those shown in Figure 4.9 suggesting that interannual variability in ventilation is larger than the bias caused by temporally varying saturation.

The results of this study make clear the continued importance of measuring CFCs and SF_6. While we showed that, as of yet, the dual tracer TTD inferred from CFC-12 and SF_6 is a poor representation of the true TTD, the decrease in atmospheric CFCs and continuing exponential growth of atmospheric SF_6 means that the CFC-12/SF_6 tracer pair may become a stronger constraint as their boundary conditions become increasingly dissimilar to each other. The decline in atmospheric concentrations of CFCs suggests that the skill of Γ-CFC12 to track changes in variability may be reduced in the future. However, we also inferred Γ using SF_6 (Γ-SF_6) as a constraint and found that correlations to ideal age were comparable to Γ constrained by CFC-12. This suggests that as a tool to diagnose determine ventilation variability, Γ-SF_6 may be used in place of Γ-CFC12 if there is at least one point in time where they diagnosed a similar change in ventilation.

4.5 Conclusions

An offline tracer transport model with a 1° resolution was used to calculate CFC-11, CFC-12, SF_6, oxygen, ideal age, and the model TTD (TTD-BIR). These tracers were then used to evaluate where the 1d TTD method can constrain the climatological and variability ven-

tilation of the ocean. The model did not reproduce observed temperature, salinity, and CFC-12 exactly, but the structure of the thermocline was sufficiently similar to suggest that the model was representing oceanic ventilation well enough to serve as a useful analogue to the real ocean. The IG approximation to the TTD-BIR were calculated from maximum likelihood estimators of Γ and Δ and referred to as IG-MLE. The Cramér-von-Mises metric was introduced as a way to compare the similarity of two TTDs, in particular the IG-MLE and the TTD-BIR.

The IG-MLE was found to be an adequate approximation of the TTD-BIR primarily within the subtropical gyres and most of the ventilated thermocline. The IG-MLE was an inadequate representation of the TTD-BIR in water masses which lie on strong gradients in age because TTDs here have features (wide shoulders or multiple peaks) which cannot be captured by a single IG. This could occur either at the base of the thermocline or at the horizontal boundaries of the subtropical gyres.

Modeled CFC-12 and SF_6 were then used to infer IGs with variable Δ/Γ (IG-Dual) and compared to the IG-MLE. For both very young water masses (< 5 years) and older water masses (> 60 years), IG-Dual differed significantly from the IG-MLE primarily because the IG-Dual had higher Δ/Γ ratios. This bias towards more diffusively dominated ventilation was attributed to the fact that a wide variety of TTDs with different Γ and Δ predicted similar values of pCFC-12 and pSF_6 for those age ranges. For younger waters, the estimated Γ was similar to the IG-MLE, but Δ tended to be much higher. For the older waters, Γ was biased low in the South Pacific and high in the Indian Ocean.

Variability in ideal age from the hindcast run was compared to variability of the mean age of TTDs (Γ) inferred from CFC-12 assuming $\Gamma/\Delta = 1$ (Γ-CFC12), Γ-Dual inferred from CFC-12 and SF_6, and AOU. All three methods were shown to correlate significantly with ideal age from 1980 to 2009 in many parts of the thermocline. AOU had higher skill in waters with ages greater than 50 years (e.g. intermediate waters) and could be used to a

greater depth within the water column where CFCs and SF_6 had yet to penetrate. In waters of around 20 years old or younger all three methods tended to underestimate the level of variability in ideal age. IG-Dual and IG-CFC-12 had comparable correlations with ideal age which suggests that to diagnose a change in ventilation, single tracer inferred TTDs are likely sufficient.

Overall, we found that 1d TTDs inferred from transient tracers can provide good approximations of water parcel age within the subtropical thermocline. From the results presented in this paper, we develop guidelines for where the TTD method could be reasonably be expected to provide robust estimates of changes in ventilation. However, because of biases potentially arising from tracer solubility or nonlinearities in atmospheric history we also recommend the use of independent methods to confirm the diagnosis of changes in ventilation.

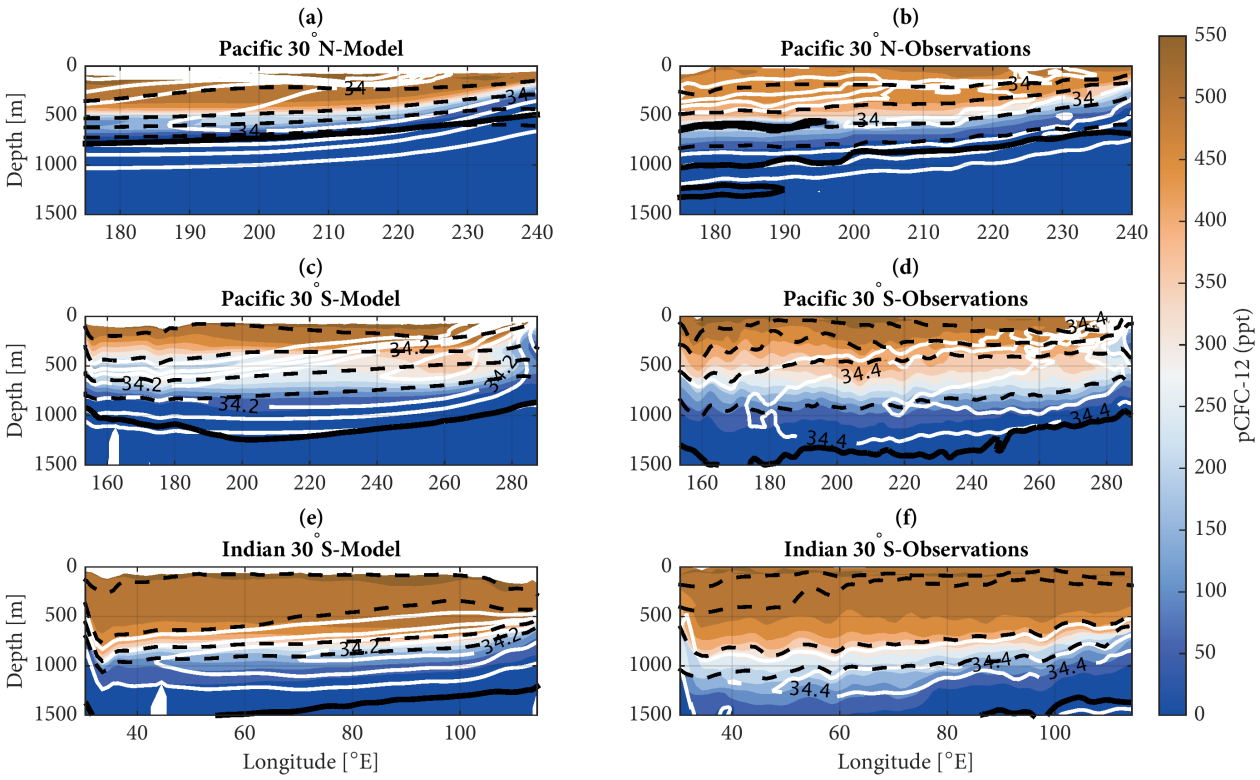

Figure 4.1: Comparison of zonal transects from (a, c, and e) the model to (b, d, and f) hydrographic cruises (a, b) in the North Pacific Ocean, (c, d) the South Pacific Ocean, and (e, f) and South Indian Ocean. White contours (in intervals of 0.1‰) show salinity with the labeled contour representing the minimum salinity characteristic of each basins' intermediate water. Colors represent chlorofluorocarbon-12 partial pressure (pCFC-12) in parts per thousand with the bold black contour representing a detection limit of 0.02 pmol kg^{-1} in units of concentration. Dashed contours represent the depths of the σ_2 = 34.1, 35.0, 35.6, and 36.0 kg m^{-3} isopycnals (from top to bottom, model layers 15, 19, 23, and 26).

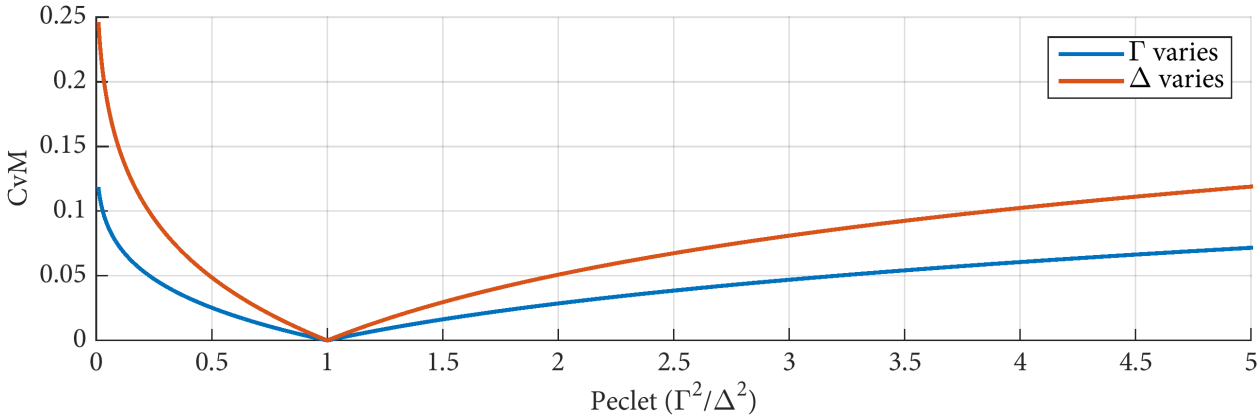

Figure 4.2: Comparison of an inverse Gaussian (IG) with mean age $\Gamma = 50$ yrs and shape parameter $\Delta = 50$ yrs IGs where the Peclet number varies from 0.1 to 5 by either varying Γ (black line, F_Γ in the text) or Δ (red line, F_Δ) using the Cramér-von-Mises (CvM) metric (see text for explanation of metric).

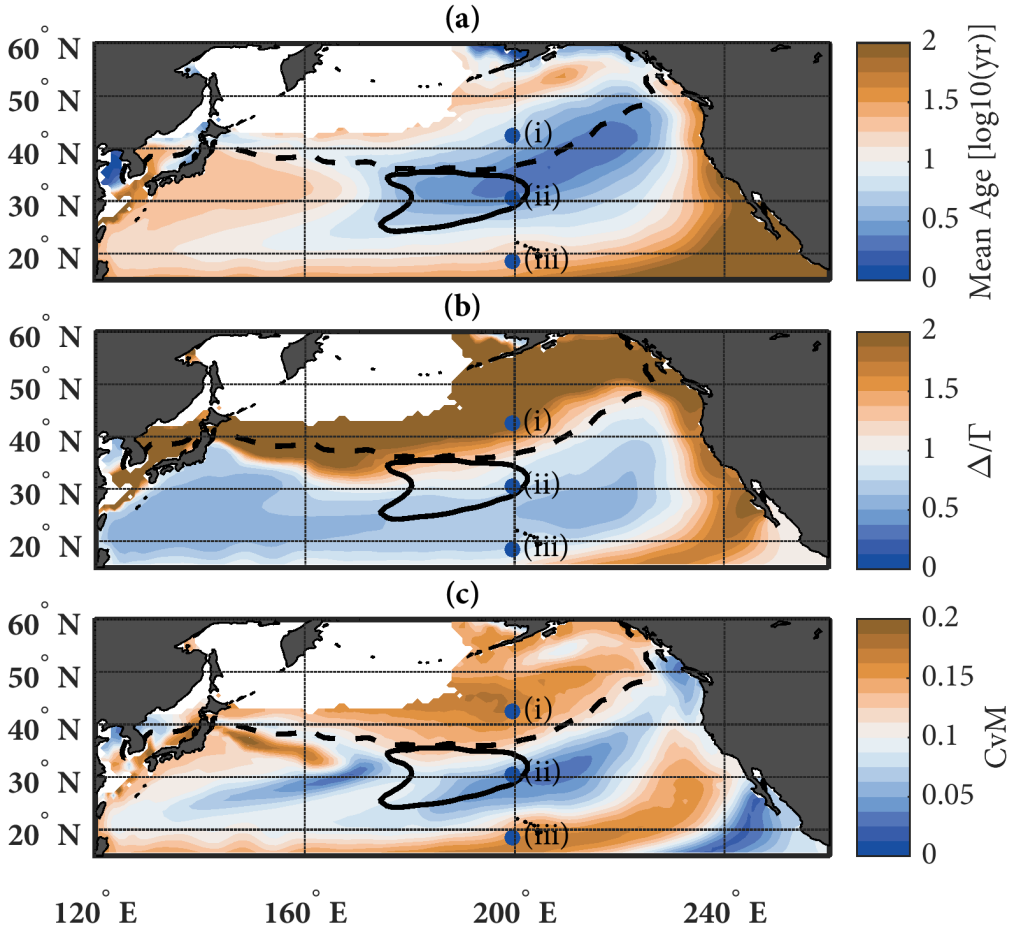

Figure 4.3: Properties of the IG approximation to the model's transit time distribution (TTD), calculated using the boundary impulse response method (TTD-BIR), on an isopycnal ($\sigma_2 = 34.1$ kg m^{-3}) containing the mode water in the North Pacific. The parameters of the IG are inferred using maximum likelihood estimators (IG-MLE) to calculate (a) the mean age (Γ) of the IG-MLE (and equivalently TTD-BIR) on $\log_{10}$ scale, (b) Δ/Γ which represents the importance of diffusive versus advective transport, and (c) CvM comparison to the TTD-BIR (c). The dashed contour shows the extent of the outcrop region and the solid black contour designates the potential vorticity minimum (1.5×10^{-6}m^{-1}s^{-1}) showing the core of the mode water. Dots with text labels (i), (ii), and (iii) are the locations of the TTDs shown in Figure 4.4.

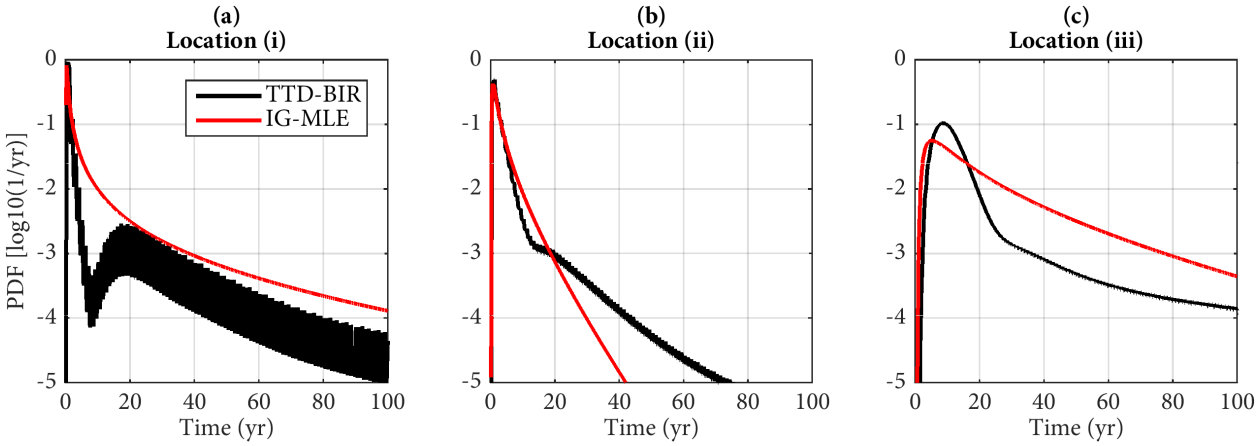

Figure 4.4: The distribution of transit times from 0 to 100 years as determined from the TTD-BIR (black) and IG-MLE (red) on the mode water isopycnal (layer 15, $\sigma_2 = 34.1$ kg m^{-3}) along 160°W within (a) the outcrop region, (b) core of the mode water, and (c) tropics. Geospatial location of each TTD are shown in Figure 4.3 as points labeled (i), (ii), and (iii).

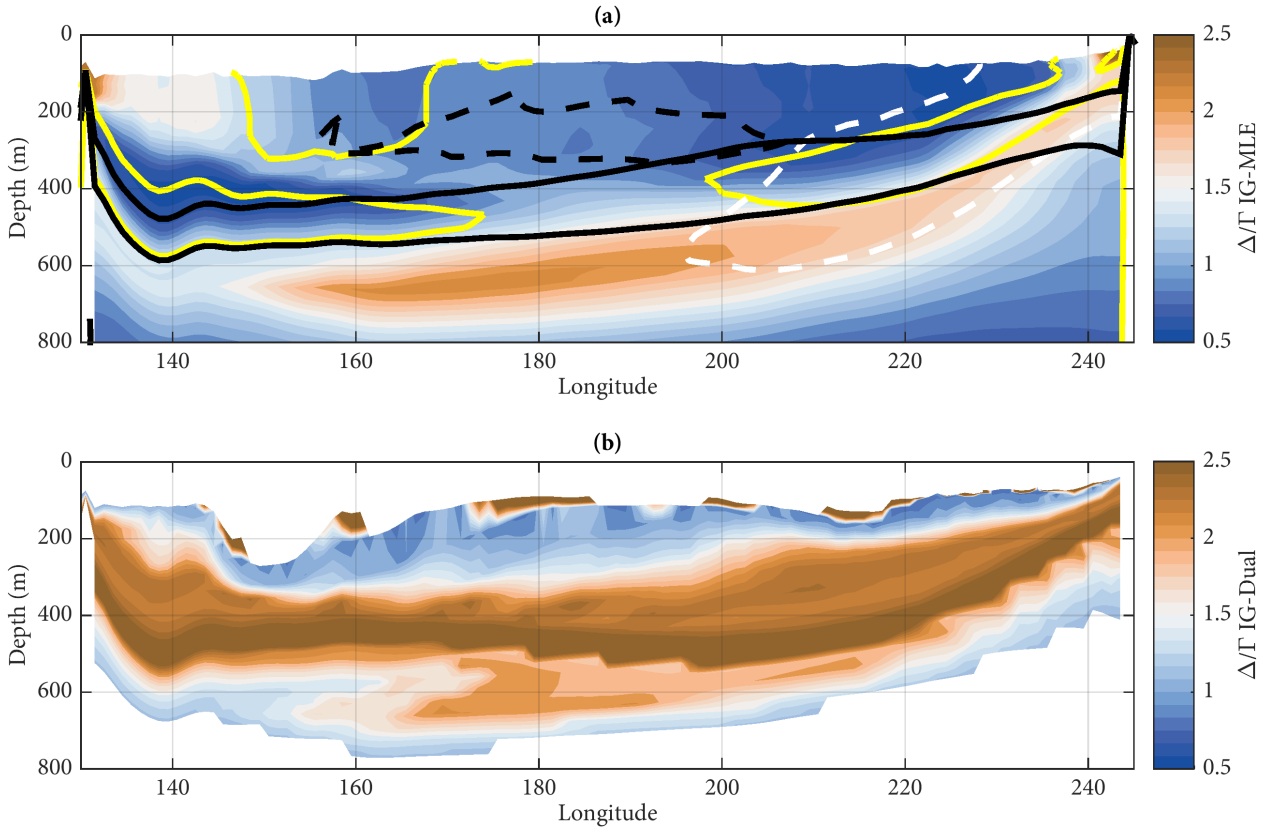

Figure 4.5: Transect along 30°N in the North Pacific showing the Δ/Γ ratio as determined from the (a) IG-MLE and (b) the IG inferred using CFC-12 and sulfur hexafluoride (IG-Dual, see text for details). Regions within the solid yellow contour have values of the CvM metric exceedig 0.1 when comparing the IG-MLE to the TTD-BIR, likely indicating that the assumption of 1d transport is poor. The solid black lines indicate the base of the mode water (shallower contour) and intermediate water (deeper contour) isopycnals. The dashed black contour indicates the PV minimum (1.5×10^{-6} m^{-1}s^{-1}) corresponding to the core of the mode water ($\sigma_2 = 34.1$ kg m^{-3}).

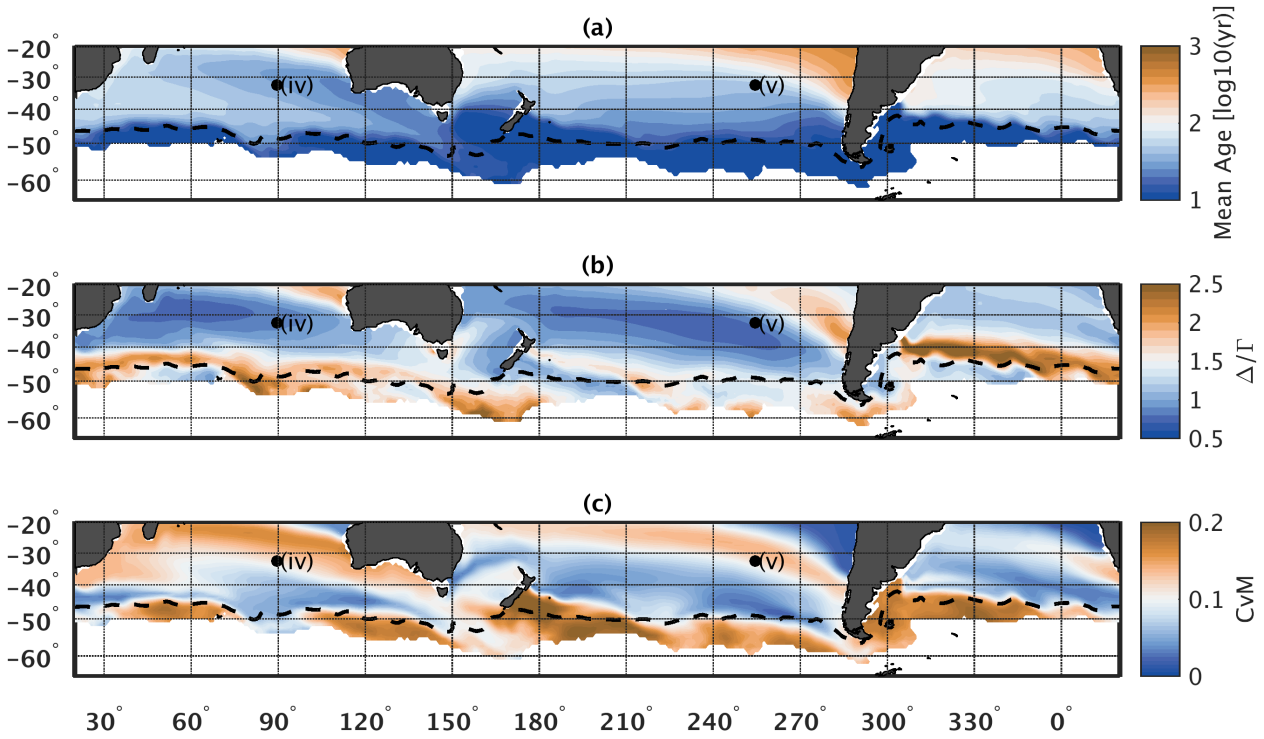

Figure 4.6: Similar to Figure 4.3, but for a denser isopycnal (layer 23, $\sigma_2 = 35.6$ kg m^{-3}) in the southern hemisphere within the core of the South Indian Ocean Antarctic Intermediate Water (AAIW). Note the difference in scales compared to Figure 4.4 for (a) TTD mean age and (b) Δ/Γ.

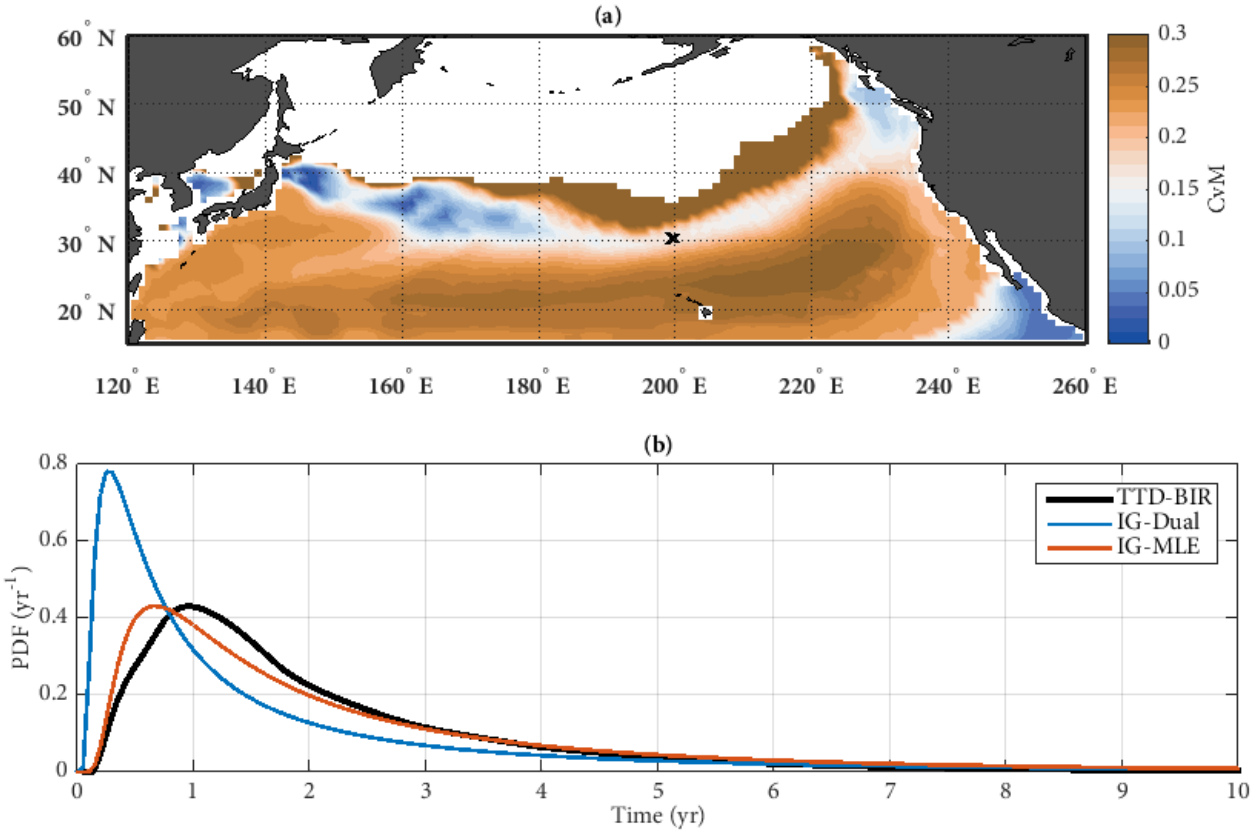

Figure 4.7: Comparisons of the IG-Dual TTD to (a) the IG-MLE on the mode water isopycnal (layer 15, $\sigma_2 = 34.1$ kg m^{-3}) using the CvM metric and (b) by showing the first ten years of the IG-Dual (blue line), IG-MLE (red line), and TTD-BIR (black line) at the point shown in (a) as an 'x' and also as location (ii) in Figure 4.3).

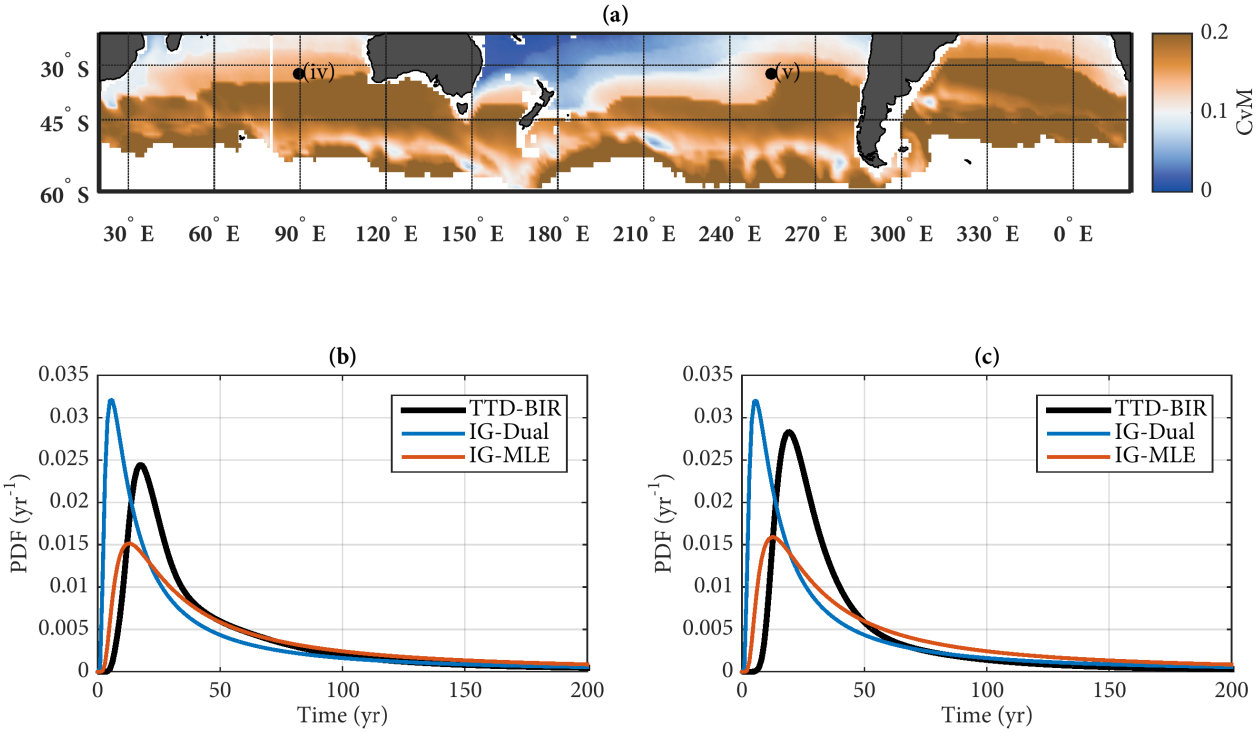

Figure 4.8: Similar to Figure 4.7, but on an isopycnal containing the South Pacific Ocean AAIW (layer 23, $\sigma_2 = 35.6$ kg m^{-3}) comparing the (a) IG-Dual to the IG-MLE using CvM comparison and (b, c) the first 200 years of the IG-MLE (red line), IG-Dual (blue line), and TTD-BIR (black line) at points (iv) and (v) shown in (a) and Figure 4.6.

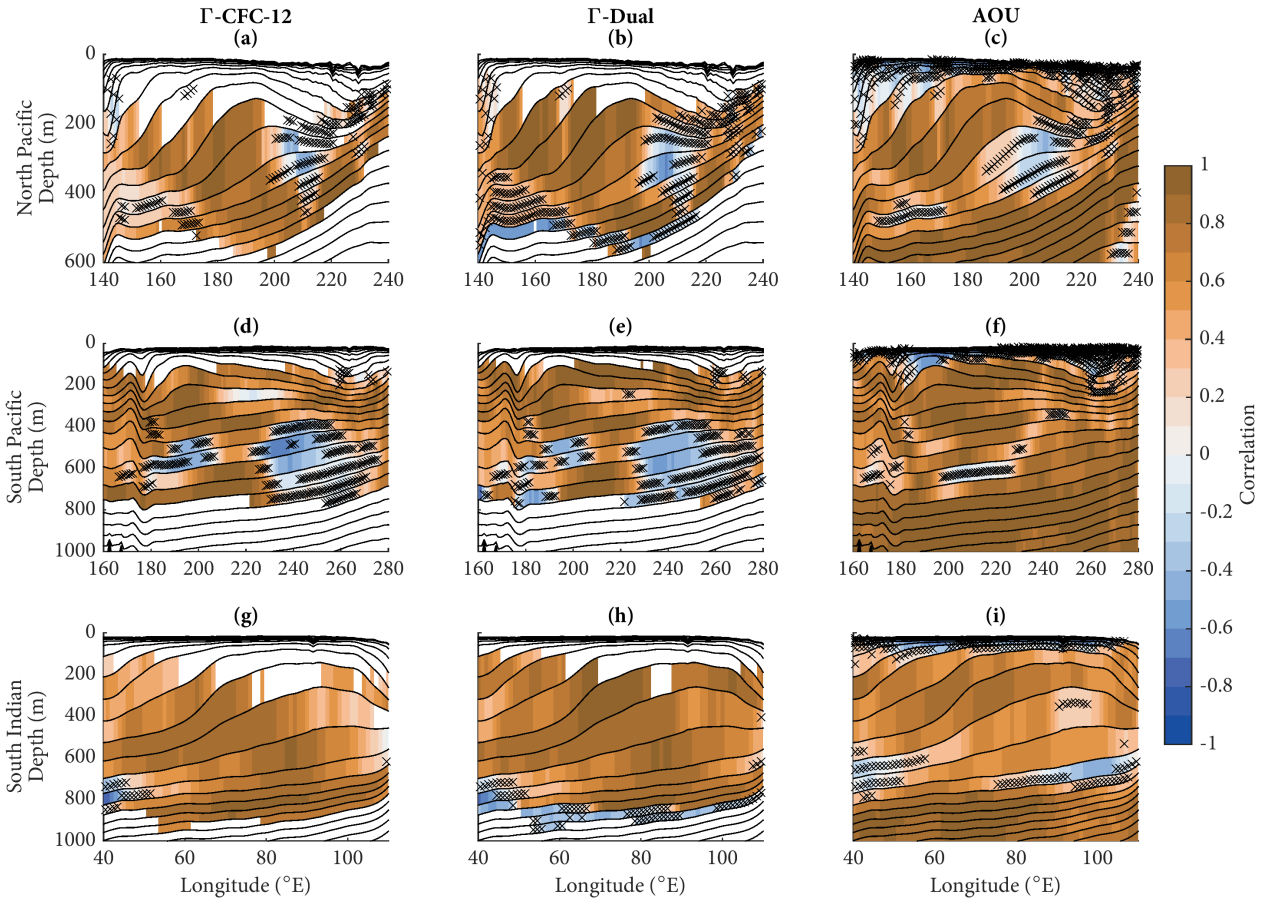

Figure 4.9: Correlations between ideal age variability from 1980-2009 and (a,d,g) Γ of TTDs inferred from pCFC-12 assuming $\Gamma/\Delta = 1$ (Γ-CFC12), (b,e,h) Γ from IG-Dual (Γ-Dual), and (c,f,i) apparent oxygen utilization (AOU=$[O_2]_{sat} - [O_2]_{measured}$) on zonal transects along 30°N in the North Pacific Ocean (a,b,c) and along 32°S in the South Pacific (d,e,f) and South Indian (g,h,i) oceans. Black contour lines represent isopycnals and hatching indicates correlations which are insignificant ($p < 0.1$).

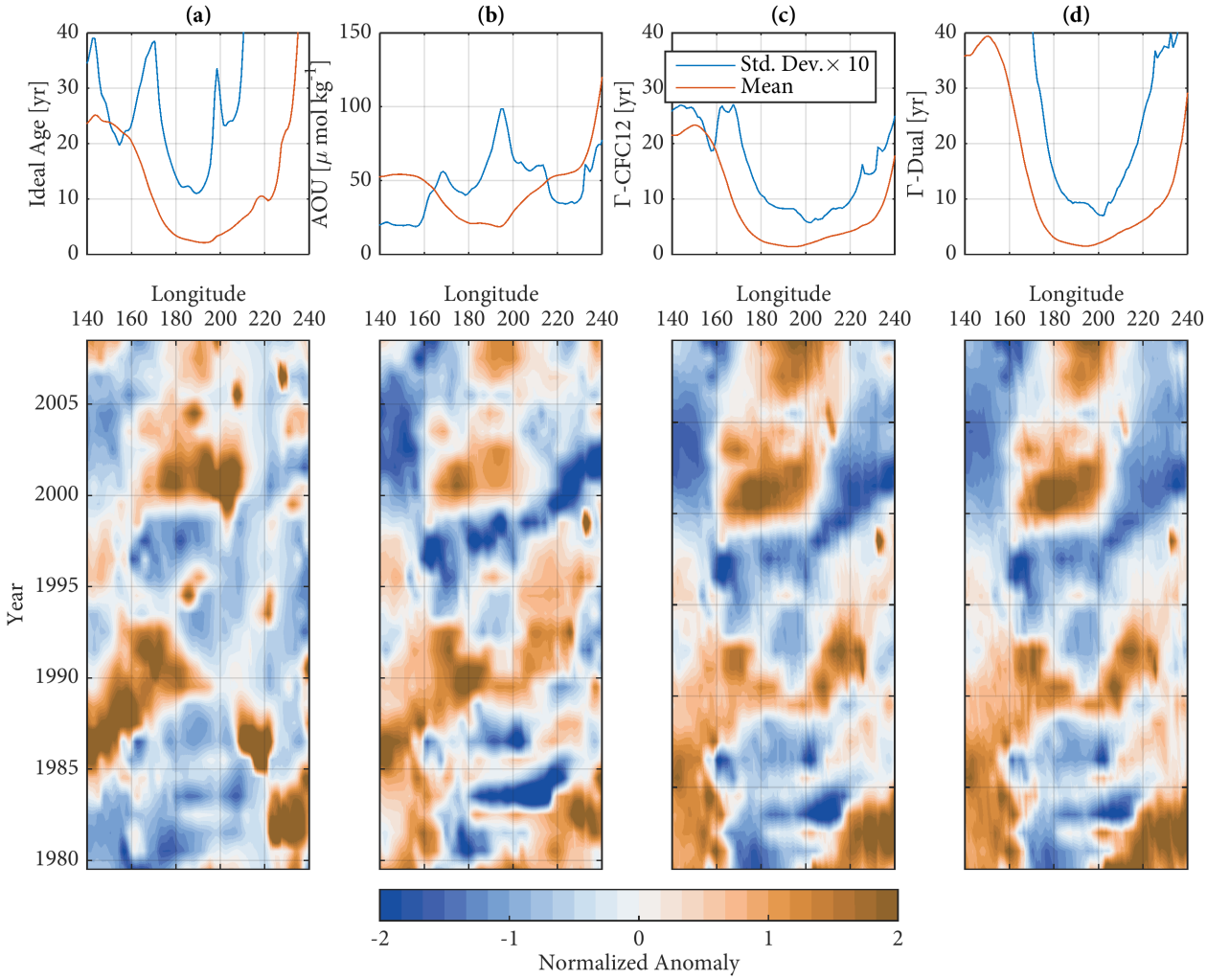

Figure 4.10: Time evolution of anomalies in (a) ideal age, (b) AOU, (c) Γ-CF12, and (d) Γ-Dual anomalies along 30°N in the North Pacific Ocean on the mode water isopycnal (layer 15, $\sigma_2 = 34.1$ kg m^{-3}). For easier comparison, the mean of each tracer from 1980-2009 has been removed (red lines in the upper panels) and the resulting time series normalized by their standard deviation (blue lines). Positive anomalies (red) indicate a slowing of ventilation whereas negative anomalies (blue) would suggest an increase in ventilation.

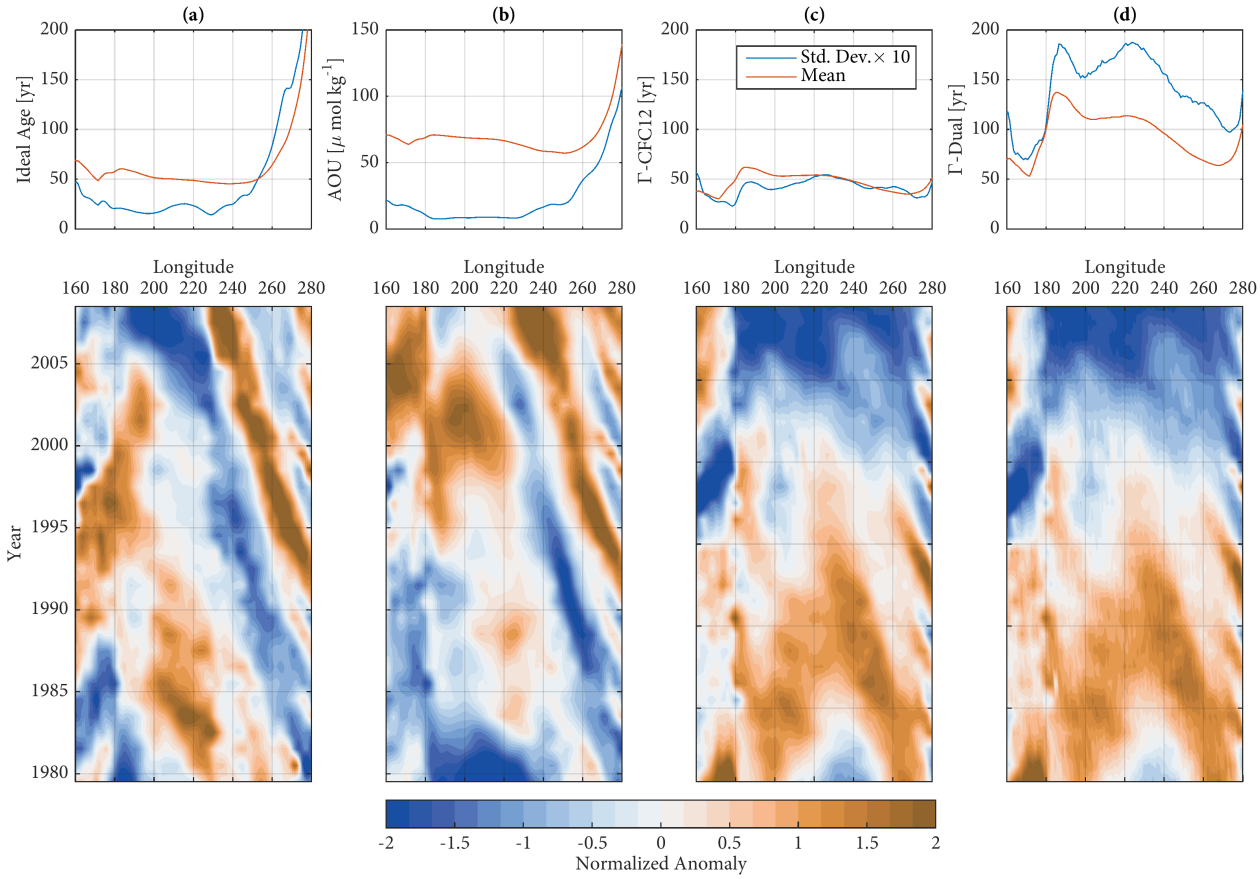

Figure 4.11: Similar to Figure 4.10, but along 30°S in the South Pacific Ocean on the AAIW isopycnal (layer 23, $\sigma_2 = 35.6$ kg m^{-3}) showing normalized anomalies in (a) ideal age, (b) AOU, (c) Γ-CFC12, and (d) Γ-dual.

Chapter 5

SOURCES OF MODE WATER FORMATION AND VARIABILITY USING AN ADJOINT TTD METHOD

5.1 Introduction

Mode waters of the world's oceans are so named because in a volumetric sense they are the most common density class of water within the thermocline. Along hydrographic transects, they can be identified as a subsurface minimum in stratification with nearly homogeneous tracer properties (McCartney, 1982). These waters are formed during the late winter when the mode water isopycnals outcrop in regions with deep mixed layers. The cooler surface temperatures during the primary subduction months lead to higher solubility of gases and the large volume of surface water that comes into contact with the atmosphere delivers gas-rich water parcels to the interior ocean. The timescales of formation and age (time since last contact with the surface) of these mode waters can be estimated from tracers like helium-tritium (Andrié et al., 1988), oxygen (Jenkins, 1987), and chlorofluorocarbons (Warner et al., 1996).

The subduction of water parcels from the surface into the thermocline is accomplished by Ekman pumping due to wind stress curl in the outcrop region and by lateral induction of water parcels in the mixed layer when the geostrophic current crosses strong gradients in mixed layer depth (Cushman-Roisin, 1987; Qiu and Huang, 1995). The annual subduction rate of surface waters into the thermocline can be calculated in a Lagrangian framework according to Woods (1985) as

$$S_{annual} = -\frac{1}{T}\int_0^T w_{tr}\ dt - \frac{1}{T}\int_0^T u_{tr}\cdot\nabla h\ dt \tag{5.1}$$

where T is a timescale of one year, w_{tr} and u_{tr} are the vertical and horizontal velocities along the path of the water parcel, and h is mixed layer thickness.

These subduction processes are sensitive to interannual changes in wintertime surface fluxes of heat and freshwater and the large-scale wind field that affect both Ekman transport and geostrophic flow. For these reasons, observed interannual variability in mode water volume, temperature, salinity, potential vorticity, and age have been in part attributed to climate modes of variability that can impact wintertime signatures of sea surface properties. In parts of the thermocline in the North Pacific, low-frequency decadal variability in oxygen and temperature have been diagnosed from both observational (e.g. Yasuda (1997) and Mecking et al. (2008)) and modeling studies (e.g. Ladd and Thompson (2002) and Deutsch et al. (2006)).

In each of these studies, the tracer variability could only be weakly related to the dominant surface mode of temperature variability in the North Pacific, the Pacific Decadal Oscillation (PDO). The PDO is defined as the first mode of variability (determined using empirical orthogonal functions) of sea surface temperature in the Pacific Basin between 20°N and 60°N (Mantua et al., 1997). As its name suggests, this mode shifts between a positive phase (cool SST anomalies in the west Pacific and warm SST anomalies in the east Pacific) and a negative phase (with opposite anomalies). An abrupt change in the PDO in the mid-1970s toward a warm phase has been referred to as a 'regime shift' in the North Pacific (Ebbesmeyer et al., 1991; Hare and Mantua, 2000).

In the Southern Ocean, the Southern Annular Mode (SAM) is the dominant mode of atmospheric variability and has been shown to have a particularly strong effect on sea surface temperature and mixed layer depth in the South Indian Ocean Basin (Lovenduski, 2005; Sallée et al., 2010). Studies of the Indian Ocean thermocline have largely shown multi-decadal trends in Indian Ocean Subantarctic Mode Water (ISAMW) towards younger ventilation ages (Waugh et al., 2013), positive temperature and salinity anomalies (Aoki, 2005), and higher

nutrient concentrations (Ayers and Strutton, 2013). These trends are linked to a trend towards stronger SAM between the 1960s and 1990s, though interannual variability (when considered by these studies) in these properties is largely uncorrelated to SAM.

The water parcels that comprise the mode water come from a myriad of surface locations with many different advective-diffusive timescales. Mixing prevents a simple one-to-one relationship between changes at the surface boundary of a tracer like temperature and the response in an interior water parcel. In the regions with strong formation, the variability at the surface may give a good estimate of the increase or decrease of the tracer in the interior, but away from the formation region that signal is diluted by mixing.

Green's function solutions of the scalar advection-diffusion equation can be used to answer the question of how water parcels are transformed and modified by the 3d oceanic circulation. A Green's function can be thought of as the response of an interior point to a change at the surface boundary. The evolution of a passive tracer (i.e. one that does not change the flow field itself) is well described by the scalar transport equation written as

$$\left[\partial_t + \vec{u}(\vec{x},t)\cdot\nabla - \nabla\cdot(\kappa(\vec{x},t)\nabla)\right] C(\vec{x},t) = R(\vec{x},t) \tag{5.2}$$

where C is the concentration of the tracer, $\vec{u}$ is the three dimensional velocity vector, κ represents tracer diffusivity due to the effect of eddies both in the vertical and horizontal, and R represents a known source term. Within the literature, the Green's function solutions to (5.2) are known as transit time distributions (TTDs).

This study investigates how oceanic transport (3d advection and diffusion) affects the response of the thermocline to a change (either in forcing or a tracer property) at the oceanic surface. We use an offline transport model, Offtrac, to calculate TTDs between the surface and mode waters in the South Indian and North Pacific Oceans. In Section 5.2, the mathematical framework of TTDs and the adjoint TTD concept are described in more detail. This section also describes our configuration of the Hallberg Isopycnal Model (HIM), a general

circulation model which is used to calculate the fields necessary to integrate Offtrac. Section 5.3 discusses how interior variability of a tracer represents a modification of the surface boundary condition by the TTD using Fourier analysis. Section 5.4 uses adjoint TTDs calculated using climatological transports to identify the main formation regions and ventilation timescales of mode water. In Section 5.5, changes in the ventilation of mode waters due to variable circulation is analyzed using adjoint TTDs calculated from hindcast transports. Section 5.6 summarizes the key points of this study including the development of the adjoint TTD method and the implications of our results to observational studies of decadal changes in thermocline ventilation.

5.2 Methods

5.2.1 Transit time distributions

Oceanic ventilation in the formulation described by (5.1) and (5.2) can be interpreted as the subduction of water from the surface into the oceanic interior and its subsequent horizontal transport and mixing. The TTD (denoted by $G(\vec{x},t)$), is a probability density function that represents the distribution of the advective-diffusive timescales (transit time) for water parcels which originated at the surface boundary and arrived at a location in the ocean interior.

Defining the terms within the square brackets in (5.2) as the linear operator L, the equation is rewritten as

$$LC(\vec{x},t) = R(\vec{x},t). \tag{5.3}$$

If $R(\vec{x},t)$ is defined as a delta-function $\delta(\vec{x}-\vec{s},t-\tau)$ (i.e. a one-time impulse of tracer at the surface), then the resulting $C(\vec{x},t)$ is the Green's function G. The general solution for

any boundary condition can thus be be written as

$$C(\vec{x},t) = \int_0^\infty \int_{\S} G(\vec{x},t;\vec{s},\tau) R(\vec{s},\tau)\ ds\ d\tau \tag{5.4}$$

where C is the time-varying value of a tracer at a location $\vec{x}$, $\vec{s}$ is a point on the spatial boundary S (often defined to be the surface mixed layer), and τ represents time elapsed since some reference year. G can be interpreted as the response of the system defined by L to a boundary impulse at $\vec{s}$ and time τ. Analytic forms of Green's function solutions to a number of simplified, but geophysically relevant domain geometries can be found in Holzer and Hall (2000).

In general circulation models (GCMs), TTDs from the surface and to interior can be calculated using the boundary impulse response (BIR) method (Primeau, 2005; Peacock and Maltrud, 2006; Maltrud et al., 2009) where the boundary condition for the passive tracer is a δ-function as described previously. The time evolution of the concentration of this BIR tracer at a point within the ocean, calculated by integrating (5.2) in time, represents the true model TTD between the surface boundary and an interior water parcel.

If $\vec{u}$ and κ in a model are cyclostationary (i.e. they are time independent except for a fixed cyclical variation in time), the model TTD can be calculated using a single BIR. However if $\vec{u}$ and κ vary interannually, the TTD becomes time dependent and requires a separate BIR run for every year. Maltrud et al. (2009) performed simulations in an eddy-resolving GCM where the BIR tracer was injected at five different times (separated by two years) and integrated forward for about 100 years. Comparing the resulting BIRs at five different locations at various depths, they showed that at each location the BIRs differed the most for smaller transit times which represented the advective part of the distribution, but the diffusive tails of the distribution were similar.

When calculating TTDs in a model if the BIR tracer is injected over the entire surface ocean S, only a spatially homogeneous boundary condition can be used in (5.4). To apply

a separate boundary condition at every surface point, a BIR simulation would have to be performed from every individual surface point. However, this is usually impractical since the number of simulations required equals the number of surface grid points. As a compromise between treating the surface as a homogeneous source and individual points, the surface can be subdivided into discrete regions. Then separate BIR runs can be performed where the δ-function is applied to each subset of the oceanic surface (Khatiwala et al., 2009; Primeau, 2005) to determine the influence of different surface regions on TTDs in the interior.

5.2.2 Adjoint TTDs

The BIR method above calculates TTDs from the surface (or patches of the surface) to every point in the interior. If instead the TTDs that connect a single interior water parcel (or water mass) to the surface are desired, Green's functions of the adjoint transport equation can be used.

Operators such as L defined by (5.2) can be interpreted as mapping a state vector ψ through the space defined by the operator onto a new state vector Ψ. The adjoint to an operator L denoted as $L^\dagger$ effectively does the converse, mapping Ψ back onto ψ. This symmetry is formally expressed as

$$\langle L\psi, \Psi \rangle = \left\langle \psi, L^\dagger \Psi \right\rangle \tag{5.5}$$

where $\langle \cdot, \cdot \rangle$ is an inner product. The adjoint operator is orthogonal to the forward operator at every timestep, that is $\left\langle L, L^\dagger \right\rangle = 1$. The adjoint to the advective portion of L is trivial necessitating only a time-reversed integration. However, the time-reversed diffusive operator is ill-defined as it suggests upgradient diffusion. Instead Holzer and Hall (2000) showed that the adjoint to the transport equation is

$$\left[\partial_t - u(\vec{x}, t) \cdot \nabla - \nabla \cdot (\kappa(\vec{x}, t) \nabla)\right] C(\vec{x}, t) = 0 \tag{5.6}$$

where it is key to note that this operator is integrated backwards in time with the sign of the velocities reversed but with down-gradient diffusion. They further demonstrated that the Green's functions for the forward and adjoint equations were related by

$$G(\vec{x}, t; s, \tau) = G^{\dagger}(\vec{s}, \tau; \vec{x}, t), \tag{5.7}$$

where $G^{\dagger}(\vec{s}, t)$ denotes the adjoint Green's function. Thus, computing Green's functions from every point $\vec{s}$ on the surface S to an interior point $\vec{x}$ using the forward transport equation is equivalent to computing Green's functions within the interior to the surface using the adjoint transport equation. For clarity, the forward TTD will be denoted by $G(\vec{x}, t)$ and the adjoint TTD by $G^{\dagger}(\vec{s}, t)$.

5.2.3 Computing adjoint Green's functions offline

TTDs using the forward BIR method can be calculated in most GCMs relatively simply. However, adjoint TTDs are difficult to calculate in a GCM because the equations that represent the thermodynamic, barotropic, and baroclinic ocean dynamics are highly nonlinear. Few GCMs in active use have adjoint formulations since they require a great deal of logistical (and computational depending on method) effort to implement. The Regional Ocean Modeling System essentially rewrites the entire dynamical core to solve the adjoint forms of its governing equations (Moore et al., 2004) whereas the Massachusetts Institute of Technology GCM computes the approximate adjoint solution by calculating the approximate tangent solution of the forward model (Marotzke et al., 1999).

For the problem of adjoint TTDs, the complexity of running a full adjoint GCM can be sidestepped by only integrating the adjoint transport equation. The fields necessary to integrate this equation, velocity $\vec{u}$ and diffusion coefficients κ, can be saved from forward integrations of the GCM. $\vec{u}$ is transformed for use with the adjoint equation by reversing the signs of the transports. An adjoint form for $R(\vec{x}, t)$ must also be derived ($R^{\dagger}$) which for

TTDs is simply a δ-function in the interior instead of at the surface. Note here that our approach of directly integrating the adjoint transport equation differs from the so-called fast matrix solver technique used to calculate adjoint TTDs in other studies (e.g. Primeau (2005) and Khatiwala (2007)) which relies on the inversion of the matrix equation representation of (5.2).

To calculate adjoint TTDs, we use the adjoint configuration of the offline transport model, which is adapted from the scalar transport portion of HIM, a GCM whose fundamental equations are formulated in an isopycnal coordinate framework (Hallberg and Gnanadesikan, 2006). The model is globally configured with realistic topography and coupled to a sea-ice model. The surface is forced using Coordinate Ocean Reference Experiment version 2 forcing described in Large and Yeager (2008). It is spunup for 450 years using the normal-year forcing, which is sufficient to bring the thermocline into pseudo-equilibrium. The interannually varying version of the forcing from 1948-2009 is then applied twice. Horizontal mass transports, diapycnal velocity, and isopycnal thickness are saved every five days during the second loop. Climatologies of these fields are created by averaging the hindcast fields between 1980-1989.

Offtrac integrates the forward tracer transport equation in isopycnal coordinates.

$$[\partial_t + \vec{u_\rho}(\vec{x_\rho}, t) \cdot \nabla_\rho]C - \partial_\rho(\kappa \nabla_\rho h) \cdot \nabla_\rho C(1/\partial_\rho h) = R(\vec{x}, t) \tag{5.8}$$

where h is isopycnal thickness and the subscript ρ (density) reinforces the idea that the horizontal components are pointed along isopycnal (epipycnal) surfaces and the vertical component is diapycnal. As shown in (5.6), the adjoint transport equation in isopycnal coordinates is very similar to the forward equation except that the direction of the velocities are reversed and the equation is integrated backwards in time.

One difference in numerically solving the adjoint tracer transport equation in isopycnal coordinates versus level coordinates is the treatment of vertical mixing. In most level co-

ordinate transport models, the diffusion operator is rotated so that it is locally oriented in the along-isopycnal and cross-isopycnal directions (the so-called Redi diffusion tensor (Redi, 1982)). In all three directions then, the diffusive transport of tracers is irreversible and down-gradient. In isopycnal coordinates by contrast, diapycnal diffusion is characterized as an explicit transport of mass (i.e. a form of advection) and so is reversible.

Adjoint TTDs can be calculated using a method similar to the BIR method for forward TTDs. Following Fukumori et al. (2004), $R^\dagger$ for a passive tracer is set to 1 at the interior points from where $G^\dagger$ will be calculated. This condition is enforced for a year to average over the effect of the seasonal cycle. At the end of each timestep, the surface concentration of the adjoint tracer is set to 0. $G^\dagger$ then is the flux of the tracer into each grid cell of the oceanic mixed layer (saved every 25 days).

This study focuses on mode waters in the North Pacific and South Indian Oceans. The points where we initialize the adjoint tracer are chosen based on density and potential vorticity (PV) criteria. North Pacific Mode Water (NPMW) is defined as all the grid points in the North Pacific where PV is less than 1.0×10^{-6} m^{-1}s^{-1} and whose σ_2 anomalies are between $34.10 - 34.35$ kg m^{-3}. ISAMW is defined as all points in the Indian Ocean basin equatorward of 40°S where PV is less than 0.5×10^{-6} m^{-1}s^{-1} and σ_2 between 35.00-35.18 kg m^{-3}. The grid points that match these criteria are shown in Figure 5.1 for NPMW (black) and ISAMW (red). Climatological adjoint TTDs for each mode water are calculated by injecting the tracer at the end of December and integrating backwards in time using climatological transports for 1000 years using a 5-day timestep.

In addition to these climatological TTDs, we also calculate the time-dependent $G^\dagger$ using transports which vary interanually (i.e. the HIM run with interannually varying atmospheric forcing). Because the location of the mode waters in the interior do not change significantly over the hindcast period (1948-2009), the same regions of the mode water as those used for the climatological TTD are initialized with the adjoint tracer. A total of 84 runs are

performed (1 run per mode water initialized every year between 1968 and 2009). Because the hindcast period is relatively short, the model is only integrated backward in time for 20 years. Note that by only integrating for 20 years, we are only accounting for surface water parcels that reach the mode water within that time frame. The mode waters are relatively young (< 4 years), and (similar to Maltrud et al. (2009)) we find that most of the variability occurs in the first 10 years of $G^\dagger$.

5.2.4 Applications of adjoint TTDs

To characterize the contribution of water from an individual surface point to an interior water parcel, we define the volume fraction (V_f) to be the amount of water formed at a surface grid point and we define the time since last contact with that surface point as $\Gamma^\dagger$, which both can be calculated from the adjoint TTD as in Primeau (2005).

V_f quantifies the fraction of the water parcel that originated at an individual surface point $\vec{x}$ and is given by

$$V_f(\vec{x}) = \frac{\int_0^{t_f} G^\dagger \vec{x}, t \; dt}{\int_S \int_0^{t_f} G^\dagger(\vec{s'}, t) \; dA \; dt} \tag{5.9}$$

where t_f is the length of the adjoint integration, S is the entire surface of the ocean, s' is a point on S, dA is the area represented by s'. This equation is thus the accumulated flux of the adjoint tracer divided by the total inventory of the tracer that has reached the mixed layer by the end of the integration.

In order for $G^\dagger$ to be used as a probability density function (and thus to calculate the mean of the distribution), a normalization constant N must be found such that $1/N \int_0^\infty G^\dagger dt = 1$. The normalized adjoint TTD will be denoted as $\tilde{G}^\dagger$. The mean of the distribution, $\Gamma^\dagger$, is then given by

$$\Gamma^\dagger(\vec{s}) = \int_0^\infty \tilde{G}^\dagger(\vec{s}, t) t \; dt \tag{5.10}$$

which represent the average of all the transit times of water parcels that originating from a

single interior point and arrive at a single surface point.

5.2.5 Approximating $G^\dagger$ as an inverse Gaussian

The two-parameter Inverse Gaussian distribution (IG) is the Green's function solution of (5.2) in 1-dimension with constant u and κ and is given by

$$G(t,\Gamma,\Delta) = \left[\Gamma^3/\left(4\pi\Delta^2 t^3\right)\right]^{1/2} \exp\left[-\Gamma(t-\Gamma)^2/4\Delta^2 t\right] \tag{5.11}$$

where Γ is the mean of the distribution and Δ is a shape parameter (Holzer and Hall, 2000). We note that in many statistical texts (e.g. Seshadri (1999)), the functional form differs slightly from (5.11), but is essentially the same given a change of variables where $\Delta = \sqrt{\Gamma^3/2\lambda}$. The choice of Δ versus λ is convenient for this problem as the Peclet number (the ratio of advective transport to diffusive transport) for the flow can be written as $Pe = \Gamma^2/\Delta^2$ (Waugh, 2003).

The maximum likelihood estimators (MLE) for the adjoint IG parameters $\Gamma^\dagger$ and $\lambda^\dagger$ (and thus also $\Delta^\dagger$) can be computed from $G^\dagger$ to find a 1d approximation. The MLE for $\Gamma^\dagger$ is identical to (5.10) (i.e. the mean of the TTD-BIR and IG-MLE are equivalent). The MLE for $\lambda^\dagger$ is given by

$$1/\lambda^\dagger = \int_0^{t_f} \tilde{G}^\dagger(t)(1/t - 1/\Gamma^\dagger)\, dt, \tag{5.12}$$

where t_f is the largest transit time, which for the real ocean would be ∞, but here in our runs of Offtrac is the total integration time.

5.3 Fourier analysis of 1d TTDs

TTDs in their mathematical interpretation as Green's function solutions to the transport equation represent the response of an water parcel to an impulse at the boundary. The convolution of a Green's function G with a boundary condition R in (5.4) means that the

resulting variability in the oceanic interior of a conserved tracer is a result of the modification of a time-varying surface boundary condition by the Green's function.

The effects of G on modifying R to create C are examined using properties of the Fourier transform. First we define $R(\vec{s},t) = \delta(x-\vec{s_0})r(t)$ (i.e. a boundary condition that has both a spatial $\delta(x-\vec{s_0})$ and time-varying component $r(t)$), so that (5.4) becomes only an integral in time. This choice for R represents a tracer whose interior variability comes from one point at the surface and whose boundary condition depends only on time. We then invoke the convolution theorem (Bracewell, 2000) which states that given two function g and h and their Fourier transforms $\hat{g}$ and $\hat{h}$,

$$g(t) * h(t) = F^{-1}[\hat{g}(f) \cdot \hat{h}(f)] \tag{5.13}$$

where f is angular frequency, $*$ is the convolution operator, and F^{-1} represents the inverse Fourier transform operator. For the purposes of this study, $g(t) = G(t)$ and $h(t) = r(t)$. According to the convolution theorem, the variation of a tracer in the interior $C(t)$ is the result of the TTD behaving like a spectral filter on $r(t)$.

We first discuss (5.13) in the advective and diffusive limits of the IG solution to $G(t)$. In the limit of purely advective pathways ($\Gamma >> \Delta$), the 1d TTD is a δ-function centered around Γ whose Fourier transform is given by $\hat{G} = \exp(-if\Gamma)$. All frequencies would thus be 'passed' without attenuation by this filter. However, this filter does have a linear phase response which means that $C(t)$ will be shifted relative to $R(t)$ by a lag of Γ.

Purely diffusive IGs ($\Delta >> \Gamma$) are Gaussian functions centered around Γ with a width Δ. The Fourier transform of a Gaussian is also a Gaussian, so the TTD would behave a like a bandpass filter with a width $1/\Delta$ and centered around a frequency $2\pi/\Gamma$. While Gaussian filters centered around 0 have zero phase response, the shift theorem (Bracewell, 2000) states that shifting of the Gaussian to be centered around Γ introduces a linear phase, $\exp(-if\Gamma)$, in Fourier space. Thus, $C(t)$ in a diffusive system will be also lagged relative to $R(t)$ by Γ.

To examine flows where advective and diffusive transport are of comparable importance, we apply the Fourier transform to (5.11) and find that

$$\hat{G}(f) = \exp\left[\frac{\Gamma^2 - \Gamma^{3/2}\sqrt{\Gamma - 8\pi i\Delta^2 f}}{2\Delta^2}\right]. \tag{5.14}$$

The properties of the IG effective filter can be understood by looking at the magnitude and phase of the IG Fourier transform.

The frequency response of the filter (i.e. attenuation as a function of f) is given by $|\hat{G}(f)| = \sqrt{G^*(f)G(f)}$ where G^* is the complex conjugate of G. The functional form of $\hat{G}(f)$ for the IG (5.14) suggests that the magnitude $|\hat{G}(f)|$ exponentially decays as a function of f. The power spectra of $C(t)$ would thus be redder than the spectra of $R(t)$. The highest frequency that will be passed by a low-pass filter is referred to as the corner frequency f^* where $|\hat{G}(f^*)| = 0.5$ and for the IG is given by

$$f^*(\Gamma, \Delta) = \frac{\log(2)^{1/2}}{\Gamma^3\Delta}\left(\Gamma^2 + \Delta^2\log(2)\right)^{1/2}\left(\Gamma^2 + \Delta^2\log(4)\right) \tag{5.15}$$

and the associated corner period (T^*) is given by $T^* = 1/f^*$.

For typical values of Γ and Δ (ranging from 0 to 50 years) in the thermocline, T^* ranges from 5 to about 140 years (Figure 5.2). For water masses whose ventilation is dominated by advective transport ($\Delta/\Gamma < 1$), f* is less sensitive to changes in Γ. Water parcels where $\Delta/\Gamma > 1$ are very sensitive to changes in Γ likely because the increase in age allows more time for along-isopycnal diffusion to 'dilute' variability from $R(t)$.

The phase of the 'filter' is determined as $\theta(f) = \arctan(-\mathrm{Im}(\hat{G})/\mathrm{Re}(\hat{G}))$ which for the IG is

$$\theta(f) = \frac{\Gamma^{3/2}}{2\Delta^2}\sqrt{\frac{\sqrt{\Gamma^2 + 16f^2\Delta^4} - \Gamma}{2}}. \tag{5.16}$$

Whereas the advective and diffusive limits of tracer transport had a linear phase response

which meant that the $C(t)$ could be lag-correlated to $R(t)$, (5.16) shows that the phase depends nonlinearly on f. This means for flows where both advection and diffusion must be considered, $C(t)$ and $R(t)$ may not be linearly correlated even accounting for a time lag.

5.4 Climatological adjoint TTDs

We next use the adjoint TTDs calculated from climatological transports to understand the sources of NPMW and ISAMW and the associated timescales of ventilation for these water masses. We then approximate the adjoint TTDs as an IG, using the maximum likelihood estimators for Γ and Δ, and compare the relative roles of advective and diffusive transport between the mode waters and grid points at the surface.

As expected, V_f for NPMW is largest in the central North Pacific centered around 180°E and 30°N, where the NPMW is thought to be formed within the model (Figure 5.3a). Integrating V_f in the region around the Kuroshio extension with deep wintertime mixed layers (within black contour denoting 150m mixed layer depth) shows that about 26% of the total volume of the mode water is formed there. Large V_f can also be found outside of these deep mixed layer regions, particularly between about 150°W and 140°W. The sharp gradient in mixed layer depth between these two regions along with large zonal velocities suggests that the lateral induction term of (5.1) characterizes the subduction of NPMW in this region, consistent with other observationally-based studies in the North Pacific (Bingham, 1992; Nakamura, 1996; Suga et al., 1997).

The mean age, $\Gamma^\dagger$ calculated from the adjoint TTDs, shows that the representative timescales for water parcels leaving the surface of the North Pacific before entering NPMW range from about 2 years to 50 years (Figure 5.4a). The adjoint TTDs with the smallest $\Gamma^\dagger$ also tend to have high V_f. $\Gamma^\dagger$ of the adjoint TTDs just poleward of 45°N (north of the formation region) are large despite their proximity to the mode water. There the mixed layer density is always greater than the density of the NPMW. Water parcels originating in these

regions must first subduct beneath the NPMW and then slowly diffuse diapyncally into the NPMW.

In the Southern Hemisphere, regions with large V_f for ISAMW are also regions with deep mixed layers (Figure 5.4b), but are not co-located with sharp gradients in mixed layer depth (not shown). This suggests that the formation of ISAMW may occur predominantly via Ekman pumping, while lateral induction plays a smaller, but still important role. In these regions where mixed layer depth exceeds 200m, the integrated V_f is about 64% of the total volume of ISAMW. Around 35° S between 20°E and 120°E, meridional gradients in mixed layer depth combined with large-scale equatorward Ekman transport shows that the remaining roughly 35% of ISAMW is formed via lateral induction. Large V_f of ISAMW can be found in the region stretching from Africa around 20°E to the eastern edge of Australia around 160°E. The local, subduction driven ISAMW formation leads to relatively low $\Gamma^\dagger$ along this entire region (between 2 to 10 years, Figure 5.4b). The only other significant formation region is in the South Atlantic (40°S between 20°W and 0°W), which contributes about 1% to the total ISAMW on a timescale of around 30 years.

Integrating V_f of NPMW over the southern hemisphere and V_f of ISAMW over the northern hemisphere shows that about 0.1% of water parcels originate from interhemispheric pathways. For the NPMW, the longer formation pathways are distributed along the length of the Antarctic Circumpolar Current (ACC) in the Southern Ocean (between 50°S and 40°S). Water parcels originating here subduct near the ACC, cross the equator, and eventually reach the subtropical North Pacific. ISAMW also has a very small contribution of water from the North Pacific that originate in the subtropical gyre central within the Sea of Okhotsk. This pathway is likely due to the formation of North Pacific Intermediate Water (which has the same density as ISAWM in the model) which is slowly transported southward. Both NPMW and ISAMW also show some parcels originating in the North Atlantic off the tip of Greenland indicating a contribution from North Atlantic Deep Water.

Together V_f and $\Gamma^\dagger$ also provide information as to whether a water mass has multiple formation regions. In the North Pacific, a single patch with low $\Gamma^\dagger$ is located in the center of the basin around 180°E (Figure 5.4a). For ISAMW, the Indian Ocean contains two nearby, but separate patches of $\Gamma^\dagger$ around 2 years (Figure 5.4b), one south of Australia (around 45°S and 120°E) and the other near the western edge of the gyre (40°S and 80°E). The separation of these two $\Gamma^\dagger$ minima along with high volume fraction in each region suggests that there are at least two primary formation regions of ISAMW. The more complicated ventilation of ISAMW compared to NPMW can be seen by comparing V_f and Γ (Figure 5.5). Whereas NPMW has a relatively strong correlation between $\Gamma^\dagger$ and V_f (Figure 5.5a), ISAMW shows at least three different regions where V_f is high, but separate ages of 2, 3, and 4 years (Figure 5.5b).

Within the main formation regions, $G^\dagger$ has a strong seasonal cycle (demonstrated for the points with the largest V_f in Figure 5.6), consistent with the idea that permanent subduction only occurs in the late winter over a time span of about a month (Stommel, 1979). For the grid point 34.5°N, 170.5°W which has the largest NPMW V_f, the annual maximum of $G^\dagger$ occurs in mid-winter in February (Figure 5.6a). For the maximum V_f point of ISAMW (35.5°S and 92.5°E), the peak of $G\dagger$ occurs in July near the end of austral winter (Figure 5.6b).

In both the NPMW and ISAMW, the width of these peaks is about two months suggesting that only the water from the time of the densest mixed layers experiences permanent subduction. Because in between these peaks the TTDs are essentially 0, only changes of a tracer during the winter months will propagate into the interior. While the magnitude of the annual maxima exponentially decays for the NPMW adjoint TTD, the ISAMW adjoint TTD's decay rate is not constant. This could arise if multiple transport pathways exist between that surface grid point and the ISAMW (Figure 5.5b).

The Peclet number ($\Gamma^{\dagger 2}/\Delta^{\dagger 2}$, see (5.10) and (5.12) for the calculation of each parameter),

shows that the ventilation pathways for ISAMW and NPMW are advectively dominated ($Pe > 1$) except in the regions with high V_f (Figure 5.7). Here we discuss three reasons why these relatively young TTDs also have a high Pe. We first note that Pe is intended to represent the local dominance of advective versus diffusive transport. Thus, trying to ascribe a Peclet number over the entire path of a water parcel may be ill-defined if the pathway is very long. Second, high Pe flows can be approximated by a system where changes can only flow downstream with no feedback between a downstream location and any point upstream. In the regions of high V_f, the seasonal cycle in mixed layer depth is also large resulting in entrainment during the winter seasons and detrainment during the summer seasons. This seasonal switch between 'upstream' and 'downstream' directions may have an effect equivalent to strong 'mixing.' Third, the 1d TTD model neglects the effect of diapycnal mixing which can be significant for surface points which detrain or entrain water into the mixed layer.

5.5 Interannual variability

We next investigate variability in the formation of NPMW and ISAMW by using $G^\dagger$ calculated with interannually varying transports. We first visually compare the time-varying $G^\dagger$ to the climatological $G^\dagger$. Next, we use the estimates of $\Gamma^\dagger$ and $\Delta^\dagger$ from the climatological adjoint TTDs to understand how the variability caused by climate modes can be transformed by the effects of oceanic ventilation. The variability of V_f and $\Gamma^\dagger$ is then calculated from the 20-year integrated adjoint TTDs which were initiated each year from 1967 to 2009, to better understand how the formation of NPMW and ISAMW varies interannually.

5.5.1 Interannual variations in $G^\dagger$

To compare the interannually-varying TTDs to the climatological ones, the adjoint TTDs are integrated over the entire surface. This is mathematically equivalent to performing a

forward TTD run initialized over the entire surface, but for consistency with the rest of the results presented in this study we use $G^{\dagger}$.

Integrating over all the hindcast $G^{\dagger}$ (blue lines in Figure 5.8) for NPMW (Figure 5.8a) and ISAMW (Figure 5.8b) yields TTDs that are similar to the corresponding climatological TTD (black lines in Figure 5.8). However, the hindcast TTDs for both NPMW and ISAMW in any given year differ significantly from their climatological TTDs (compare Figure 5.8 to Figure 5.6).

For ISAMW, the annual peak of the distribution from year to year does not occur consistently in August as for the climatological TTD, but can also occur in June or July. The magnitude of the hindcast TTDs (i.e. the amount of ISAMW formed at any given time) also varies in strength compared to the climatological TTD (compare the colored dots to the solid black line in Figure 5.8a). The difference in the timing of the TTD's annual maximum along with the variability of magnitude of the maximum may reflect changes either in total ISAMW formation or a shift in the strength of formation between the two regions discussed in Figure 5.4a.

The NPMW interannual TTDs primarily differ only slightly from the climatological TTDs (Figure 5.6b). The TTDs in 35 of the 43 years place the annual peak of the TTD in the same month as the climatological TTD (February). The variability in magnitude does change interannually and corresponds to a weakening or strenghthening of NPMW formation in that year.

5.5.2 Propagating climate mode variability into the interior

Using the interpretation of the TTD as a 'filter' of surface variability discussed in Section 5.3, we next show how the variability of a tracer in the interior, $C(\vec{x}, t)$, with known boundary condition, $R(t)$, is modified differently by climatological versus interannually-varying ventilation. We first assume that R is spatially homogeneous (i.e. $R(\vec{s}, t) = R(t)$) and represents

a passive tracer whose boundary condition is perfectly correlated to the SAM index or the PDO index.

As was discussed in Section 5.4, the mode waters are only sensitive to variability of a tracer in the winter months when the TTDs are non-zero. Because of this, annual values of the PDO and SAM indices are calculated by averaging over the value of each index in January, February, and March for the PDO and July, August, and September for SAM. These wintertime indices for PDO and SAM are referred to as R_{PDO} and R_{SAM} respectively. The result of convolving the PDO tracer with either the surface-integrated climatological TTDs (with $\Gamma^{\dagger} = 4.7$yrs for ISAMW and 3.3 yrs for NPMW) or with the interannually varying TTDs will be referred to as C^{clim}_{PDO} or C^{hind}_{PDO} respectively. Similarly, the interior variability of the SAM tracer will be referred to as C^{clim}_{SAM} or C^{hind}_{SAM}.

The low-pass nature of the IG filter means that differences between C and R in (5.2) will depend on how much of the variance in R is contained in the higher frequencies. At frequencies less than the corner frequency f^*, given in (5.15), the power spectra of C and R will remain coherent, but at high frequencies the spectra will diverge. Because subduction primarily happens in the wintertime, mode water formation places an upper bound on the highest observable frequency of oscillation (i.e. the Nyquist frequency) of 2 years. The cumulative integral of the estimated power spectra (Welch, 1967) of C and R can also be used to understand how the filtering changes the distribution of spectral variance by frequency.

For both the PDO and SAM, C^{clim}_{PDO} and C^{clim}_{SAM} have a redder spectrum compared to their respective R (Figures 5.9 a and b) and also have reduced total variance when integrated over the entire spectrum (Figures 5.9 c and d). The spectrum of R_{PDO} already has a strong, negative spectral slope (Figure 5.9a) with a rolloff around 0.05 (yr^{-1}) and with 50% of the variance contained within the 0-0.1 yr^{-1} frequency range (Figure 5.9c). The power spectrum of C^{clim}_{PDO} has a slightly steeper spectral slope (about 5%) than that of the PDO index, but retains many of the same features seen in the R_{PDO} spectrum. This additional reddening

however does lead to a loss of about 40% of the variance due to the effects of advection and mixing.

The SAM index has a power spectrum that is relatively flat because SAM has variability which is distributed across a range of frequencies (Figure 5.9b). After the IG TTD is applied, C^{clim}_{SAM} has a similar spectrum to R_{SAM} until about 0.1 yr^{-1} when the C^{clim}_{SAM} spectrum begins to redden sharply. This is in contrast to the power spectra of R_{SAM} which has a slight positive spectral slope around this same frequency. The lack of coherence between these two spectra particularly at high frequencies leads to an overall decrease of about 60% in the total variance (Figure 5.9d).

We next compare C and R in the time domain to understand how the reddening of the spectrum and loss of variance affects the correlation of the two time series. The IG phase response is nonzero, so C may be lagged relative to R, however we also note that the nonlinearity of the phase response may further reduce correlations.

For the NPMW, the C^{clim}_{PDO} (Figure 5.10a) shows that the PDO tracer is only slightly modified by the IG filter ($\Gamma = 3.3$ yrs $\Delta = 2.5$ yrs). C^{clim}_{PDO} has a maximum correlation at 1-year lag and explains about 76% of the variance of the PDO index. The high correlations relative to the ISAMW and SAM result from both the spectrum of the PDO containing comparatively little energy at high-frequencies and the lower Γ of NPMW. When interannually varying TTDs are considered (red line Figure 5.10a), the correlation C^{hind}_{PDO} to the PDO is only slightly lower and explains 69% of the variance. This relatively small reduction in variance due to changing ventilation as compared to C^{clim}_{PDO} likely arises from the fact that the PDO, by construction, is a mode of oceanic surface variability. Any changes at the surface related to the PDO may directly affect the TTDs as well.

C^{clim}_{SAM} shows similar patterns of temporal variability as the SAM index (Figure 5.10b). C^{clim}_{SAM} remains significantly correlated ($p < 0.1$) with SAM, however C^{clim}_{SAM} lags SAM by one year. The amplitude of is also significantly reduced. The attenuation of high frequency

variability means that some of the high amplitude SAM events (e.g. 1973, 1979, 1985, and 1993) still show up as peaks in C_{SAM}^{clim}, but their magnitude is greatly reduced (by a factor of 2.5, 4.6, 1.7, and 1.7). The 1979 event is the strongest positive event in the SAM record, but barely registers as an anomaly in the interior because of the weak or negative events between 1975 to 1979. The longterm trend in SAM (blue dashed line) and the trend in C_{SAM}^{clim} are statistically indistinguishable ($p < 0.1$) because in Fourier space, trends can be thought of as low-frequency modes of variability which are not attenuated by the IG filter.

When the interannually varying TTDs are used (red line Figure 5.10b), C_{SAM}^{hind} is significantly correlated ($p < 0.1$) to the SAM index. The filtering still has a maximum lag at one year, but in this case only 29% of the variance in the SAM index is explained by C_{SAM}^{hind}. The reduction in variance explained arises from the fact that SAM is an atmospheric mode of variability that, while being well-correlated with many mixed layer properties, can only indirectly cause changes in oceanic circulation by changing the wind forcing. The strong positive 1979 anomaly in SAM appears as a weak negative anomaly in the interior. The high frequency variability in SAM is even further reduced and instead C_{SAM}^{hind} is dominated by a low frequency 15-year oscillation in SAM along with a trend in time.

5.5.3 Formation region variability from adjoint TTDs

The analysis performed above implicitly assumes that the surface variability does not affect subduction and circulation. To determine the effects of SAM and PDO on modifying the strength of subduction and gyre circulation, we compute a number of metrics based on V_f calculated from both the climatological and interannually varying adjoint TTDs. The centroid of the formation region ($\bar{V}_f$) is calculated as a geographic mean weighted by V_f of the hindcast TTDs given by

$$\bar{V}_f(t) = \int_S V_f(\vec{x}, t)\vec{s}d\vec{x} \tag{5.17}$$

where S indicates the surface mixed layer. An empirical orthogonal function analysis (EOF) is also applied to the V_f maps to identify the large-scale modes of variability. The principle components of each of the first modes of these EOFs are then correlated to the PDO (for NPMW) and SAM (for ISAMW).

The NPMW $\bar{V}_f$ shows that the center of the formation region has both significant meridional and zonal variation between 1967 and 2009 (Figure 5.12a). At the beginning of the hindcast period, the centroid begins slightly northwest of the climatological position (35.5°N, 175°W). Between 1967-1976, the centroid moves east and slightly to the south until 1977, when it shifts southward (coincident with the 'regime shift' in the PDO). The first EOF of V_f (Figure 5.12b) contains about 55% of the variance and shows a meridional oscillation with a node at 35°N between 155°W and 185°W, which strengthens mode water formation in the south during its positive phase. This EOF also seems to be consistent with the PDO; when the PDO is in a positive phase, negative temperature anomalies are present in the central North Pacific, which shifts NPMW isopycnal outcrops southward. Both the temporal variability of the meridional changes in the centroid and the principle component of the V_f EOF (Figure 5.12c) are significantly correlated with the PDO ($p < 0.1$).

Both $\bar{V}_f$ and the first EOF of V_f show that the formation region of ISAMW has little meridional variation, but significant zonal variation (Figures 5.11 a and b). The climatological V_f centroid is located at 37.1°S±0.4°, 86.4°E±1.5°. The interannually varying centroid oscillates around this location with a zonal amplitude of about 2.8°E (243km) with an approximate period of about 20 years (Figure 5.11a). The first EOF (which contains 43% of the variance) also diagnoses a spatial pattern which varies primarily zonally in time (Figure 5.11b). The EOF has a node at 90°E with a strengthening in the amount of ISAMW formed between 90°E and 105°E and a weakening between 60°E and 90°E during positive phases of this EOF. The insignificant correlations ($p > 0.1$) of both the principle component of this EOF (Figure 5.11c) and the zonal part of $\bar{V}_f$ with the SAM index, suggest that SAM does

not directly control anomalies in ISAMW formation.

5.6 Summary and discussion

Here we used the adjoint transit time distribution (TTD) framework to infer the mean state and variability of the formation regions and ventilation timescales of North Pacific Mode Water (NPMW) and Indian Ocean Subantarctic Mode Water (ISAMW). A Fourier analysis was applied to the analytic, Green's function solution of the 1d advection-diffusion equation (which takes the form of the two-parameter inverse Gaussian distribution) to show how mixing causes high frequency variability at the surface to be attenuated by the effects of oceanic transport.

While 1d TTDs have been extensively used in the literature to identify the timescales of oceanic ventilation, the estimate of mean age (Γ) and shape parameter (Δ) can also be used to determine what timescales of variability at the surface may directly affect the thermocline. Assuming a fixed ratio $\Delta/\Gamma = \alpha$ allows the 1d TTD to be inferred from a single tracer like CFC-11, CFC-12, or SF_6. In this case (5.15) simplifies to

$$f^*(\Gamma) = \frac{\sqrt{\log(2)}\sqrt{\alpha^2\log(2)+1}\,(\alpha^2\log(4)+1)}{\alpha\Gamma} \tag{5.18}$$

and the frequency-dependent phase response to

$$\phi(f) = \left(\frac{\sqrt{\sqrt{16\alpha^4\Gamma^2 f^2+1}-1}}{2\sqrt{2}\alpha^2}\right). \tag{5.19}$$

These formulae could be applied to mapped estimates of tracer-inferred age from observations to estimate which natural modes of surface variability might affect the thermocline.

To calculate the 3d, model adjoint TTDs, 1000-year integrations of the offline model were performed where grid points corresponding to NPMW or ISAMW (chosen using potential

vorticity and density criteria) were initialized with a passive tracer. The volume fraction V_f of water that formed at each surface point was calculated by integrating the flux through each grid point over the 1000 year integrations. V_f then allowed for the specific identification of formation regions of NPMW and ISAMW. $\Gamma^\dagger$ and $\Delta^\dagger$ were also calculated from these adjoint TTDs. The ventilation pathways connecting the high V_f regions with the mode water were often diffusively dominated due to the reentrainment of the water from year to year.

The adjoint TTDs displayed a strong seasonal cycle; the adjoint TTD tracer fluxed into the surface only during the winter months (January, February, and March in the Northern Hemisphere and June, July, and August in the Southern Hemisphere) when subduction of NPMW and ISAMW occurred. Thus for waters that are formed primarily by subduction, the current IG model should be modified to include this seasonality by setting the summer months of the IG to 0 when iferring ages from observations or using TTDs to infer anthropogenic carbon dioxide inventories. Future work could examine how sensitive current estimates of ventilation age and TTD-inferred anthropogenic carbon (e.g. Khatiwala et al. (2009)) are to this modified IG.

We relaxed the assumption of cyclostationary transport used in previous studies by performing adjoint runs where separate runs were performed for each year between 1967-2009 and integrated using the interannually varying transports for 20 years. The interannually varying maps of V_f for both ISAMW and NPMW were then used to calculate the centroid of the formation region (i.e. the geographic average weighted by V_f) and used to perform an empirical orthogonal function analysis.

Both the climatological and hindcast TTDs for NPMW and ISAMW were applied to tracers whose surface boundary was either the index of Pacific Decadal Oscillation (PDO) for NPMW or the index of the the Southern Annular Mode (SAM) to generate time series of the tracer within the interior. Because most of the variability of the PDO occurs at low frequencies, we found that the interior time series of the PDO tracer remained strongly

correlated to the PDO index. In contrast, the SAM tracer was also correlated, but much of the high-frequency variance was 'filtered' away by the effects of advection-diffusion.

While all these metrics showed that NPMW was significantly correlated to the PDO, the SAM was not correlated with ISAMW. This finding may relate to the fact that the PDO, by construction, is intended to capture SST variability (and thus also other oceanic surface changes) whereas SAM is an atmospheric mode of variability. While SST, mixed layer depth, and surface heat fluxes have been shown to be correlated with SAM, their regressions with the SAM index are not as strong as PDO and SST (Lovenduski, 2005; Sallée et al., 2010).

The lack of a relationship between SAM and ISAMW is also consistent with recent observational studies which show that at best the trend towards positive SAM may cause persistent changes in the large-scale dynamics, but otherwise is largely uncorrelated with the Southern Ocean thermocline. A number of recent studies have found the location of the Subantarctic Front (north of which deep mixed layers form) does not vary in response to SAM (Graham et al., 2012; Gille, 2014; Shao et al., 2015). Additionally, Ayers and Strutton (2013) found little evidence that nutrient delivery to ISAMW was correlated to changes in wind stress curl over the ISAMW formation region.

The adjoint TTD method used here provides an alternative to particle bactracking in identifying the sources of waters in ocean models. We have shown too that interannually varying TTDs can be used to infer how ventilation of specific water masses can vary interannually. Plans to incorporate offline adjoint functionality into other GCMs will allow similar analysis to be performed for long integrations of coupled, atmosphere-ocean simulations which can be used to understand how multidecadal variability in climate modes may project onto the oceanic interior.

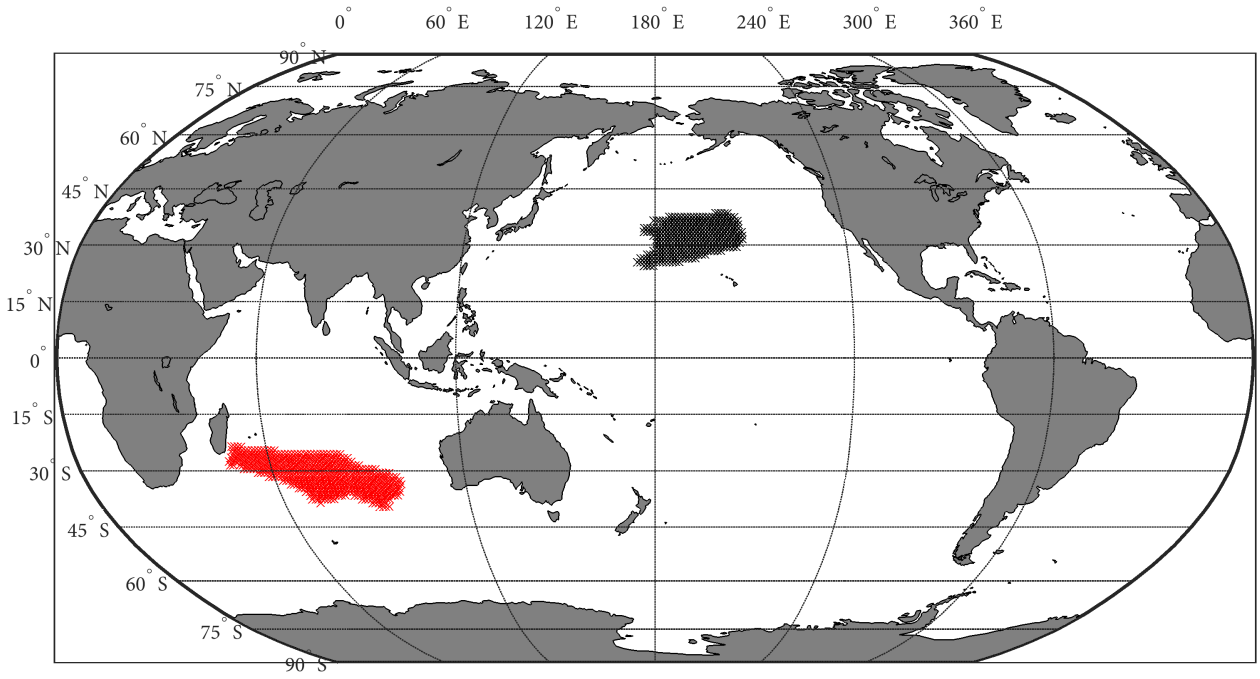

Figure 5.1: The locations of the grid points used to initialize the adjoint transit time distributions (TTDs) for the North Pacific Mode Water (NPMW, black) and Indian Ocean Subantarctic Mode Water (ISAMW, red). See text for the potential vorticity and density criteria used for each water mass.

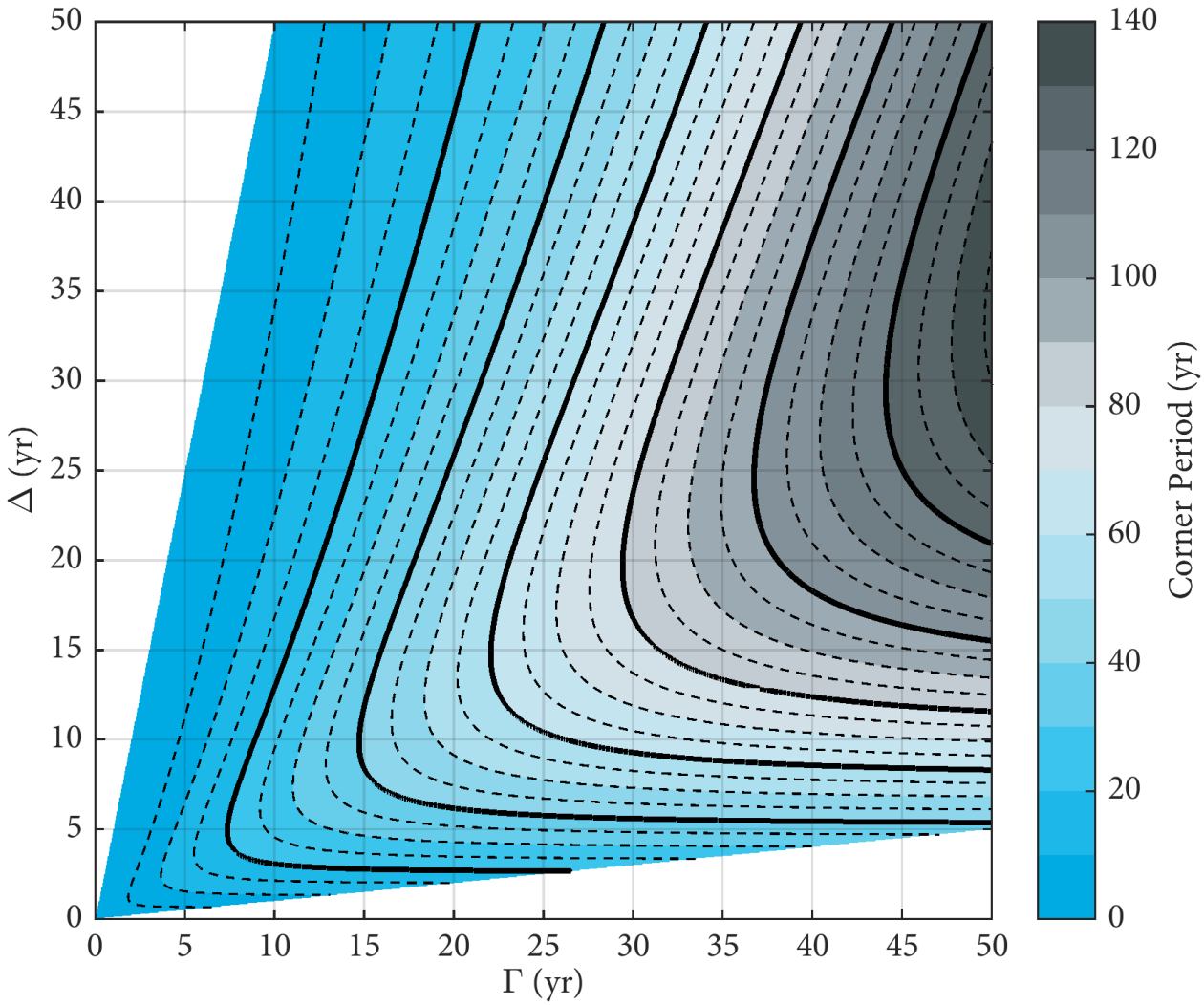

Figure 5.2: The corner period of an Inverse Gaussian (IG) 'filter' as a function of mean age Γ and width parameter Δ (see text for derivation). For interior water parcels whose TTD is described by an IG, the corner period describes the shortest period of variability of a time-varying surface boundary condition that could be measured in the interior. The dashed contour interval is 5 years and the bold contour interval is 20 years.

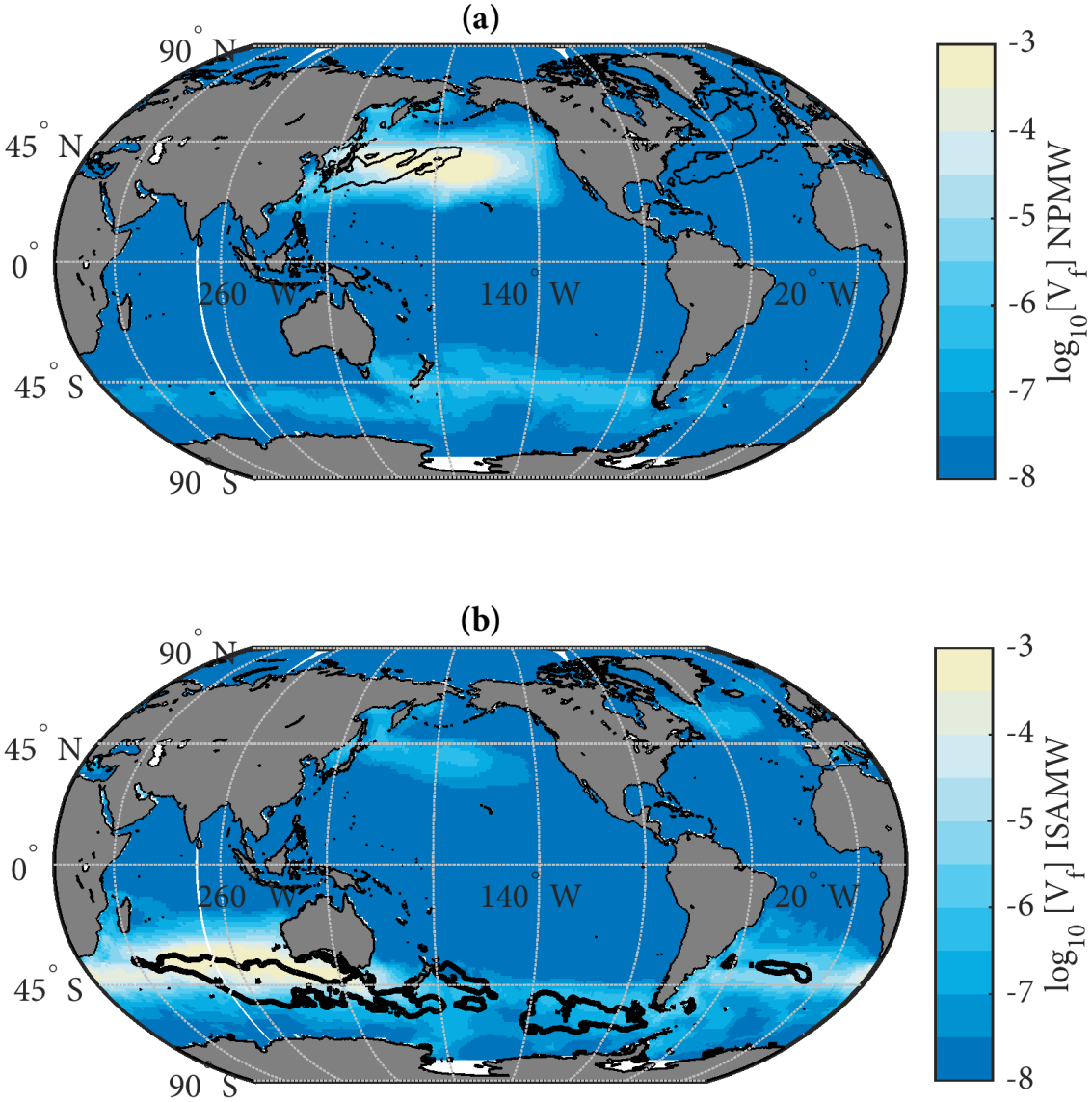

Figure 5.3: The fraction of the total volume (V_f) of (a) NPMW and (b) ISAMW that originated at each surface grid point using adjoint TTDs based on climatological transports. V_f is shown on a $\log_{10}$ scale to distinguish the small ($< 0.001\%$) contributions from other ocean basins. Black contours indicate regions where wintertime mixed layer depths exceed 150m for NPMW and 200m for ISAMW.

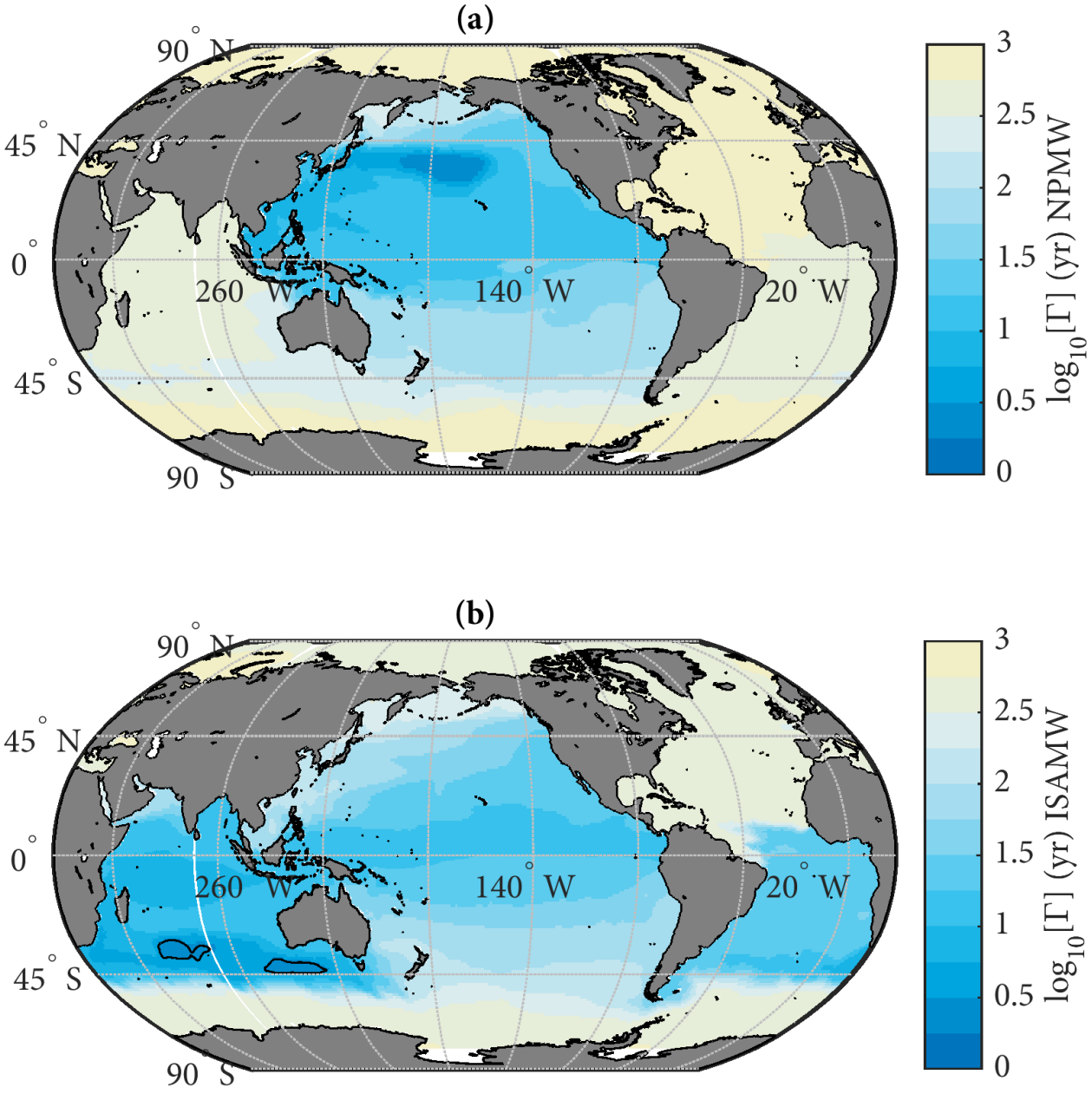

Figure 5.4: Mean age ($\Gamma^\dagger$) of the adjoint TTDs for (a) NPMW and (b) ISAMW. Color is on a $\log_{10}$ scale to capture both the very short intra-basin timescales and transport from more remote locations.

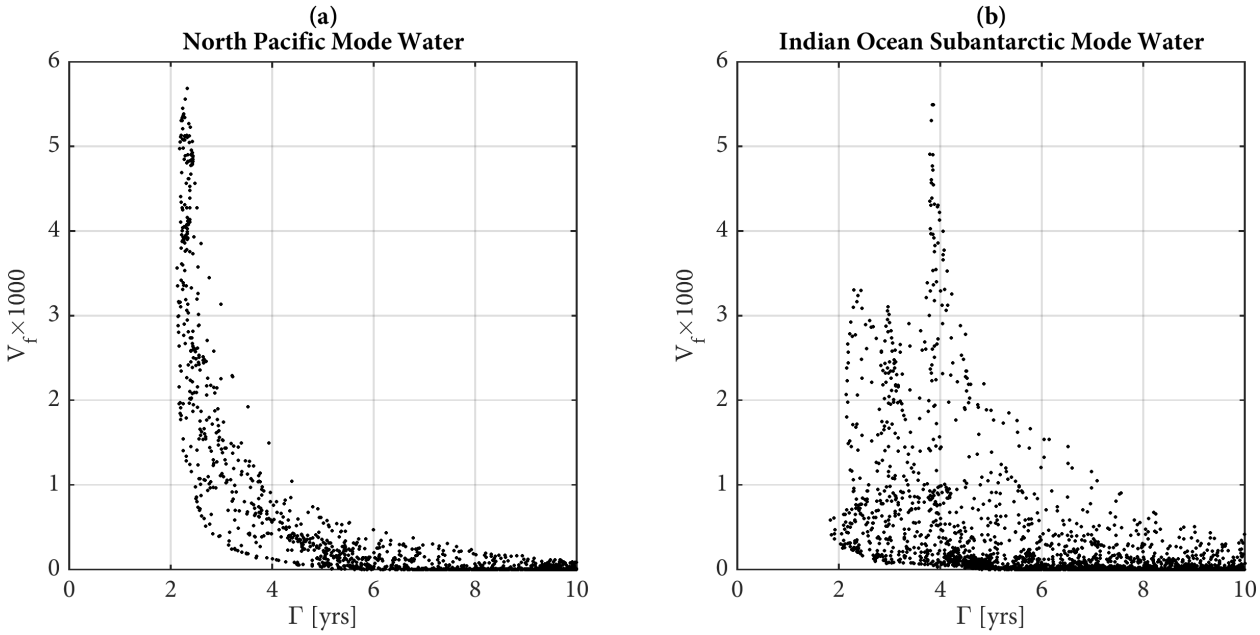

Figure 5.5: The relationship between $\Gamma^{\dagger}$ versus V_f, for all surface grid points, calculated from the climatological adjoint TTDs for (a) NPMW and (b) ISAMW. Large values of V_f that are clustered around similar values of $\Gamma^{\dagger}$ are associated with a unique formation region of mode water.

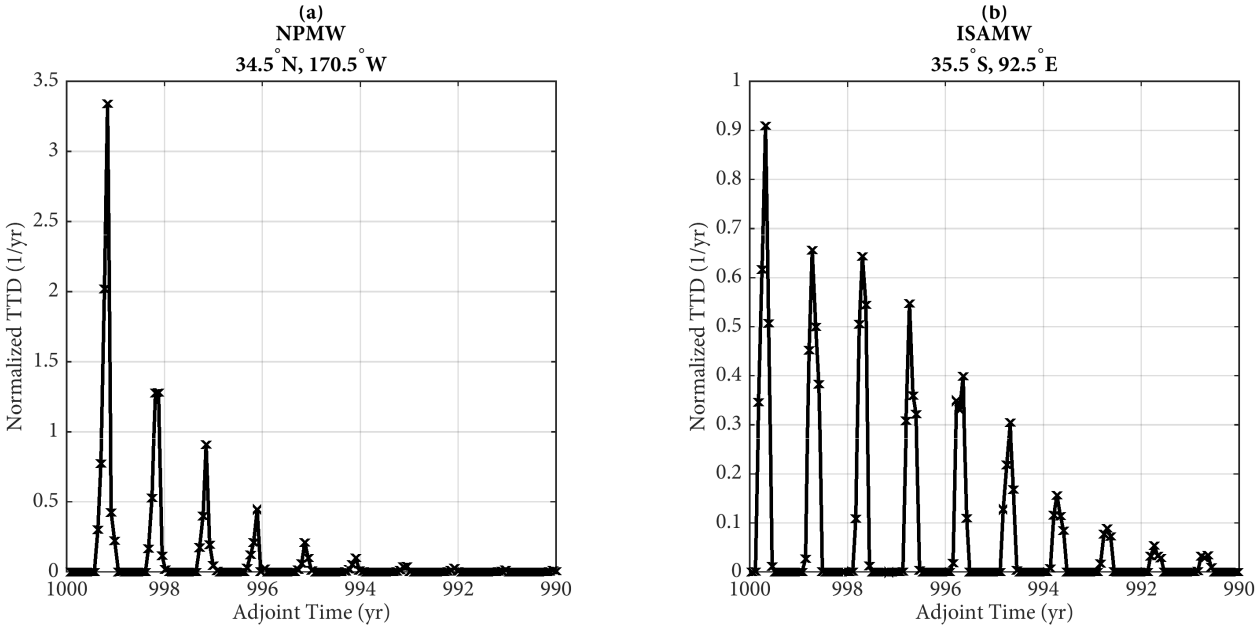

Figure 5.6: Adjoint TTDs at the surface grid point which has the maximum V_f for (a) NPMW and (b) ISAMW where 'x' indicates the magnitude of the TTD every 25 days. Note that the time axis is reversed because the adjoint equation is integrated backwards in time starting at 1000 years.

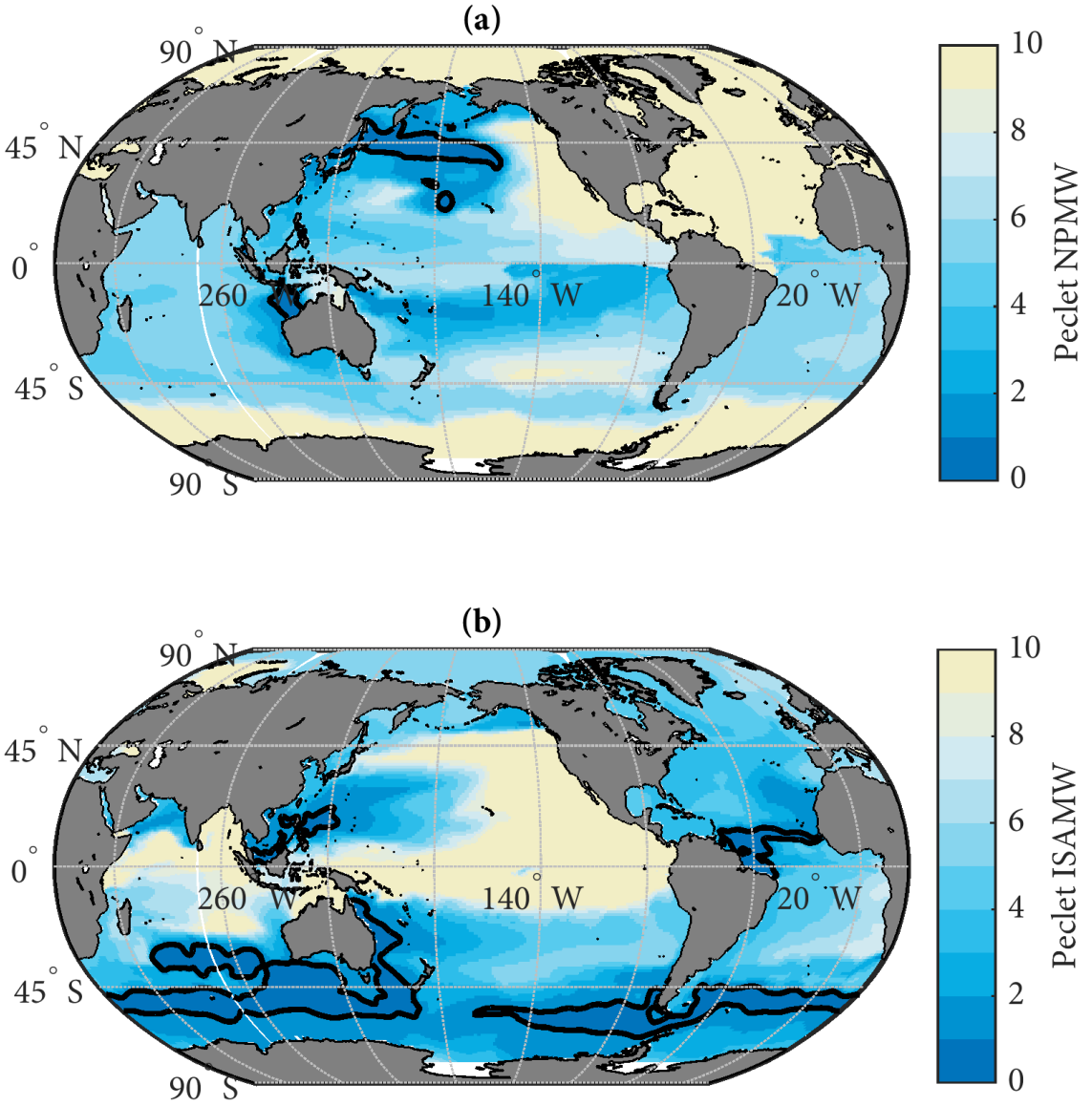

Figure 5.7: Peclet number ($\Gamma^{\dagger 2}/\Delta^{\dagger 2}$) where $\Delta^{\dagger}$ is estimated from the adjoint TTD using a maximum likelihood estimator. Peclet values below 1 (black contour) would in principle indicate regions where diffusive transport dominates, but there can be exceptions (see text for details).

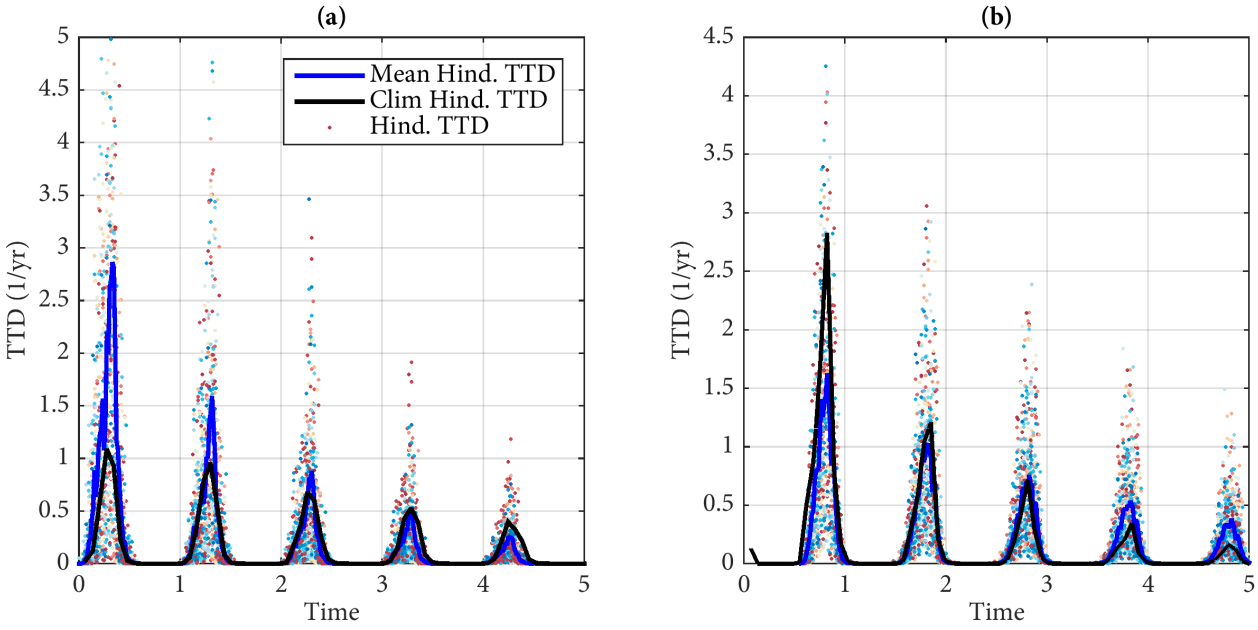

Figure 5.8: Comparison of multiple instances of the TTDs connecting the surface to (a) NPMW and (b) ISAMW calculated using hindcast transports (each year represent by the same colored dots), the multi-year average of these hindcast TTDs (blue line), and climatological TTDs (black line). These TTDs are calculated by integrating the adjoint TTDs over the entire surface of the ocean.

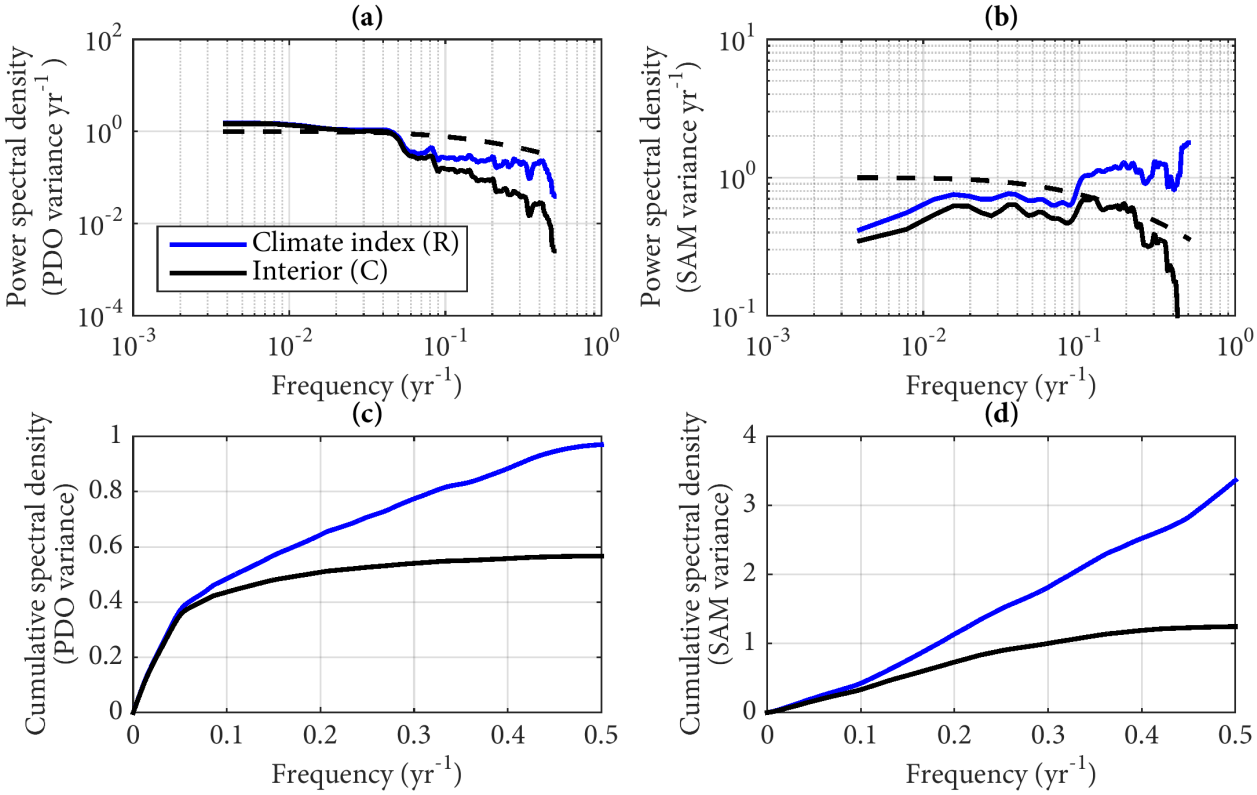

Figure 5.9: Comparisons of the (a, b) power spectra and (c, d) the cumulative spectra for the (a, c) PDO and (b, d) SAM for the climate index (blue lines) and the interior variability of a hypothetical tracer (black lines) that was propagated into the interior using climatological TTDs. The (a, b) power spectra are estimated by applying Welch's method (Welch, 1967) to the timeseries of the indices for each climate mode. The (c, d) cumulative spectra are the cumulative integral of (a, b) and represent the accumulated variance as a function of frequency. Dashed lines in (a) and (b) indicate the attenuation by frequency of the IG filter.

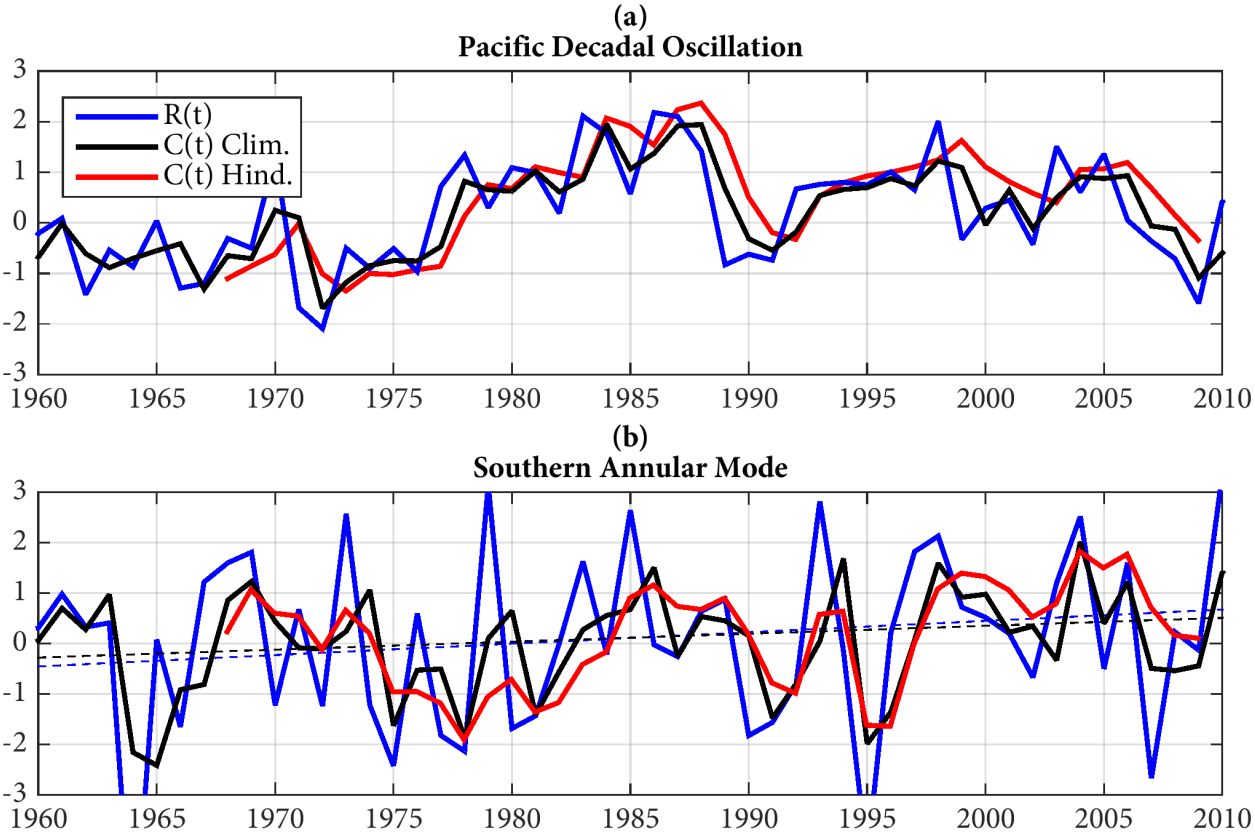

Figure 5.10: Comparisons of the (a) Pacific Decadal Oscillation (PDO) and (b) Southern Annular Mode (SAM) indices (blue lines, referred to as $R(t)$ in the text) with those modified by oceanic transport assuming the IG climatological (black lines) and 3d, hindcast (red lines) TTDs (referred to $C(t)$ in the text). Only the average of the index of the winter months are shown to correspond with the months of mode water formation (January, February, and March for the PDO and June, July, and August for SAM). The trends in SAM of the original index (black) and in the interior (blue) are shown as dashed lines in (b).

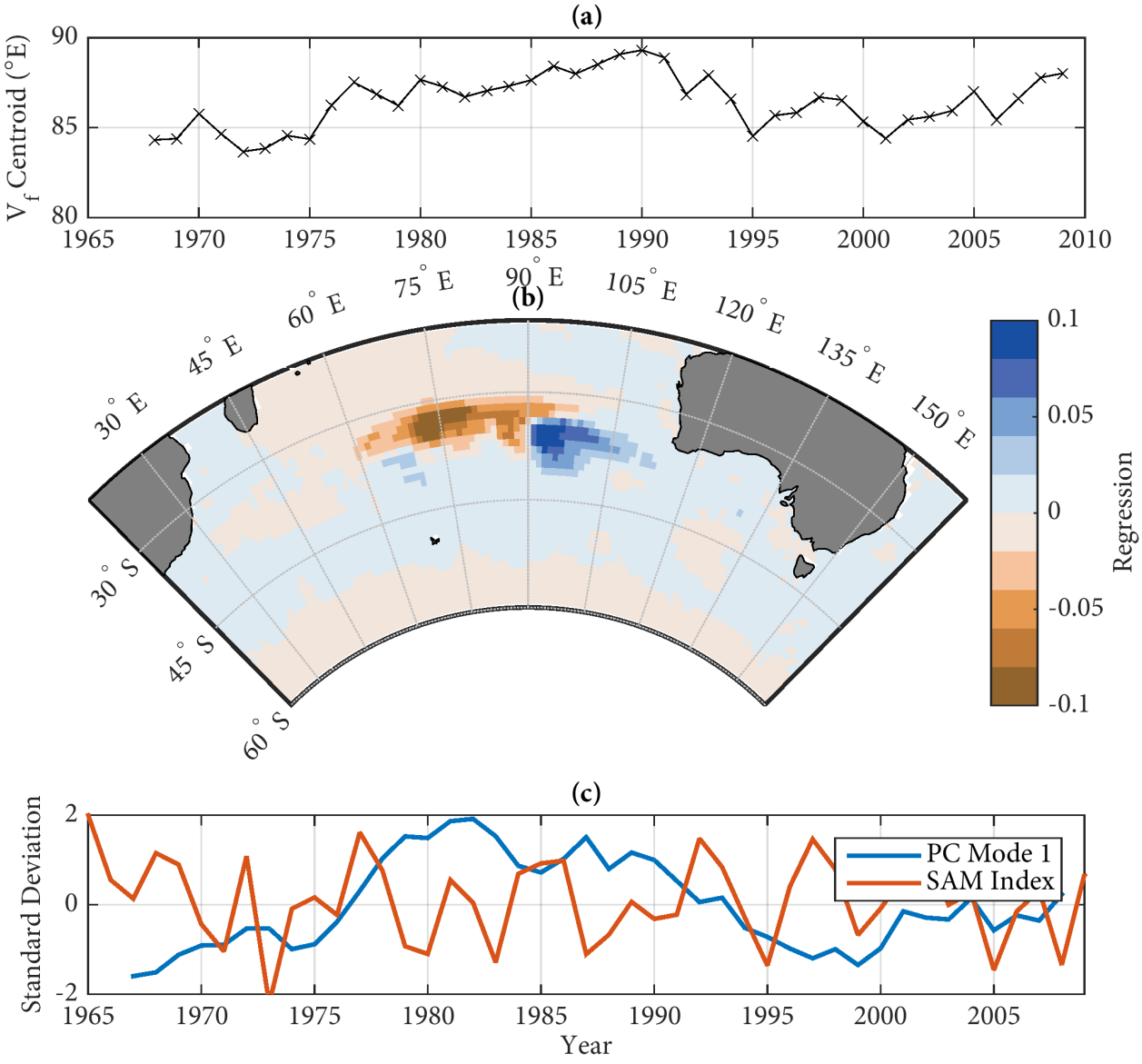

Figure 5.11: Changes in formation region calculated as (a) the zonal variation of the center of the formation region of ISAMW ($\bar{V}_f$), (b) the first empirical orthogonal function (EOF) of V_f, and (c) the principle component associated with the EOF compared to the austral winter SAM index. The V_f used for these plots is calculated from the interannually varying adjoint TTDs that were initiated between 1967-2009 within ISAMW.

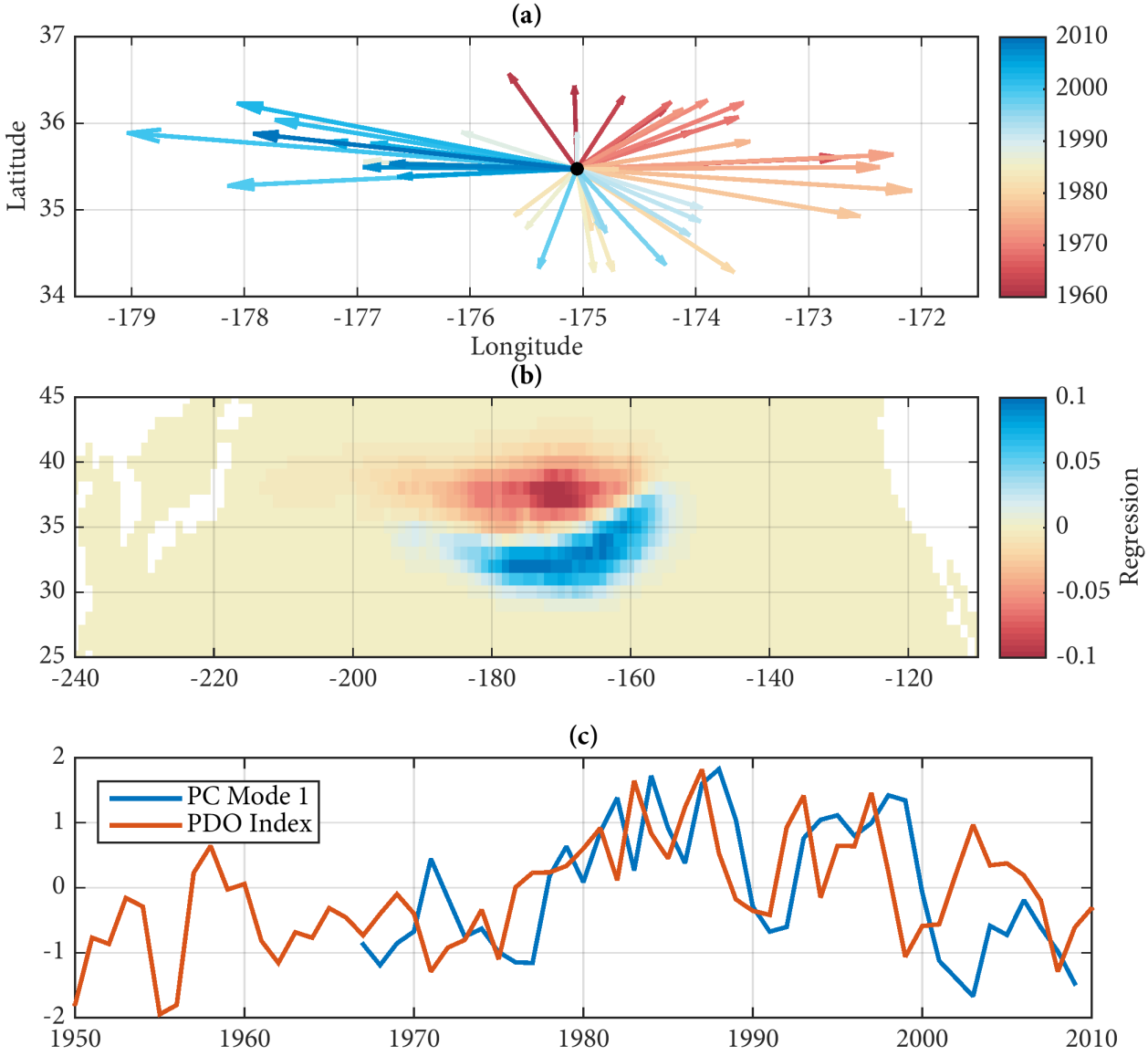

Figure 5.12: Similar to Figure 5.11 but for V_f calculated from the adjoint TTDs of NPMW where (a) is a hodograph of the position of $\bar{V}_f$ colored by year, (b) is the EOF of V_f, and (c) is the principle component (red line) of the EOF and the wintertime PDO index.

Chapter 6
SUMMARY AND FUTURE WORK

The previous four chapters of this thesis have shed insight into how the ocean interior responds to changes at the surface using a combination of tracer modeling and satellite observations. Here the main results of Chapters 2 to 5 are summarized. The broader implications on the use of tracers to infer both the mean state and variability of thermocline ventilation are discussed.

6.1 Main results

In Chapter 2, an offline tracer model (Offtrac) to the Hallberg Isopycnal Model (HIM) and a simple 1-dimensional gas exchange model was used to estimate the time-varying mixed layer saturation of sulfur hexafluoride (SF_6) and chlorofluorocarbons (CFCs) 11 and 12. A strong seasonal cycle in undersaturation was evident for each tracer with the largest undersaturations occuring in mid-winter and saturation in the summer months (and occasionally supersaturation). This seasonal variability was largely attributed to the effect of entrainment of tracer-poor waters during mixed layer deepening in the winter and also seasonality in the solubility of each gases. Wintertime undersaturations were largest near the beginning of the records when the tracers were first released into the atmosphere and then decreased largely monotonically.

In Chapter 3, the skewness of sea level anomaly measured from satellite altimeters was used to identify strong frontal features in the Antarctic Circumpolar Current. A meandering Gaussian jet model was combined with a Monte-Carlo simulation to estimate the mean position and meander window of the Subantarctic Front and Polar Front. Topography was

speculated to be a strong constraint on the path of these fronts. Using annual subsets of the altimetry record from 1993 to 2014, the mean position of these fronts had significant variability especially downstream of topographic features basins. However, this variability was largely uncorrelated with changes in the large-scale wind field and the Southern Annular Mode (SAM).

In Chapter 4, the 3-dimensional transit time distributions (TTDs) using a boundary impulse response method (TTD-BIRs), ideal age, CFCs, SF_6, and oxygen were calculated using Offtrac. By computing inverse Gaussian (IG) approximations to the TTD-BIR using a maximum likelihood estimator approach (IG-MLE), we found that oceanic ventilation could be reasonably approximated by a simple 1d model of ventilation for an isopycnal containing the mode water in the thermocline of the North Pacific subtropical gyre and near the formation region of the South Pacific Antarctic Intermediate Waters (AAIW). IGs inferred using modeled CFC-12 and SF_6 were generally dissimilar to the IG-MLE suggesting that this tracer pair did not form strongly independent constraints on oceanic ventilation. The Peclet number of these dual-tracer inferred TTDs were biased low relative to those of the IG-MLE, indicating that these tracers might overestimate the magnitude of diffusive transport relative to advective transport. Apparent oxygen utilization (AOU) and mean ages of TTDs inferred using CFC-12 assuming fixed Peclet numbers IGs and TTDs whose parameters are constrained by both CFC-12 and SF_6 were found to be broadly well-correlated ($p < 0.1$) to variability in ideal age in most of the thermocline. However, TTD mean ages showed significant anti-correlations (i.e. diagnosing the opposite change in ventilation) in the South Pacific AAIW. If changes in AOU and either the single or dual-tracer TTD mean ages agreed in sign, the possibility of a 'false' change in ventilation could be avoided.

In Chapter 5, adjoint TTDs were calculated using an adjoint configuration of Offtrac to identify the formation regions of North Pacific Mode Water (NPMW) and Indian Ocean Subantarctic Mode Water (ISAMW). Climatological TTDs showed that NPMW was primarily

formed in the central basin, likely via lateral induction. ISAMW had two distinct formation regions in the central and eastern South Indian Ocean. Variability in NPMW formation was linked to the southward shift of isopycnals related to the Pacific Decadal Oscillation. The variability of ISAMW formation, however, was uncorrelated to SAM and instead exhibited a slow mode of variability dominated by a roughly 30-year oscillation. A Fourier analysis of the 1d TTD showed that a surface boundary condition is significantly modified by advection and diffusion. The interior variability of a tracer is a result of a low-pass filtering of its boundary condition by the TTD. Analytic forms for both the corner frequency and the phase response of the filter were also presented.

6.2 Implications of research

The results of this dissertation serve to further emphasize the role of tracers as an effective way to infer changes in ventilation. In the particular cases of CFC-11 and CFC-12, their decreasing atmospheric concentrations since the early 1990s have hampered their ability to robustly infer changes in ventilation age within the thermocline. However, assuming that the Peclet number was fixed, we found that TTDs inferred using SF_6 or CFC-12 had comparable skill at tracking changes in ventilation. As observations of SF_6 are now routinely being measured along with CFCs on the repeat hydrography cruises by Global Ocean Ship-Based Hydrographic Investigations Programme (GO-SHIP), mean ages inferred using SF_6 may provide a way to continue tracking decadal changes in thermocline ventilation if there was an occupation of that hydrographic section in the late 1990s or early 2000s that measured both CFC-12 and SF_6.

The recommendation to use two tracer methods to validate a change in ventilation is further strengthened when applied to the context of decadal repeat hydrography. The variability of apparent oxygen utilization (AOU) and CFC-12 and/or SF_6 inferred ages were significantly correlated with ideal age at the $p < 0.1$ level when the tracers were sampled an-

nually. In the roughly thirty years since the World Ocean Circulation Experiment (WOCE), many of the original lines have had only two or three occupations. For three samples, the equivalent correlation value at the $p < 0.1$ level is about 0.8- a higher value than was calculated in Chapter 4 for AOU or tracer ages in most parts of the thermocline (i.e. the correlation would be insignificant). However, if we make the assumption that tracer ages and AOU add equal degrees of freedom to the problem (i.e. six degrees of freedom over three cruises), the critical value drops to 0.62 which is exceeded in many portions of the thermocline. Thus, statistically robust diagnoses of changes in ventilation are more likely if tracer ages and AOU are used in combination even with relatively sparse sampling in time.

Changes in oxygen (and more specifically AOU) were found to closely reflect changes in age both above and just below the base of the thermocline. While there are a number of regions where the correlations to ideal age variability were insignificant, rarely did they exhibit significant anti-correlations. With the increasing availability of oxygen data collected by some configures of the profiling floats deployed by the International Argo Programme (Körtzinger et al., 2004), this opens up the possibility of inferring interannual changes in ventilation in the upper 2000db of the ocean in regions where temporal variability in oxygen production or consumption is negligible. The efficacy of using the data from these floats necessarily depends on a number of factors that affect the quality of the data including cross-calibration of oxygen across floats and drifts in the oxygen sensors over time. Nevertheless, these oxygen observations combined with continued decadal measurements of CFC-12 and SF_6 through GO-SHIP cruises provide a means to determine both natural variability of and longer terms trends in ventilation associated with climate change.

The Fourier analysis of IG TTDs suggests that the measured variability of a passive tracer at an interior point is a result of significant modification of the tracer's surface variability by the effects of advection and diffusion. The low-pass filtering by the IG, suggests that the high frequency variability of a passive tracer measured in the ocean must be due to some

process other than through a direct connection to changes at the surface. While this analysis has assumed that the IG TTD is constant in time, the non-linear phase response of the filter further suggests that the effects of advection and diffusion mean that the variability of the tracer at the surface will not be linearly correlated to variability in the interior. Allowing the TTD to vary in time likely would cause a further modification of the surface variability. This likely would result in the interior and surface time series of the tracers becoming increasingly uncorrelated.

Connecting interior variability of a tracer to surface variability requires knowing the formation region of that water parcel. For mode waters, this is relatively straightforward as we know that they originate in regions with deep wintertime mixed layers. However, it is difficult to establish, a priori, the origination sites of water masses that experience significant transformation within the oceanic interior (e.g. intermediate or deep waters). Previous modeling studies, targeting the formation of North Pacific Intermediate Water (Kobayashi, 1999) and Antarctic Intermediate Waters (AAIW) (Rimaud et al., 2012), have relied on particle-tracking methods which releases particles in a flow field and track their positions over time. Because these particles are transported via advection, the particles that arrive in the AAIW can then be tagged and their trajectories followed backwards in time. However, by construct, the effects of diffusion must either be treated as either an analogue to advection (i.e. a random walk at each time step) or neglected entirely, neither of which may be satisfactory approximations for some water masses.

The adjoint TTD framework, demonstrated in this dissertation for the mode waters of the North Pacific and South Indian Oceans, provide an alternative method to particle-tracking that can explicitly take into account the effects of mixing. Particularly for general circulation models that have offline transport models, their calculation is no more difficult than solving for forward TTDs. The volume fraction calculated from the adjoint TTDs also can be used to estimate the surface points which have smaller contributions. To demonstrate this, consider

a surface grid point that has a volume fraction of 0.001 for AAIW. For 1000 particles released uniformly over the surface of the ocean, this means that we would expect 1 particle to make it into the interior. However, if only 100 particles were released, that particular surface point may have been assumed to not contribute to AAIW. Adjoint TTD volume fraction, conversely, can be used to calculate the contribution of a surface grid point to the interior to very small values.

The results discussed in Chapter 2, 4, and 5 are based on physical fields derived from a globally configured version of the HIM and tracer fields using Offtrac. In chapter 4, HIM was argued to have fairly good skill at representing processes leading to thermocline ventilation by comparing sections of CFC-12 and salinity. However, our configuration of HIM is a relatively coarse resolution model (nominally 1° in the horizontal) and relies on parameterizations of eddy effects especially their contributions to along-isopycnal and diapycnal mixing. The along-isopycnal transport of tracers due to eddies is parameterized as a spatially homogeneous diffusivity (κ_h set to 1000 m^2 s^{-1} in Offtrac). While this represents a reasonable globally averaged value for κ_h, observationally derived estimates show enhanced eddy fluxes in regions with strong eddy formation (e.g. the Southern Ocean (Gille, 2003) and near western boundary currents (Mecking, 2004)) where κ_h can exceed 10,000 m^2 s^{-1} (Cole et al., 2015). Our value of κ_h is thus lower than the observations suggest in these regions, reducing the overall transport of tracers from these locations, and perhaps overemphasizing the importance of advective transport. In relatively quiescent regions, we are likewise overestimating the amount of diffusive transport particularly in the deep and abyssal ocean. Whereas spatial heterogeneity of κ_h may in turn yield gradients of tracers along an isopycnal, homeogeneous κ_h could lead to weak, along-isopycnal gradients of modeled tracer concentrations.

While diapycnal mixing due to shear-driven turbulence is likely to be of lesser direct importance than the along-isopycnal mixing for the transport of tracers, it does affect the depth of the thermocline because it helps mediate the transfer of heat from the surface to the

interior (Hu, 1996; Park and Bryan, 2000). The Hallberg (2000) parameterization diagnoses diapycnal diffusivity (κ_d) using a local gradient Richardson number. However, because the Richardson number is calculated at the interface of two isopycnal layers, this can lead to surface-intensified mixing. This may be the reason for the depth of the thermocline being too shallow in the sections for the Indian and Pacific Ocean in Chapter 4. The follow-on to HIM, the General Ocean Layer Dynamics Model (GOLD) incorporates the Jackson et al. (2008) parameterization which does allow for non-localized mixing (analogous to a vertical diffusion of turbulent kinetic energy). Profiles of κ_d tend to be smoother in GOLD than in HIM and the depth of subtropical thermocline in GOLD is similar to the observed depth. Both the shallower thermocline and weaker κ_d in HIM may mean that the CFCs and SF_6 concentrations are too low near the base of the thermocline.

The relatively coarse resolution of the model also means that some mesoscale features that control water mass formation in the subtropical thermocline are poorly represented. This is particularly evident for the NPIW which, in contrast to observations and noted in Chapter 4, is slightly thicker in the model along 30°N in the North Pacific. In nature, the NPIW is formed between the Oyashio and Kuroshio just east of Japan (Talley et al., 1995). In the model, these two currents are much broader and more diffuse than observed leading to a larger region where NPIW can be formed. Likewise, the North Pacific Central Mode Water and subtropical mode waters are not distinct water masses in the model because of a weaker, modeled Kuroshio recirculation. Other boundary currents and the Antarctic Circumpolar Current are likely to also be too broad and diffuse. Thus for some water masses, the subduction regions and formation mechanisms of both mode waters and intermediate waters likely differ from observations.

Despite these caveats, the work presented here stresses the importance of tracers to both observational and modeling studies in oceanography as ways to understand the complex 3-dimensional circulation of the ocean. The historical literature provides an observational and

theoretical framework on which to understand the mean state of oceanic ventilation. Understanding the variability of the thermocline on the other hand is still an open question partly due to the historically sparse sampling of even basic ocean properties both at the surface and at depth. Satellite remote sensing, observations of tracers both physical and chemical by Argo floats, and the continuing hydrographic efforts of GO-SHIP, GEOTRACES, and other similar international collaborations, together form a wealth of information about both the surface and interior ocean. Combined with new techniques which take advantage of tracer information, these data can be used shed insight how variability in thermocline ventilation may affect the uptake of heat and anthropogenic carbon dioxide due to anthropogenic climate change.

BIBLIOGRAPHY

Allison, L. C., H. L. Johnson, D. P. Marshall, and D. R. Munday, 2010: Where do winds drive the Antarctic Circumpolar Current? *Geophysical Research Letters*, **37 (12)**, n/a–n/a, doi:10.1029/2010GL043355.

Anderson, L. A., and J. L. Sarmiento, 1994: Redfield ratios of remineralization determined by nutrient data analysis. *Global Biogeochemical Cycles*, **8 (1)**, 65–80, doi:10.1029/93GB03318.

Anderson, T. W., 1962: On the Distribution of the Two-Sample Cramer-von Mises Criterion. *The Annals of Mathematical Statistics*, **33 (3)**, 1148–1159.

Andrié, C., P. Jean-baptiste, and L. Merlivat, 1988: Tritium and helium 3 in the northeastern Atlantic Ocean during the 1983 TOPOGULF cruise. *Journal of Geophysical Research*, **93 (C10)**, 12 511, doi:10.1029/JC093iC10p12511.

Aoki, S., 2005: Interdecadal water mass changes in the Southern Ocean between 30E and 160E. *Geophysical Research Letters*, **32 (7)**, L07 607, doi:10.1029/2004GL022220.

Ayers, J. M., and P. G. Strutton, 2013: Nutrient variability in Subantarctic Mode Waters forced by the Southern Annular Mode and ENSO. *Geophysical Research Letters*, **40 (13)**, 3419–3423, doi:10.1002/grl.50638.

Belkin, I. M., and A. L. Gordon, 1996: Southern Ocean fronts from the Greenwich meridian to Tasmania. *Journal of Geophysical Research*, **101 (C2)**, 3675, doi:10.1029/95JC02750.

Bender, E. A., 2000: *An Introduction to Mathematical Modeling*. Courier Corporation, 256 pp.

Bingham, F., 1992: Formation and Spreading of Subtropical Mode Water in the North Pacific. *Journal of Geophysical Research: Oceans*, **97 (C7)**, 11,177–11,189, doi:10.1029/92JC01001.

Bjerknes, V., E. Volken, and S. Brennimann, 1904: The problem of weather prediction, considered from the viewpoints of mechanics and physics. *Meteorologische Zeitschrift*, **18 (6)**, 663–667, doi:10.1127/0941-2948/2009/416.

Bolin, B., and H. Rodhe, 1973: A note on the concepts of age distribution and transit time in natural reservoirs. *Tellus*, **25 (1)**, 58–62, doi:10.1111/j.2153-3490.1973.tb01594.x.

Bracewell, R. N., 2000: The Fourier Transform and Its Applications. *American Journal of Physics*, **34 (8)**, 616, doi:10.1049/ep.1965.0268.

Broecker, W. S., T. H. Peng, and G. Ostlund, 1986: The distribution of bomb tritium in the ocean. *Journal of Geophysical Research*, **91 (C12)**, 14 331, doi:10.1029/JC091iC12p14331.

Bullister, J. L., and R. F. Weiss, 1983: Anthropogenic chlorofluoromethanes in the greenland and norwegian seas. *Science (New York, N.Y.)*, **221 (4607)**, 265–8, doi:10.1126/science.221.4607.265.

Bullister, J. L., D. P. Wisegarver, and F. a. Menzia, 2002: The solubility of sulfur hexafluoride in water and seawater. *Deep Sea Research Part I: Oceanographic Research Papers*, **49 (1)**, 175–187, doi:10.1016/S0967-0637(01)00051-6.

Bullister, J. L., D. P. Wisegarver, and R. E. Sonnerup, 2006: Sulfur hexafluoride as a transient tracer in the North Pacific Ocean. *Geophysical Research Letters*, **33 (18)**, L18 603, doi:10.1029/2006GL026514.

Cai, W., A. Sullivan, and T. Cowan, 2011: Interactions of ENSO, the IOD, and the SAM in CMIP3 Models. *Journal of Climate*, **24 (6)**, 1688–1704, doi:10.1175/2010JCLI3744.1.

Chapman, C., 2014: Southern Ocean jets and how to find them: Improving and comparing common jet detection methods. *Journal of Geophysical Research: Oceans*, 4318–4339, doi:10.1002/2014JC009810.Received.

Chapman, C. C., and A. McC. Hogg, 2013: Jet Jumping: Low-Frequency Variability in the Southern Ocean. *Journal of Physical Oceanography*, **43 (5)**, 990–1003, doi:10.1175/JPO-D-12-0123.1.

Chapman, C. C., and R. Morrow, 2014: Variability of Southern Ocean Jets near Topography. *Journal of Physical Oceanography*, **44 (2)**, 676–693, doi:10.1175/JPO-D-13-0182.1.

Chelton, D. B., M. G. Schlax, and R. M. Samelson, 2011: Global observations of nonlinear mesoscale eddies. *Progress in Oceanography*, **91 (2)**, 167–216, doi:10.1016/j.pocean.2011.01.002.

Ciasto, L. M., and D. W. J. Thompson, 2008: Observations of Large-Scale OceanAtmosphere Interaction in the Southern Hemisphere. *Journal of Climate*, **21 (6)**, 1244–1259, doi:10.1175/2007JCLI1809.1.

Cole, S. T., C. Wortham, E. Kunze, and W. B. Owens, 2015: Eddy stirring and horizontal diffusivity from Argo float observations: Geographic and depth variability. *Geophysical Research Letters*, **42 (10)**, 3989–3997, doi:10.1002/2015GL063827.

Cox, M. D., 1975: A Baroclinic Numerical Model of the Word Ocean: Preliminary Results. *Numerical Models of Ocean Circulation*.

Cushman-Roisin, B., 1987: Subduction. *Dynamics of the Oceanic Surface Mixed Layer*, Hawaiian Winter Workshop, U of Hawaii at Manoa, 181.

Dee, D. P., and Coauthors, 2011: The ERA-Interim reanalysis: configuration and performance of the data assimilation system. *Quarterly Journal of the Royal Meteorological Society*, **137 (656)**, 553–597, doi:10.1002/qj.828.

Deutsch, C., 2005: Fingerprints of climate change in North Pacific oxygen. *Geophysical Research Letters*, **32 (16)**, L16 604, doi:10.1029/2005GL023190.

Deutsch, C., S. Emerson, and L. Thompson, 2006: Physical-biological interactions in North Pacific oxygen variability. *Journal of Geophysical Research*, **111 (C9)**, C09S90, doi:10.1029/2005JC003179.

Dickson, R. R., E. M. Gmitrowicz, and A. J. Watson, 1990: Deep-water renewal in the northern North Atlantic. *Nature*, **344 (6269)**, 848–850, doi:10.1038/344848a0.

Domingues, R., G. Goni, S. Swart, and S. Dong, 2014: Wind forced variability of the Antarctic Circumpolar Current south of Africa between 1993 and 2010. *Journal of Geophysical Research: Oceans*, **119 (2)**, 1123–1145, doi:10.1002/2013JC008908.

Ebbesmeyer, C. C., D. R. Cayan, D. R. McLain, F. H. Nichols, D. H. Peterson, K. T. Redmond, and C. D. o. W. Resources, 1991: 1976 step in the Pacific climate: forty environmental changes between 1968-1975 and 1977-1984. *Proceedings of the Seventh Annual Pacific Climate (PACLIM) Workshop, April 1990. California Department of Water Resources. Interagency Ecological Studies Program Technical Report 26*, 115–126.

Efron, B., and R. Tibshirani, 1994: *An Introduction to the Bootstrap*. CRC Press, 456 pp.

Ekman, V., 1906: Beiträge zur Theorie der Meeresströmungen.

Emerson, S., Y. W. Watanabe, T. Ono, and S. Mecking, 2004: Temporal Trends in Apparent Oxygen Utilization in the Upper Pycnocline of the North Pacific: 19802000. *Journal of Oceanography*, **60 (1)**, 139–147, doi:10.1023/B:JOCE.0000038323.62130.a0.

England, M. H., V. Garçon, and J.-F. Minster, 1994: Chlorofluorocarbon uptake in a world ocean model: 1. Sensitivity to the surface gas forcing. *Journal of Geophysical Research*, **99 (C12)**, 25 215, doi:10.1029/94JC02205.

England, M. H., and E. Maier-Reimer, 2001: Using chemical tracers to assess ocean models. *Reviews of Geophysics*, **39 (1)**, 29–70, doi:10.1029/1998RG000043.

Fisher, R. A., 1930: The Moments of the Distribution for Normal Samples of Measures of Departure from Normality. *Proceedings of the Royal Society A: Mathematical, Physical and Engineering Sciences*, **130 (812)**, 16–28, doi:10.1098/rspa.1930.0185.

Fu, L.-L., 2009: Pattern and velocity of propagation of the global ocean eddy variability. *Journal of Geophysical Research*, **114 (C11)**, C11 017, doi:10.1029/2009JC005349.

Fukumori, I., T. Lee, B. Cheng, and D. Menemenlis, 2004: The origin, pathway, and destination of Niño-3 water estimated by a simulated passive tracer and its adjoint. *Journal of Physical Oceanography*, 582–604.

Fyfe, J. C., and O. A. Saenko, 2006: Simulated changes in the extratropical Southern Hemisphere winds and currents. *Geophysical Research Letters*, **33 (6)**, L06 701, doi: 10.1029/2005GL025332.

Gammon, R. H., J. Cline, and D. Wisegarver, 1982: Chlorofluoromethanes in the northeast Pacific Ocean: Measured vertical distributions and application as transient tracers of upper ocean mixing. *Journal of Geophysical Research*, **87 (C12)**, 9441, doi: 10.1029/JC087iC12p09441.

Gent, P. R., and J. C. Mcwilliams, 1990: Isopycnal Mixing in Ocean Circulation Models. *Journal of Physical Oceanography*, **20 (1)**, 150–155, doi:10.1175/1520-0485(1990)020⟨0150:IMIOCM⟩2.0.CO;2.

Gill, A. E., 1982: *Atmosphere-Ocean Dynamics*. Academic Press, 662 pp.

Gille, S. T., 1994: Mean sea surface height of the Antarctic Circumpolar Current from Geosat data: Method and application. *Journal of Geophysical Research*, **99 (C9)**, 18 255, doi:10.1029/94JC01172.

Gille, S. T., 2003: Float Observations of the Southern Ocean. Part II: Eddy Fluxes. *Journal of Physical Oceanography*, **33 (6)**, 1182–1196, doi:10.1175/1520-0485(2003)033⟨1182:FOOTSO⟩2.0.CO;2.

Gille, S. T., 2014: Meridional displacement of the Antarctic Circumpolar Current. *Philosophical transactions. Series A, Mathematical, physical, and engineering sciences*, **372 (2019)**, 20130 273, doi:10.1098/rsta.2013.0273.

Gille, S. T., and K. A. Kelly, 1996: Scales of spatial and temporal variability in the Southern Ocean. *Journal of Geophysical Research*, **101 (C4)**, 8759, doi:10.1029/96JC00203.

Gong, D., and S. Wang, 1999: Definition of Antarctic Oscillation index. *Geophysical Research Letters*, **26 (4)**, 459–462, doi:10.1029/1999GL900003.

Gould, R. T., 1923: The Marine Chronometer: Its History and Development. *London*, 287.

Graham, R. M., and A. M. De Boer, 2013: The Dynamical Subtropical Front. *Journal of Geophysical Research: Oceans*, **118 (10)**, 5676–5685, doi:10.1002/jgrc.20408.

Graham, R. M., A. M. de Boer, K. J. Heywood, M. R. Chapman, and D. P. Stevens, 2012: Southern Ocean fronts: Controlled by wind or topography? *Journal of Geophysical Research*, **117 (C8)**, C08 018, doi:10.1029/2012JC007887.

Griffies, S. M., and Coauthors, 2009: Coordinated Ocean-ice Reference Experiments (COREs). *Ocean Modelling*, **26 (1-2)**, 1–46, doi:10.1016/j.ocemod.2008.08.007.

Gruber, N., J. L. Sarmiento, and T. F. Stocker, 1996: An improved method for detecting anthropogenic CO 2 in the oceans. *Global Biogeochemical Cycles*, **10 (4)**, 809–837, doi: 10.1029/96GB01608.

Haine, T., H. Zhang, D. Waugh, and M. Holzer, 2008: On transit-time distributions in unsteady circulation models. *Ocean Modelling*, **21 (1-2)**, 35–45, doi:10.1016/j.ocemod. 2007.11.004.

Haine, T. W., and K. J. Richards, 1995: The influence of the seasonal mixed layer on oceanic uptake of CFCs. *Journal of Geophysical Research*, **100 (C6)**, 10 727–10 744, doi: 10.1029/95JC00629.

Haine, T. W. N., and T. M. Hall, 2002: A Generalized Transport Theory: Water-Mass Composition and Age. *Journal of Physical Oceanography*, **32 (6)**, 1932–1946, doi:10.1175/ 1520-0485(2002)032⟨1932:AGTTWM⟩2.0.CO;2.

Hall, T. M., T. W. N. Haine, and D. W. Waugh, 2002: Inferring the concentration of anthropogenic carbon in the ocean from tracers. *Global Biogeochemical Cycles*, **16 (4)**, 78–1–78–15, doi:10.1029/2001GB001835.

Hall, T. M., T. W. N. Haine, D. W. Waugh, M. Holzer, F. Terenzi, and D. a. LeBel, 2007: Ventilation Rates Estimated from Tracers in the Presence of Mixing. *Journal of Physical Oceanography*, **37 (11)**, 2599–2611, doi:10.1175/2006JPO3471.1.

Hall, T. M., and R. A. Plumb, 1994: Age as a diagnostic of stratospheric transport. *Journal of Geophysical Research*, **99 (D1)**, 1059, doi:10.1029/93JD03192.

Hallberg, R., 2000: Time Integration of Diapycnal Diffusion and Richardson NumberDependent Mixing in Isopycnal Coordinate Ocean Models. *Monthly Weather Review*, **128 (5)**, 1402–1419, doi:10.1175/1520-0493(2000)128⟨1402:TIODDA⟩2.0.CO;2.

Hallberg, R., 2003: The ability of large-scale ocean models to accept parameterizations of boundary mixing, and a description of a refined bulk mixed-layer model. *Proceedings of the 2003 Aha Hulikoa Hawaiian Winter ....*

Hallberg, R., and A. Gnanadesikan, 2006: The Role of Eddies in Determining the Structure and Response of the Wind-Driven Southern Hemisphere Overturning: Results from the Modeling Eddies in the Southern Ocean (MESO) Project. *Journal of Physical Oceanography*, **36 (12)**, 2232–2252, doi:10.1175/JPO2980.1.

Hallberg, R. W., 1995: Some aspects of the circulation in ocean basins with isopycnals intersecting the sloping boundaries. Ph.D. thesis, University of Washington.

Hare, S. R., and N. J. Mantua, 2000: Empirical evidence for North Pacific regime shifts in 1977 and 1989. *Progress in Oceanography*, **47 (2-4)**, 103–145, doi:10.1016/S0079-6611(00)00033-1.

Ho, D. T., J. R. Ledwell, and W. M. Smethie, 2008: Use of SF 5 CF 3 for ocean tracer release experiments. *Geophysical Research Letters*, **35 (4)**, L04 602, doi:10.1029/2007GL032799.

Holte, J., and L. Talley, 2009: A New Algorithm for Finding Mixed Layer Depths with Applications to Argo Data and Subantarctic Mode Water Formation*. *Journal of Atmospheric and Oceanic Technology*, **26 (9)**, 1920–1939, doi:10.1175/2009JTECHO543.1.

Holzer, M., and T. M. Hall, 2000: Transit-Time and Tracer-Age Distributions in Geophysical Flows. *Journal of the Atmospheric Sciences*, **57 (21)**, 3539–3558, doi:10.1175/1520-0469(2000)057⟨3539:TTATAD⟩2.0.CO;2.

Holzer, M., and F. W. Primeau, 2010: Improved constraints on transit time distributions from argon 39: A maximum entropy approach. *Journal of Geophysical Research*, **115 (C12)**, C12 021, doi:10.1029/2010JC006410.

Hu, D., 1996: On the Sensitivity of Thermocline Depth and Meridional Heat Transport to Vertical Diffusivity in OGCMS. *Journal of Physical Oceanography*, **26 (8)**, 1480–1494, doi:10.1175/1520-0485(1996)026⟨1480:OTSOTD⟩2.0.CO;2.

Hughes, C. W., A. F. Thompson, and C. Wilson, 2010: Identification of jets and mixing barriers from sea level and vorticity measurements using simple statistics. *Ocean Modelling*, **32 (1-2)**, 44–57, doi:10.1016/j.ocemod.2009.10.004.

Idyll, C., 1970: *The science of the sea: a history of oceanography*. Nelson.

Iselin, C. O., 1939: The influence of vertical and lateral turbulence on the characteristics of the waters at mid-depths. *Transactions, American Geophysical Union*, **20 (3)**, 414, doi:10.1029/TR020i003p00414.

Jackson, L., R. Hallberg, and S. Legg, 2008: A Parameterization of Shear-Driven Turbulence for Ocean Climate Models. *Journal of Physical Oceanography*, **38 (5)**, 1033–1053, doi: 10.1175/2007JPO3779.1.

Jenkins, W. J., 1987: 3 H and 3 He in the Beta Triangle: Observations of Gyre Ventilation and Oxygen Utilization Rates. *Journal of Physical Oceanography*, **17 (6)**, 763–783, doi: 10.1175/1520-0485(1987)017⟨0763:AITBTO⟩2.0.CO;2.

Keeling, R. F., 1993: On the role of large bubbles in air-sea gas exchange and supersaturation in the ocean. *Journal of Marine Research*, **51 (2)**, 237–271, doi:10.1357/ 0022240933223800.

Keffer, T., and G. Holloway, 1988: Estimating Southern Ocean eddy flux of heat and salt from satellite altimetry. *Nature*, **332 (6165)**, 624–626, doi:10.1038/332624a0.

Khatiwala, S., 2007: A computational framework for simulation of biogeochemical tracers in the ocean. *Global Biogeochemical Cycles*, **21 (3)**, doi:10.1029/2007GB002923.

Khatiwala, S., F. Primeau, and T. Hall, 2009: Reconstruction of the history of anthropogenic CO(2) concentrations in the ocean. *Nature*, **462 (7271)**, 346–9, doi:10.1038/nature08526.

Kibler, S., and F. Primeau, 2006: A Maximum Entropy Approach to Water Mass Analysis. *American Geophysical Union*.

Kim, Y. S., and A. H. Orsi, 2014: On the Variability of Antarctic Circumpolar Current Fronts Inferred from 19922011 Altimetry*. *Journal of Physical Oceanography*, **44 (12)**, 3054–3071, doi:10.1175/JPO-D-13-0217.1.

Kobayashi, T., 1999: Study of the formation of North Pacific Intermediate Water by a general circulation model and the particle-tracking method: 1. A pitfall of general circulation model studies. *Journal of Geophysical Research: Oceans*, **104 (C3)**, 5423–5439, doi:10.1029/1998JC900084.

Körtzinger, A., J. Schimanski, U. Send, and D. Wallace, 2004: The ocean takes a deep breath. *Science (New York, N.Y.)*, **306 (5700)**, 1337, doi:10.1126/science.1102557.

Kraus, E. B., and J. S. Turner, 1967: A one-dimensional model of the seasonal thermocline II. The general theory and its consequences. *Tellus*, **19 (1)**, 98–106, doi:10.3402/tellusa.v19i1.9753.

Ladd, C., and L. A. Thompson, 2000: Formation Mechanisms for North Pacific Central and Eastern Subtropical Mode Waters. *Journal of Physical Oceanography*, **30 (5)**, 868–887, doi:10.1175/1520-0485(2000)030⟨0868:FMFNPC⟩2.0.CO;2.

Ladd, C., and L. A. Thompson, 2001: Water Mass Formation in an Isopycnal Model of the North Pacific. *Journal of Physical Oceanography*, **31 (6)**, 1517–1537, doi:10.1175/1520-0485(2001)031⟨1517:WMFIAI⟩2.0.CO;2.

Ladd, C., and L. A. Thompson, 2002: Decadal Variability of North Pacific Central Mode Water*. *Journal of Physical Oceanography*, **32 (10)**, 2870–2881, doi:10.1175/1520-0485(2002)032⟨2870:DVONPC⟩2.0.CO;2.

Large, W. G., and S. G. Yeager, 2008: The global climatology of an interannually varying airsea flux data set. *Climate Dynamics*, **33 (2-3)**, 341–364, doi:10.1007/s00382-008-0441-3.

Lovenduski, N. S., 2005: Impact of the Southern Annular Mode on Southern Ocean circulation and biology. *Geophysical Research Letters*, **32 (11)**, L11 603, doi:10.1029/2005GL022727.

Maltrud, M., F. Bryan, and S. Peacock, 2009: Boundary impulse response functions in a century-long eddying global ocean simulation. *Environmental Fluid Mechanics*, **10 (1-2)**, 275–295, doi:10.1007/s10652-009-9154-3.

Maltrud, M. E., and J. L. McClean, 2005: An eddy resolving global 1/10 ocean simulation. *Ocean Modelling*, **8 (1-2)**, 31–54, doi:10.1016/j.ocemod.2003.12.001.

Mantua, N. J., S. R. Hare, Y. Zhang, J. M. Wallace, and R. C. Francis, 1997: A Pacific Interdecadal Climate Oscillation with Impacts on Salmon Production. *Bulletin of the American Meteorological Society*, **78 (6)**, 1069–1079, doi:10.1175/1520-0477(1997)078⟨1069:APICOW⟩2.0.CO;2.

Marotzke, J., R. Giering, K. Q. Zhang, D. Stammer, C. Hill, and T. Lee, 1999: Construction of the adjoint MIT ocean general circulation model and application to Atlantic heat transport sensitivity. *Journal of Geophysical Research: Oceans*, **104 (C12)**, 29 529–29 547, doi:10.1029/1999JC900236.

Marshall, D., 1995: Topographic steering of the Antarctic Circumpolar Current. *Journal of physical oceanography*.

Marshall, J., and F. Schott, 1999: Open-ocean convection: Observations, theory, and models. *Reviews of Geophysics*, **37 (1)**, 1–64, doi:10.1029/98RG02739.

McCaffrey, K., 2014: Characterizing Ocean Turbulence from Argo, Acoustic Doppler, and Simulation Data. Ph.D. thesis, University of Colorado Boulder.

McCartney, M. S., 1982: The subtropical recirculation of mode waters. *Journal of Marine Research*, **40 (Supplement)**, 427–464.

Mecking, S., 2004: Influence of mixing on CFC uptake and CFC ages in the North Pacific thermocline. *Journal of Geophysical Research*, **109 (C7)**, C07 014, doi:10.1029/2003JC001988.

Mecking, S., G. Johnson, J. Bullister, and A. Macdonald, 2012: Decadal changes in oxygen and temperature-salinity relations along 32S in the Indian Ocean through 2009. Ocean Sciences Meeting 2012.

Mecking, S., C. Langdon, R. A. Feely, C. L. Sabine, C. A. Deutsch, and D.-H. Min, 2008: Climate variability in the North Pacific thermocline diagnosed from oxygen measurements: An update based on the U.S. CLIVAR/CO 2 Repeat Hydrography cruises. *Global Biogeochemical Cycles*, **22 (3)**, n/a–n/a, doi:10.1029/2007GB003101.

Mecking, S., M. J. Warner, and J. L. Bullister, 2006: Temporal changes in pCFC-12 ages and AOU along two hydrographic sections in the eastern subtropical North Pacific. *Deep Sea Research Part I: Oceanographic Research Papers*, **53 (1)**, 169–187, doi:10.1016/j.dsr.2005.06.018.

Meijers, a. J. S., E. Shuckburgh, N. Bruneau, J.-B. Sallee, T. J. Bracegirdle, and Z. Wang, 2012: Representation of the Antarctic Circumpolar Current in the CMIP5 climate models and future changes under warming scenarios. *Journal of Geophysical Research*, **117 (C12)**, C12 008, doi:10.1029/2012JC008412.

Montgomery, R., 1937: A suggested method for representing gradient flow in isentropic surfaces. *Bull. Amer. Meteor. Soc.*

Moore, A. M., H. G. Arango, E. Di Lorenzo, B. D. Cornuelle, A. J. Miller, and D. J. Neilson, 2004: A comprehensive ocean prediction and analysis system based on the tangent linear and adjoint of a regional ocean model. *Ocean Modelling*, **7 (1-2)**, 227–258, doi: 10.1016/j.ocemod.2003.11.001.

Moore, J. K., M. R. Abbott, and J. G. Richman, 1997: Variability in the location of the Antarctic Polar Front (9020W) from satellite sea surface temperature data. *Journal of Geophysical Research*, **102 (C13)**, 27 825, doi:10.1029/97JC01705.

Munk, W. H., 1950: on the Wind-Driven Ocean Circulation. *Journal of Meteorology*, **7 (2)**, 80–93, doi:10.1175/1520-0469(1950)007⟨0080:OTWDOC⟩2.0.CO;2.

Najjar, R. G., and J. C. Orr, 1998: Design of OCMIP-2 simulations of chlorofluorocarbons, the solubility pump and common biogeochemistry. *Internal OCMIP Report, LSCE/CEA Saclay, Gifsur- . . .*, 1–19.

Nakamura, H., 1996: A pycnostad on the bottom of the ventilated portion in the central subtropical North Pacific: Its distribution and formation. *Journal of Oceanography*, **52 (2)**, 171–188, doi:10.1007/BF02235668.

Orsi, A. H., T. Whitworth, and W. D. Nowlin, 1995: On the meridional extent and fronts of the Antarctic Circumpolar Current. *Deep Sea Research Part I: Oceanographic Research Papers*, **42 (5)**, 641–673, doi:10.1016/0967-0637(95)00021-W.

Park, Y.-G., and K. Bryan, 2000: Comparison of Thermally Driven Circulations from a Depth-Coordinate Model and an Isopycnal-Layer Model. Part I: Scaling-Law Sensitivity to Vertical Diffusivity. *Journal of Physical Oceanography*, **30 (3)**, 590–605, doi:10.1175/1520-0485(2000)030⟨0590:COTDCF⟩2.0.CO;2.

Peacock, S., and M. Maltrud, 2006: Transit-Time Distributions in a Global Ocean Model. *Journal of Physical Oceanography*, **36 (3)**, 474–495, doi:10.1175/JPO2860.1.

Penduff, T., M. Juza, L. Brodeau, G. C. Smith, B. Barnier, J.-M. Molines, A.-M. Treguier, and G. Madec, 2010: Impact of global ocean model resolution on sea-level variability with emphasis on interannual time scales. *Ocean Science*, **6 (1)**, 269–284, doi:10.5194/os-6-269-2010.

Primeau, F., 2005: Characterizing Transport between the Surface Mixed Layer and the Ocean Interior with a Forward and Adjoint Global Ocean Transport Model. *Journal of Physical Oceanography*, **35 (4)**, 545–564, doi:10.1175/JPO2699.1.

Qiu, B., and R. X. Huang, 1995: Ventilation of the North Atlantic and North Pacific: Subduction Versus Obduction. *Journal of Physical Oceanography*, **25 (10)**, 2374–2390, doi:10.1175/1520-0485(1995)025⟨2374:VOTNAA⟩2.0.CO;2.

Redfield, A. C., 1934: *On the Proportions of Organic Derivatives in Sea Water and Their Relation to the Composition of Plankton*. University Press of Liverpool, 17 pp.

Redi, M. H., 1982: Oceanic Isopycnal Mixing by Coordinate Rotation. *Journal of Physical Oceanography*, **12 (10)**, 1154–1158, doi:10.1175/1520-0485(1982)012⟨1154:OIMBCR⟩2.0.CO;2.

Rimaud, J., S. Speich, B. Blanke, and N. Grima, 2012: The exchange of Intermediate Water in the southeast Atlantic: Water mass transformations diagnosed from the Lagrangian analysis of a regional ocean model. *Journal of Geophysical Research: Oceans*, **117 (C8)**, n/a–n/a, doi:10.1029/2012JC008059.

Robbins, P. E., and W. J. Jenkins, 1998: Observations of temporal changes of tritium-¡SUP¿3¡/SUP¿He age in the eastern North Atlantic thermocline: Evidence for

changes in ventilation? *Journal of Marine Research*, **56 (5)**, 1125–1161, doi:10.1357/002224098765173482.

Rodehacke, C. B., W. Roether, H. H. Hellmer, and T. Hall, 2010: Temporal variations and trends of CFC11 and CFC12 surface-water saturations in Antarctic marginal seas: Results of a regional ocean circulation model. *Deep Sea Research Part I: Oceanographic Research Papers*, **57 (2)**, 175–198, doi:10.1016/j.dsr.2009.09.008.

Rooth, C. G., and G. Östlund, 1972: Penetration of tritium into the Atlantic thermocline. *Deep Sea Research and Oceanographic Abstracts*, **19 (7)**, 481–492, doi:10.1016/0011-7471(72)90016-2.

Saenko, O. A., J. C. Fyfe, and M. H. England, 2005: On the response of the oceanic wind-driven circulation to atmospheric CO2 increase. *Climate Dynamics*, **25 (4)**, 415–426, doi:10.1007/s00382-005-0032-5.

Sallée, J. B., K. Speer, and R. Morrow, 2008: Response of the Antarctic Circumpolar Current to Atmospheric Variability. *Journal of Climate*, **21 (12)**, 3020–3039, doi:10.1175/2007JCLI1702.1.

Sallée, J.-B., K. Speer, S. Rintoul, and S. Wijffels, 2010: Southern Ocean Thermocline Ventilation. *Journal of Physical Oceanography*, **40 (3)**, 509–529, doi:10.1175/2009JPO4291.1.

Sandström, J., 1908: Dynamische versuche mit meerwasser. *Ann. Hydrodynam. Marine Meteorol.*

Sarmiento, J. L., 1983: A Tritium Box Model of the North Atlantic Thermocline. *Journal of Physical Oceanography*, **13 (7)**, 1269–1274, doi:10.1175/1520-0485(1983)013⟨1269:ATBMOT⟩2.0.CO;2.

Schudlich, R., and S. Emerson, 1996: Gas supersaturation in the surface ocean: The roles of heat flux, gas exchange, and bubbles. *Deep Sea Research Part II: Topical Studies in Oceanography*, **43 (2-3)**, 569–589, doi:10.1016/0967-0645(95)00098-4.

Seabrooke, J. M., G. L. Hufford, and R. B. Elder, 1971: Formation of Antarctic bottom water in the Weddell Sea. *Journal of Geophysical Research*, **76 (9)**, 2164–2178, doi:10.1029/JC076i009p02164.

Seshadri, V., 1999: *The Inverse Gaussian Distribution*, Lecture Notes in Statistics, Vol. 137. Springer New York, New York, NY, doi:10.1007/978-1-4612-1456-4.

Shao, A. E., S. T. Gille, S. Mecking, and L. Thompson, 2015: Properties of the Subantarctic Front and Polar Front from the skewness of sea level anomaly. *Journal of Geophysical Research: Oceans*, **120 (7)**, 5179–5193, doi:10.1002/2015JC010723.

Shao, A. E., S. Mecking, L. Thompson, and R. E. Sonnerup, 2013: Mixed layer saturations of CFC-11, CFC-12, and SF 6 in a global isopycnal model. *Journal of Geophysical Research: Oceans*, **118 (10)**, 4978–4988, doi:10.1002/jgrc.20370.

Sloyan, B. M., and S. R. Rintoul, 2001: Circulation, Renewal, and Modification of Antarctic Mode and Intermediate Water*. *Journal of Physical Oceanography*, **31 (4)**, 1005–1030, doi:10.1175/1520-0485(2001)031⟨1005:CRAMOA⟩2.0.CO;2.

Smethie, W. M., and R. A. Fine, 2001: Rates of North Atlantic Deep Water formation calculated from chlorofluorocarbon inventories. *Deep Sea Research Part I: Oceanographic Research Papers*, **48 (1)**, 189–215, doi:10.1016/S0967-0637(00)00048-0.

Smith, R. D., M. E. Maltrud, F. O. Bryan, and M. W. Hecht, 2000: Numerical Simulation of the North Atlantic Ocean at 1 / 10 . *Journal of Physical Oceanography*, **30 (7)**, 1532–1561, doi:10.1175/1520-0485(2000)030⟨1532:NSOTNA⟩2.0.CO;2.

Smith, W. H., 1997: Global Sea Floor Topography from Satellite Altimetry and Ship Depth Soundings. *Science*, **277 (5334)**, 1956–1962, doi:10.1126/science.277.5334.1956.

Sokolov, S., and S. R. Rintoul, 2002: Structure of Southern Ocean fronts at 140E. *Journal of Marine Systems*, **37 (1-3)**, 151–184, doi:10.1016/S0924-7963(02)00200-2.

Sokolov, S., and S. R. Rintoul, 2007: On the relationship between fronts of the Antarctic Circumpolar Current and surface chlorophyll concentrations in the Southern Ocean. *Journal of Geophysical Research*, **112 (C7)**, C07 030, doi:10.1029/2006JC004072.

Sokolov, S., and S. R. Rintoul, 2009: Circumpolar structure and distribution of the Antarctic Circumpolar Current fronts: 1. Mean circumpolar paths. *Journal of Geophysical Research*, **114 (C11)**, C11 018, doi:10.1029/2008JC005108.

Sonnerup, R. E., 2001: On the relations among CFC derived water mass ages. *Geophysical Research Letters*, **28 (9)**, 1739–1742, doi:10.1029/2000GL012569.

Sonnerup, R. E., J. L. Bullister, and S. Mecking, 2007: Circulation rate changes in the eastern subtropical North Pacific based on chlorofluorocarbon ages. *Geophysical Research Letters*, **34 (8)**, L08 605, doi:10.1029/2006GL028813.

Sonnerup, R. E., J. L. Bullister, and M. J. Warner, 2008: Improved estimates of ventilation rate changes and CO 2 uptake in the Pacific Ocean using chlorofluorocarbons and sulfur hexafluoride. *Journal of Geophysical Research*, **113 (C12)**, C12 007, doi: 10.1029/2008JC004864.

Sonnerup, R. E., S. Mecking, and J. L. Bullister, 2013: Transit time distributions and oxygen utilization rates in the Northeast Pacific Ocean from chlorofluorocarbons and sulfur hexafluoride. *Deep Sea Research Part I: Oceanographic Research Papers*, **72**, 61–71, doi: 10.1016/j.dsr.2012.10.013.

Sonnerup, R. E., S. Mecking, J. L. Bullister, and M. J. Warner, 2015: Transit time distributions and oxygen utilization rates from chlorofluorocarbons and sulfur hexafluoride in the Southeast Pacific Ocean. *Journal of Geophysical Research: Oceans*, **120 (5)**, 3761–3776, doi:10.1002/2015JC010781.

Stanley, R. H. R., S. C. Doney, W. J. Jenkins, and D. E. Lott, III, 2012: Apparent oxygen utilization rates calculated from tritium and helium-3 profiles at the Bermuda Atlantic Time-series Study site. *Biogeosciences*, **9 (6)**, 1969–1983, doi:10.5194/bg-9-1969-2012.

Steele, M., R. Morley, and W. Ermold, 2001: PHC: A Global Ocean Hydrography with a High-Quality Arctic Ocean. *Journal of Climate*, **14 (9)**, 2079–2087, doi:10.1175/1520-0442(2001)014⟨2079:PAGOHW⟩2.0.CO;2.

Stein, K., N. Schneider, A. Timmermann, and F. F. Jin, 2010: Seasonal synchronization of ENSO events in a linear stochastic model. *Journal of Climate*, **23 (21)**, 5629–5643, doi:10.1175/2010JCLI3292.1.

Stommel, H., 1948: The westward intensification of wind-driven ocean currents. *Transactions, American Geophysical Union*, **29 (2)**, 202, doi:10.1029/TR029i002p00202.

Stommel, H., 1979: Determination of water mass properties of water pumped down from the Ekman layer to the geostrophic flow below. *Proceedings of the National Academy of Sciences of the United States of America*, **76 (7)**, 3051–5.

Stöven, T., and T. Tanhua, 2014: Ventilation of the Mediterranean Sea constrained by multiple transient tracer measurements. *Ocean Science*, **10 (3)**, 439–457, doi:10.5194/os-10-439-2014.

Suga, T., Y. Takei, and K. Hanawa, 1997: Thermostad Distribution in the North Pacific Subtropical Gyre: The Central Mode Water and the Subtropical Mode Water. *Journal of*

Physical Oceanography, **27 (1)**, 140–152, doi:10.1175/1520-0485(1997)027⟨0140:TDITNP⟩2.0.CO;2.

Sura, P., and S. T. Gille, 2010: Stochastic Dynamics of Sea Surface Height Variability. *Journal of Physical Oceanography*, **40 (7)**, 1582–1596, doi:10.1175/2010JPO4331.1.

Sverdrup, H. U., 1947: Wind-Driven Currents in a Baroclinic Ocean; with Application to the Equatorial Currents of the Eastern Pacific. *Proceedings of the National Academy of Sciences of the United States of America*, **33 (11)**, 318–26.

Sweeney, C., E. Gloor, A. R. Jacobson, R. M. Key, G. McKinley, J. L. Sarmiento, and R. Wanninkhof, 2007: Constraining global air-sea gas exchange for CO 2 with recent bomb 14 C measurements. *Global Biogeochemical Cycles*, **21 (2)**, n/a–n/a, doi:10.1029/2006GB002784.

Taft, B., 1963: Distribution of salinity and dissolved oxygen on surfaces of uniform potential specific volume in the South Atlantic, South Pacific, and Indian Oceans. *Journal of Marine Research*.

Talley, L. D., 1993: Distribution and Formation of North Pacific Intermediate Water. *Journal of Physical Oceanography*, **23 (3)**, 517–537, doi:10.1175/1520-0485(1993)023⟨0517:DAFONP⟩2.0.CO;2.

Talley, L. D., 1996: Antarctic Intermediate Water in the South Atlantic. *The South Atlantic : present and past circulation*, Springer Berlin Heidelberg, 219–238, doi:10.1007/978-3-642-80353-6{_}11.

Talley, L. D., and M. S. McCartney, 1982: Distribution and Circulation of Labrador Sea Water. *Journal of Physical Oceanography*, **12 (11)**, 1189–1205, doi:10.1175/1520-0485(1982)012⟨1189:DACOLS⟩2.0.CO;2.

Talley, L. D., Y. Nagata, M. Fujimura, T. Iwao, T. Kono, D. Inagake, M. Hirai, and K. Okuda, 1995: North Pacific Intermediate Water in the Kuroshio/Oyashio Mixed Water Region. *Journal of Physical Oceanography*, **25 (4)**, 475–501, doi:10.1175/1520-0485(1995)025⟨0475:NPIWIT⟩2.0.CO;2.

Tanhua, T., E. P. Jones, E. Jeansson, S. Jutterström, W. M. Smethie, D. W. R. Wallace, and L. G. Anderson, 2009: Ventilation of the Arctic Ocean: Mean ages and inventories of anthropogenic CO 2 and CFC-11. *Journal of Geophysical Research*, **114 (C1)**, C01 002, doi:10.1029/2008JC004868.

Tanhua, T., D. W. Waugh, and J. L. Bullister, 2013: Estimating changes in ocean ventilation from early 1990s CFC-12 and late 2000s SF6 measurements. *Geophysical Research Letters*, **40 (5)**, 927–932, doi:10.1002/grl.50251.

Tanhua, T., D. W. Waugh, and D. W. R. Wallace, 2008: Use of SF6 to estimate anthropogenic CO2 in the upper ocean. *Journal of Geophysical Research: Oceans*, **113 (4)**, doi:10.1029/2007JC004416.

Thiele, G., and J. L. Sarmiento, 1990: Tracer dating and ocean ventilation. *Journal of Geophysical Research*, **95 (C6)**, 9377, doi:10.1029/JC095iC06p09377.

Thompson, A. F., and K. J. Richards, 2011: Low frequency variability of Southern Ocean jets. *Journal of Geophysical Research*, **116 (C9)**, C09 022, doi:10.1029/2010JC006749.

Thompson, A. F., and J.-B. Sallée, 2012: Jets and Topography: Jet Transitions and the Impact on Transport in the Antarctic Circumpolar Current. *Journal of Physical Oceanography*, **42 (6)**, 956–972, doi:10.1175/JPO-D-11-0135.1.

Thompson, K. R., and E. Demirov, 2006: Skewness of sea level variability of the world's oceans. *Journal of Geophysical Research*, **111 (C5)**, C05 005, doi:10.1029/2004JC002839.

Tokieda, T., M. Ishii, T. Yasuda, and K. Enyo, 2004: Chlorofluorocarbons (CFCs) in the North Pacific Central Mode Water: Possibility of under-saturation of CFCs in the winter-time mixed layer. *GEOCHEMICAL JOURNAL*, **38 (6)**, 643–650, doi:10.2343/geochemj.38.643.

Trossman, D., 2011: Advection-diffusion process inference via statistical oceanographic methods in the North Atlantic and Southern Oceans. Ph.d. thesis, University of Washington.

Trossman, D., L. Thompson, S. Mecking, M. Warner, F. Bryan, and S. Peacock, 2014: Evaluation of oceanic transport parameters using transient tracers from observations and model output. *Ocean Modelling*, **74**, 1–21, doi:10.1016/j.ocemod.2013.11.001.

Valsala, V., S. Maksyutov, and I. Motoyoshi, 2008: Design and Validation of an Offline Oceanic Tracer Transport Model for a Carbon Cycle Study. *Journal of Climate*, **21 (12)**, 2752–2769, doi:10.1175/2007JCLI2018.1.

Walker, S. J., R. F. Weiss, and P. K. Salameh, 2000: Reconstructed histories of the annual mean atmospheric mole fractions for the halocarbons CFC-11 CFC-12, CFC-113, and carbon tetrachloride. *Journal of Geophysical Research*, **105 (C6)**, 14 285, doi:10.1029/1999JC900273.

Wanninkhof, R., 1992: Relationship Between Wind Speed and Gas Exchange. *Journal of Geophysical Research*, **97 (92)**, 7373–7382, doi:10.1029/92JC00188.

Warner, M., and R. Weiss, 1985: Solubilities of chlorofluorocarbons 11 and 12 in water and seawater. *Deep Sea Research Part A. Oceanographic Research Papers*, **32 (12)**, 1485–1497, doi:10.1016/0198-0149(85)90099-8.

Warner, M. J., 1988: *Chlorofluoromethanes F-11 and F-12, Their Solubilities in Water*

and Seawater and Studies of Their Distributions in the South Atlantic and North Pacific Oceans. University of California, San Diego, 248 pp.

Warner, M. J., J. L. Bullister, D. P. Wisegarver, R. H. Gammon, and R. F. Weiss, 1996: Basin-wide distributions of chlorofluorocarbons CFC-11 and CFC-12 in the North Pacific: 19851989. *Journal of Geophysical Research*, **101 (C9)**, 20 525, doi:10.1029/96JC01849.

Waugh, D., 2002a: Age of stratospheric air: Theory, observations, and models. *Reviews of Geophysics*, **40 (4)**, 1010, doi:10.1029/2000RG000101.

Waugh, D. W., 2002b: Transit time distributions in Lake Issyk-Kul. *Geophysical Research Letters*, **29 (24)**, 2231, doi:10.1029/2002GL016201.

Waugh, D. W., 2003: Relationships among tracer ages. *Journal of Geophysical Research*, **108 (C5)**, 3138, doi:10.1029/2002JC001325.

Waugh, D. W., 2014: Changes in the ventilation of the southern oceans. *Philosophical transactions. Series A, Mathematical, physical, and engineering sciences*, **372 (2019)**, 20130 269, doi:10.1098/rsta.2013.0269.

Waugh, D. W., T. W. Haine, and T. M. Hall, 2004: Transport times and anthropogenic carbon in the subpolar North Atlantic Ocean. *Deep Sea Research Part I: Oceanographic Research Papers*, **51 (11)**, 1475–1491, doi:10.1016/j.dsr.2004.06.011.

Waugh, D. W., T. M. Hall, B. I. McNEIL, R. Key, and R. J. Matear, 2006: Anthropogenic CO 2 in the oceans estimated using transit time distributions. *Tellus B*, **58 (5)**, 376–389, doi:10.1111/j.1600-0889.2006.00222.x.

Waugh, D. W., F. Primeau, T. Devries, and M. Holzer, 2013: Recent changes in the ventilation of the southern oceans. *Science (New York, N.Y.)*, **339 (6119)**, 568–70, doi:10.1126/science.1225411.

Weiss, R. F., J. L. Bullister, R. H. Gammon, and M. J. Warner, 1985: Atmospheric chlorofluoromethanes in the deep equatorial Atlantic. *Nature*, **314 (6012)**, 608–610, doi:10.1038/314608a0.

Welch, P., 1967: The Use of Fast Fourier Transform for the Estimation of Power Spectra: A Method Based on Time Averaging Over Short, Modified Periodograms. *IEEE Trans. Audio & Electroacoust.*, 70–73.

Woods, J., 1985: *Coupled Ocean-Atmosphere Models*, Elsevier Oceanography Series, Vol. 40. Elsevier, 543–590 pp., doi:10.1016/S0422-9894(08)70730-X.

Xu, Y., and L.-L. Fu, 2011: Global Variability of the Wavenumber Spectrum of Oceanic Mesoscale Turbulence. *Journal of Physical Oceanography*, **41 (Fu 1983)**, 802–809, doi:10.1175/2010JPO4558.1.

Yasuda, I., 1997: The origin of the North Pacific Intermediate Water. *Journal of Geophysical Research*, **102 (C1)**, 893, doi:10.1029/96JC02938.

Zhang, Y., L. Jaegle, and L. Thompson, 2014: Natural biogeochemical cycle of mercury in a global three-dimensional ocean tracer model. *Global Biogeochemical Cycles*, **28 (5)**, 553–570, doi:10.1002/2014GB004814.

Zheng, M., W. J. De Bruyn, and E. S. Saltzman, 1998: Measurements of the diffusion coefficients of CFC-11 and CFC-12 in pure water and seawater. *Journal of Geophysical Research*, **103 (C10)**, 21 735, doi:10.1029/98JC02688.

Zöppritz, K., 1878: Hydrodynamische Probleme in Beziehung zur Theorie der Meeresströmungen. *Annalen der Physik und Chemie*, **239 (4)**, 582–607, doi:10.1002/andp.18782390409.